INFORMATION TO USERS

This manuscript has been reproduced from the microfilm master. UMI films the text directly from the original or copy submitted. Thus, some thesis and dissertation copies are in typewriter face, while others may be from any type of computer printer.

The quality of this reproduction is dependent upon the quality of the copy submitted. Broken or indistinct print, colored or poor quality illustrations and photographs, print bleedthrough, substandard margins, and improper alignment can adversely affect reproduction.

In the unlikely event that the author did not send UMI a complete manuscript and there are missing pages, these will be noted. Also, if unauthorized copyright material had to be removed, a note will indicate the deletion.

Oversize materials (e.g., maps, drawings, charts) are reproduced by sectioning the original, beginning at the upper left-hand corner and continuing from left to right in equal sections with small overlaps.

Photographs included in the original manuscript have been reproduced xerographically in this copy. Higher quality 6" x 9" black and white photographic prints are available for any photographs or illustrations appearing in this copy for an additional charge. Contact UMI directly to order.

Bell & Howell Information and Learning
300 North Zeeb Road, Ann Arbor, MI 48106-1346 USA
800-521-0600

UMI®

Reproduced with permission of the copyright owner. Further reproduction prohibited without permission.

Reproduced with permission of the copyright owner. Further reproduction prohibited without permission.

NEW, EFFICIENT, ROOM TEMPERATURE MID-INFRARED LASER AT 3.9 µM IN HO:BAY$_2$F$_8$ AND VISIBLE PR:LIYF$_4$ LASER FOR HOLOGRAPHY

By

ANNA M. TABIRIAN

A dissertation submitted in partial fulfillment of the requirements
for the degree of Doctor of Philosophy
from the Department of Physics
in the College of Art and Sciences
at the University of Central Florida
Orlando, Florida

Summer Term

2000

Major Professors: Dr. Hans P. Jenssen and Dr. Michael Bass

Reproduced with permission of the copyright owner. Further reproduction prohibited without permission.

UMI Number: 9977827

Copyright 2000 by
Tabirian, Anna Murazian

All rights reserved.

UMI Microform 9977827
Copyright 2000 by Bell & Howell Information and Learning Company.
All rights reserved. This microform edition is protected against
unauthorized copying under Title 17, United States Code.

Bell & Howell Information and Learning Company
300 North Zeeb Road
P.O. Box 1346
Ann Arbor, MI 48106-1346

Reproduced with permission of the copyright owner. Further reproduction prohibited without permission.

Copyright ©2000

By

Anna M. Tabirian

Reproduced with permission of the copyright owner. Further reproduction prohibited without permission.

ABSTRACT

This dissertation describes a series of experiments and theoretical studies, which led to the development of two new solid state laser systems: efficient, room temperature mid-infrared solid state laser at 3.9 μm in Ho^{3+} doped BaY_2F_8 and visible Pr:$LiYF_4$ laser at 640 nm for holography.

The 3.9 μm laser wavelength matches the peak of mid-IR atmospheric transmission window, which makes it very important for multiple applications such as remote sensing, imaging, IR countermeasures, eye-safe lidars and environmental agent detection.

We present the results of spectroscopic evaluations and numerical modeling of energy transfer processes between rare earth ions of Ho^{3+} doped in two host laser materials: BaY_2F_8 and $LiYF_4$. The 3.9 μm laser is based on transition with upper laser lifetime considerably shorter than lower level lifetime, which in general leads to self-terminating laser action in the cw mode or at high repetition rates. Therefore, three different pumping and lasing schemes, that could allow overcoming these limitations have been suggested and studied.

Reproduced with permission of the copyright owner. Further reproduction prohibited without permission.

First, cascade laser action at 1.4 μm and 3.9 μm was achieved with low thresholds and near-theoretical quantum efficiency in Ho^{3+} doped BaY_2F_8 pumped at 532 nm by a Q-switched frequency doubled Nd:YAG laser.

Next, the feasibility of achieving 3.9 μm laser with cw resonant cascade pumping at 750 nm by a Ti:Sapphire laser was studied. New energy transfer process, such as upconversion from terminal level of the 3.9 μm laser was observed in high concentration Ho^{3+} doped BaY_2F_8.

Finally, we proposed to use high-energy flashlamp pumped tunable Cr:LiSAF laser operating in long pulse regime for the direct pumping of the upper level of the 3.9 μm laser. Pulsed laser oscillation at 3.9 μm is demonstrated in Ho^{3+} doped BaY_2F_8 with low threshold of 3 mJ and a slope efficiency of 14.5 % with maximal energy of 30 mJ.

The second part of the thesis describes the design and the development of the visible $Pr:LiYF_4$ laser for holography at 640 nm resonantly pumped by the frequency-doubled flashlamp pumped tunable Cr:LiSAF laser at 444 nm.

Reproduced with permission of the copyright owner. Further reproduction prohibited without permission.

To my parents Silva and Lev Murazian

my daughter Alissa

and my husband Nelson

Reproduced with permission of the copyright owner. Further reproduction prohibited without permission.

ACKNOWLEDGEMENTS

I wish to express my sincere appreciation to my thesis supervisor, Dr. Hans P. Jenssen, for his guidance and encouragement throughout this work. His expertise and excellent intuition were an inspiring example for me. I will remember our exciting scientific discussions, which very often motivated me to come up with new ideas and concepts. His patience has been an invaluable source of support, and his critical comments have greatly helped me in my professional growth.

I would also like to thank my co-advisor Dr. Michael Bass for his unfailing support and helpful discussions. I would like to acknowledge Dr. W. Silfvast for his interest in my new 3.9 μm laser and very valuable comments. Special thanks to Dr. B. Zel'dovich for being such a great teacher and for his constant support throughout my graduate years. I would also like to thank Dr. Arlete Cassanho for growth of many crystals used in this thesis.

A note of thanks to fellow graduate students for helpful discussions and support in non-technical matters that I have valued very much. Special thanks go to all of my dear friends at School of Optics.

Finally, I want to thank my parents, my husband and my daughter for steady encouragement and moral support throughout my graduate study.

Reproduced with permission of the copyright owner. Further reproduction prohibited without permission.

TABLE OF CONTENTS

Reproduced with permission of the copyright owner. Further reproduction prohibited without permission.

Reproduced with permission of the copyright owner. Further reproduction prohibited without permission.

LIST OF TABLES

Reproduced with permission of the copyright owner. Further reproduction prohibited without permission.

LIST OF FIGURES

Reproduced with permission of the copyright owner. Further reproduction prohibited without permission.

Reproduced with permission of the copyright owner. Further reproduction prohibited without permission.

Reproduced with permission of the copyright owner. Further reproduction prohibited without permission.

Reproduced with permission of the copyright owner. Further reproduction prohibited without permission.

CHAPTER 1. INTRODUCTION

This thesis describes a series of experiments and theoretical studies, which led to the development of two new solid state laser systems. The most significant achievement reported in this work is prediction, analysis and actual demonstration of the efficient, room temperature mid-infrared solid state laser at 3.9 μm in Ho^{3+} doped BaY_2F_8. The second part of the thesis describes the design and the development of the visible $Pr:LiYF_4$ laser at 640 nm for holography.

For well over two decades now a solid state laser operating in the 3 to 5 μm wavelength range, which falls into mid-infrared atmospheric transmission window, has been the subject of intense research and development efforts. Numerous applications, such as remote sensing, infrared countermeasures, illumination for space-based lasers, imaging, eye-safe lidars, environmental agent detection, etc., require a frequency agile mid-infrared lasers operating at one or multiple different wavelengths spanning the 3-5 μm range and beyond. In some of these applications, the laser is required to operate in a pulsed mode, while others dictate cw or quasi-cw mode operation. Other requirements may include overall good beam quality and multi-wavelength capability. In most cases, the laser source must be scalable to high average powers and have the potential for high efficiency, all from a compact, reliable and ruggedized package. A mid-infrared source based on a solid state laser, therefore, was expected to meet such a demanding set of requirements.

Reproduced with permission of the copyright owner. Further reproduction prohibited without permission.

Thus the initial motivation for the first part of this work was an investigation of the feasibility of developing a mid-infrared solid state laser source at 3.9 μm wavelength. As laser materials we chose fluorides: BaY_2F_8 (BYF) and $LiYF_4$ (YLF) that incorporate trivalent rear-earth ions of Ho^{3+} as active ions. In the Chapters 3, 5 and 6 we present the results of spectroscopic evaluations and numerical modeling of energy transfer processes between rare earth ions of Ho^{3+} doped into host laser crystals. A thorough study and understanding of the processes occurring in these laser materials allowed us to propose new principles for achieving laser action at 3.9 μm, to test several efficient excitation techniques, and to optimize operation characteristics of the actual laser. Three different pumping and lasing schemes of the 3.9 μm laser have been suggested and studied.

First (Chapter 4), short pulse resonant pumping at 532 nm by a Q-switched frequency doubled Nd:YAG laser and cascade lasing at 1.4 μm, and 3.9 μm was achieved with low thresholds of 1 mJ and 5 mJ, respectively, and a slope efficiency of 10.4% for the 3.9 μm Ho:BYF laser.

In the second excitation scheme (Chapter 5), the feasibility of achieving laser action at 3.9 μm with cw resonant cascade pumping at 750 nm by a Ti:Sapphire laser was studied, by taking advantage of a fortuitous coincidence of ground state absorption and excited state absorption, combined with the strong cross-relaxation processes in high concentration samples. A numerical model, based on a system of coupled nonlinear rate equations, for calculation of the population dynamics of the Ho^{3+} energy levels was developed (Chapter 5). This model allowed determination of steady state values for the populations of the several energy levels at different pump intensities as well as their temporal development. It predicted, initially, that laser action at 3.9 μm with cw pumping

Reproduced with permission of the copyright owner. Further reproduction prohibited without permission.

at 750 nm would be self-terminating due to the unfavorable lifetime ratio of the upper and lower levels of the 3.9 μm transition.

In order to check the results of model calculations, we performed Z-scan measurements of nonlinear transmission and of fluorescence intensity from various energy levels as a function of the pump intensity (Chapter 5). The numerical model is in good agreement with the Z-scan measurements of fluorescence for Ho:YLF. In Ho:BYF, however, we discovered new energy transfer processes that efficiently deplete the lower level ($^5I_6$) of the 3.9 μm transition, and could be used to break the bottleneck created by the long lifetime of that level. We performed the measurements of visible fluorescence with cw near-IR laser excitation at 750 nm (Chapter 5) in order to determine the nature of energy transfer processes that can deplete the long lived $^5I_6$ manifold. Based on experimental observations, we came to the conclusion, that one such process is the strong upconversion from the $^5I_6$ level in high concentration Ho:BYF. We have also suggested, that another process, responsible for the depletion of the $^5I_6$ level, is the excited state absorption. The numerical model for the 3.9 μm Ho:BYF laser with cw pumping at 750 nm was upgraded by taking into account the depletion of the lower level of the 3.9 μm transition, and the values of the pump intensity required for achieving inversion of population have been estimated.

As a third alternative pumping scheme of the 3.9 μm laser, the author suggested the new idea of linear down conversion in Ho doped BYF or YLF by direct long pulse resonant pumping of upper laser level at 890 nm by a flashlamp pumped Cr:LiSAF laser (Chapter 6). This new approach was based on the results of experimental measurements of fluorescence transients from the participating energy levels (Chapter 6) and theoretical

Reproduced with permission of the copyright owner. Further reproduction prohibited without permission.

calculations of the temporal development of populations of the same levels (Chapter 6), which provided evidence that direct pumping of the upper level $^5I_5$ of the 3.9 μm transition will increase the power efficiency of the 3.9 μm laser. Pulsed laser oscillation at 3.9 μm involving the $^5I_5$ and $^5I_6$ manifolds was demonstrated for Ho^{3+} in BaY_2F_8 pumped at 890 nm by a flashlamp pumped long pulse Cr:LiSAF laser for the first time. Laser threshold was achieved at 3 mJ of pump energy. Slope efficiencies of up to 14.5% were demonstrated with maximum energy of 31 mJ of 3.9 μm laser pulse.

The goal of the second part of this thesis, described in Chapter 7, was to develop an efficient visible pulsed laser system for holography. Lasers, which have balanced mix of red, green, and blue wavelengths, have many important present and future applications, particularly in color laser imaging in all of its various aspects. Pr:YLF was used as a laser gain material because it can offer visible red, green, and blue emission from a solid state laser. We have designed and constructed a laser system that is a prototype for low energy testing of an actual holographic laser. It is a 640 nm high coherence length Pr:YLF laser resonantly pumped by a frequency doubled flashlamp pumped tunable Cr:LiSAF laser at 444 nm.

We have demonstrated efficient long pulse Cr:LiSAF laser tuned to 890 nm with up to 1.5 J pulse energy and 50 μs pulse duration. The discussion of the design and optimization of the Cr:LiSAF laser used as a pump source for both the mid-infrared 3.9 μm laser and the 640 nm Pr:YLF laser, is presented in the Chapter 7.

Reproduced with permission of the copyright owner. Further reproduction prohibited without permission.

1.1. Properties of Rare-Earth Ions in Solids

1.1.1. Energy levels

The rare-earth ions are characterized by partially filled 4f shells within the closed shell configuration of xenon [1]. Optical transitions take place between the energy levels of the $4f^N$ ground configuration. The degeneracy of the $4f^N$ configuration is split by the coulomb interaction of the electrons yielding terms ^{2S+1}L with separation on the order of 10^4 cm^{-1}. The ^{2S+1}L degeneracy is split by spin-orbit interaction into multiplets of $^{2S+1}L_J$ with separations on the order of 10^3 cm^{-1}. Finally, the 2J+1 free-ion degeneracy is further reduced by the static crystal field into the Stark components with separation on the order of 10^2 cm^{-1}. Since the 4f electrons are well shielded from the surrounding crystal environment by the filled $5s^2 5p^6$ shells, the energy levels retain an atomic character similar to those of triply ionized rare-earth ions in a gas, and the positions of the energy multiplets vary little from host to host. A good approximation of the energy levels in any material can be found from the Dieke chart [2], which summarizes the positions of energy levels of the rare-earths in $LaCl_3$.

1.1.2. Relaxation mechanisms

A rare-earth ion in an excited multiplet can decay to a lower energy state through one of the following several mechanisms:

(1) *Multiphonon relaxation*, in which the energy is taken up by lattice vibrations. Not only do phonons affect the optical transitions between manifolds and bring the excited ions within the manifold to equilibrium, they also can cause transitions between different manifolds. This process is called multi-phonon relaxation; generally the optical

Reproduced with permission of the copyright owner. Further reproduction prohibited without permission.

phonons are thought to be involved in this process as the bridged energy gaps can be on the order of the thousands of wavenumbers. Partlow and Moos [3] have found the following empirical relationship between the multiphonon relaxation rate and the energy gap, ΔE, between that multiplet and the one below it:

$$W_{mp} = C \exp(-\theta \Delta E)$$

where C and θ are constants characteristic of the host material.

The multiphonon relaxation rate, therefore, depends on the host material and the energy gap ΔE, but not on the type of ion or its concentration. Since this non-radiative relaxation limits the lifetimes of manifolds which lie energetically close to lower manifolds, the lifetimes of the manifolds of a rare-earth ion are dependent on the phonon spectrum of the host.

(2) *Radiative transition,* in which the energy is emitted as a photon. Since optical transitions of rare-earth ions take place between the states of the $4f^N$ ground configuration, electric dipole transitions are parity forbidden for the free ion. However, if the ion is placed in a crystal field lacking inversion symmetry, wavefunctions of different parities mix. In the rare-earths, the inter-mixing of the $5d\text{-}4f^{N-1}$ and $4f^N$ wavefunctions allows electric dipole transitions to occur between different $4f^N$ shell configurations [4]. Magnetic dipole and electric quadruple transitions are allowed, but their contributions to a radiative decay are usually small, except when $\Delta J = 0$ or ± 1, in which case magnetic dipole contributions can be significant. The radiative transition probability depends on

Reproduced with permission of the copyright owner. Further reproduction prohibited without permission.

the particular states involved and the host material, but not on the dopant concentration [5].

(3) *Non radiative or radiative energy transfer* in which all or part of the energy of the excited ion (called the donor or the sensitizer) excites a nearby ion (called the acceptor or the activator) into a higher energy state. The transfer is not radiative if no photon is involved, but it is radiative if the donor actually emits the photon, which is then absorbed by the acceptor. The mechanisms responsible for non-radiative energy transfer have been attributed to electric and magnetic multipolar interactions and exchange interactions between the donor and the acceptor [6,7,8]. Since these interactions become stronger as the donor/acceptor separation decreases, non-radiative transfer becomes more probable with increasing dopant concentration.

Figure 1 shows examples of the types of energy transfer that have been observed in materials doped with rare-earth ions. The transfer is resonant if the energy given up by the donor equals that taken up by the acceptor. In non-resonant transfer, the energy mismatch must be made up by lattice vibrations.

Cross-relaxation (or self-quenching) refers to the transfer between ions of the same species. In this process, an ion in a high lying level falls to an intermediate level while promoting another ion from the ground state to a higher level.

Energy migration refers to the hopping of excitation among the donors. An excitation is transferred resonantly between the same manifolds of two ions. This mechanism, while not visibly changing the spectra or lifetimes of the manifold by itself, allows excitations to diffuse away from the location of the initial excitation until it finds an acceptor or decays on its own.

Reproduced with permission of the copyright owner. Further reproduction prohibited without permission.

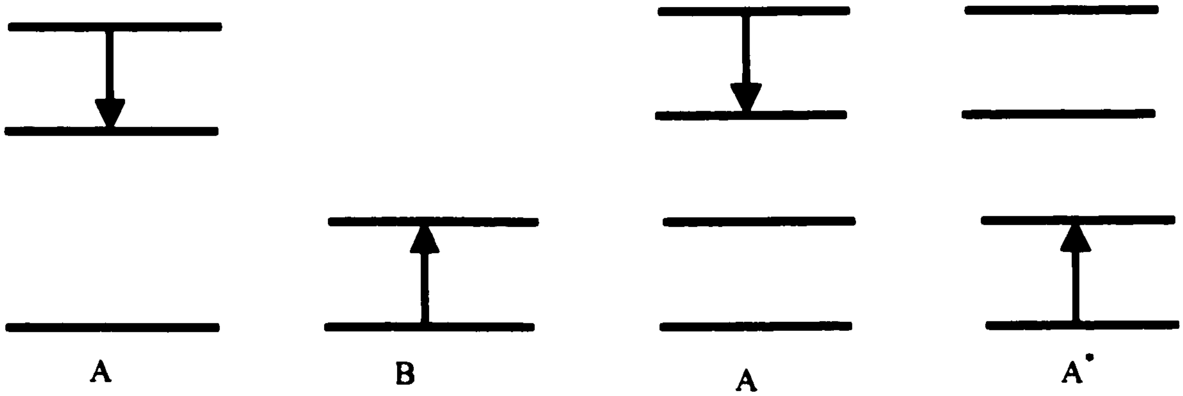

Resonant transfer

Cross-relaxation (Self-quenching)

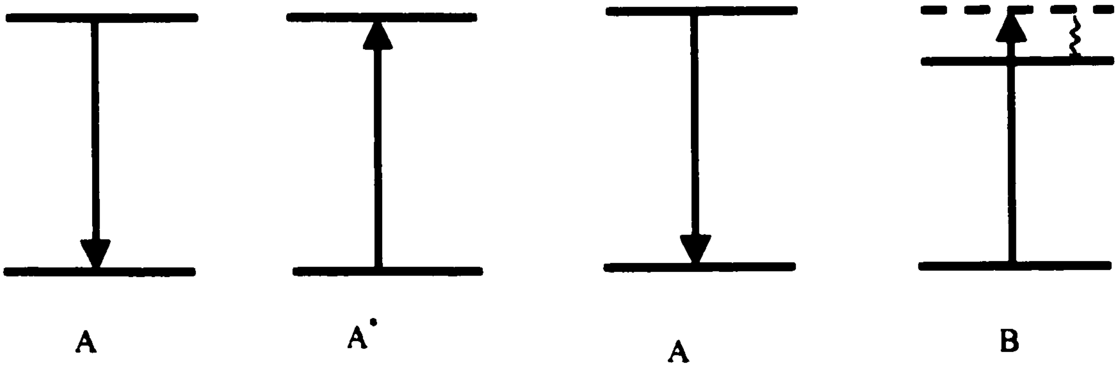

Energy migration

Non-resonant transfer

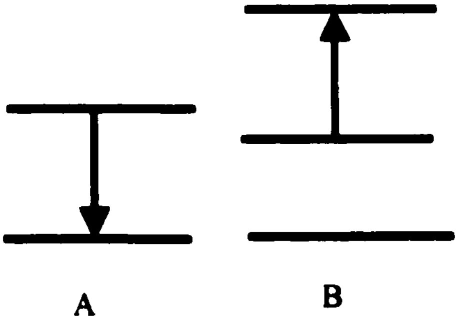

Upconversion

Figure 1. Examples of the types of energy transfer processes in rare-earth activated materials.

Reproduced with permission of the copyright owner. Further reproduction prohibited without permission.

Upconversion is a transfer process where one or more of the initial states are an excited state. Here an ion in an intermediate state falls to a lower state while promoting another ion in an intermediate state to a higher state. Since the interaction between rare-earth ions is fairly weak, the upconversion is probable only for closely spaced excitations. The rate of upconversion will obviously increase with the density of excitations, as well as with higher dopant concentrations. Upconversion is also important for practical reasons. Because rare earth doped solid state lasers often operate with a large fraction of the dopant ions in excited states, upconversion can become a macroscopically observable process. While this offers the possibility of increasing efficiency for some important transitions, upconversion greatly complicates the population dynamics of the energy levels of rare-earth ions in laser material.

The quantum-mechanical theory of resonant energy transfer was first developed by Forster in the dipole approximation [6]. Dexter [7] generalized the theory to higher-order interactions. Reviews of the theoretical background have been given by Watts [9], Bernard et. al. [10] and Di Bartolo [11].

Energy transfer mechanisms have played an increasingly important role in laser material research, since they provide effective means of moving energy around in the material without a large amount of heat dissipation. A scheme that has been successfully employed for efficiency improvements through energy transfer is called *sensitization*. In such a scheme, a species of ions, called sensitizers, which are good absorbers of the pump radiation are introduced into the material. If the sensitizer is able to efficiently transfer

Reproduced with permission of the copyright owner. Further reproduction prohibited without permission.

the absorbed pump energy to the activator, it effectively complements the pump band of the activator ions and leads to a higher pumping efficiency.

Reproduced with permission of the copyright owner. Further reproduction prohibited without permission.

CHAPTER 2. IR LASER TRANSITIONS IN HO^{3+} AND MID-INFRARED 3.9 µM LASER

2.1. Motivation and comparison with alternative methods of achieving the mid-IR laser oscillation

Lasers that operate in the mid-infrared region are of great interest to the technical community. For well over two decades now a solid state laser operating in the 3 to 5 µm wavelength range, which falls into mid-infrared atmospheric transmission window, has been the subject of intense research and development efforts. Applications include remote sensing, countermeasures, illumination for space-based lasers, imaging, eye-safe lidars, environmental agent detection, to name a few.

In recent years, the main options considered for frequency-agile lasers in the mid-infrared, especially beyond 3 µm, were directed at down shifting of some shorter wavelength radiation using a nonlinear conversion process such as an optical parametric oscillator (OPO) or Raman conversion. While capable of providing wavelengths beyond 3 µm, frequency conversion methods suffer from a number of drawbacks including optical system complexity and degraded reliability due to potential damage to the nonlinear crystal used for an OPO or beam quality degradation in the case of Raman shifting in gases. Furthermore, both methods generally require a high peak power (i.e.,

Reproduced with permission of the copyright owner. Further reproduction prohibited without permission.

short pulse) pump laser for efficient radiation conversion. Consequently they do not lend themselves well to cw, quasi-cw or long pulse applications.

Another alternative method for obtaining laser radiation in mid-infrared is direct emission from semiconductor lasers. Among the main drawbacks of semiconductor lasers are poor beam quality and the overall complexity due to the need for low temperature operation. It is generally accepted, therefore, that a mid-IR source based on a solid state laser operating at room temperature is the preferred technology path.

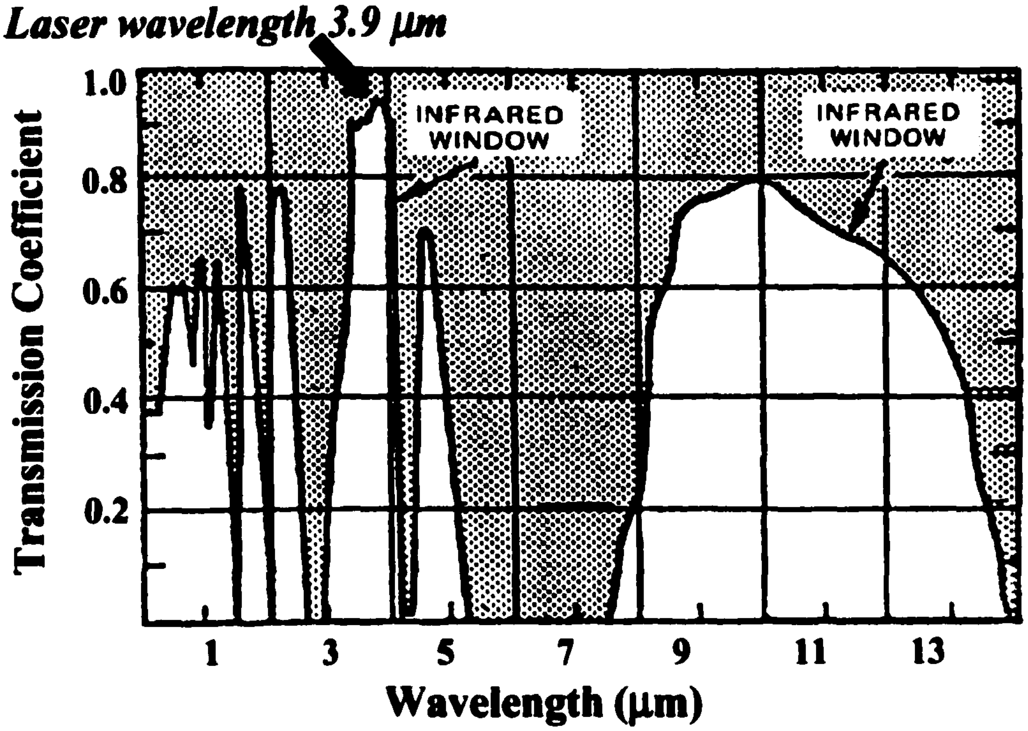

Figure 2. Infrared atmospheric transmission spectrum.

The rare-earth doped fluorides are attractive laser materials for operation in the mid-infrared spectral region. They can be incorporated in rugged and compact systems,

Reproduced with permission of the copyright owner. Further reproduction prohibited without permission.

which can be operated at high peak powers. These lasers can provide overall good beam quality and multi-wavelength operation capability.

The initial motivation for this work was to determine the optimal conditions for achieving 3.9 μm laser emission from the holmium-doped fluoride crystals Ho:YLF and Ho:BYF through the series of theoretical calculations and experimental measurements. The 3.9 μm wavelength matches peak of mid-IR atmospheric transmission window (see Figure 2), which makes it very important for applications mentioned above.

2.2. Infrared laser transitions in Ho^{3+}

It is well known that Ho^{3+} ions are capable of producing stimulated emission at several wavelengths across the infrared. Laser emission from trivalent holmium is normally associated with the $^5I_7$ - $^5I_8$ transition in the 2 μm region. Barnes et al. [12] have reported on low temperature operation (ca. 80° K) of an αβHo:YLF laser in a TEM$_{00}$ Q-switched mode with up to 150 mJ per pulse. Studies of laser emission have been reported on fluorescence transitions appearing at 2.4 and 2.9 μm, in addition to the familiar transition at 2.1 μm [13]. A. M. Morozev, et al. [14] and Podkolozinia et al. [15] have demonstrated numerous laser transitions in LiHoF$_4$ and 2% Ho:YLF at low temperatures including the $^5S_2$ - $^5I_7$ transition in the 750 nm region. E. P. Chicklis et al. [16] have reported laser operation of this transition in 2% Ho:YLF at room temperature. They utilized both flashlamp and dye laser pumps as the excitation mechanism. A green laser pump from a frequency doubled, Q-switched Nd:YAG laser at 532 nm was also successfully used by Knights et al. [17] to pump Ho:YLF producing short pulse radiation at 750 nm at room temperature with high efficiency and repetition rates as high as 40 Hz.

Reproduced with permission of the copyright owner. Further reproduction prohibited without permission.

Operation down to 4.2° K has allowed oscillation at several laser transitions to the ground $^5I_8$ state both in infrared, at 1153 nm, 889.7 nm, as well as in visible, at 645.4 nm and 540.8 nm. Ho:YLF and $LiHoF_4$ lasers were demonstrated at 979 nm at room and low temperatures [14]. Cooling of these lasers, with the terminal laser level being either ground state or manifolds with longer lifetime, allowed obtaining laser oscillation with much lower threshold by essentially unpopulating the lower laser level and achieving quasi-four level operation.

The energy level structure of Ho^{3+} doped fluorides [14] also lends itself to operation as a cascade laser. Multiple transitions can be lased from the single solid state medium. In the reference [18] cascade laser action has been observed in 1% Ho^{3+}-doped YLF using short pulse resonant pumping at 535 nm by frequency-doubled Nd:glass laser. Two sets of cascade laser transitions, the $^5S_2$ - $^5I_5$, $^5I_5$ - $^5I_6$ (1.392 μm, 3.914 μm) and $^5S_2$ - $^5I_5$, $^5I_5$ - $^5I_7$ (1.392 μm, 1.673 μm), were successfully lased. Shortly thereafter, Eckart et al [19] reported a three line sequential laser emission at 3.4 μm, 3.9 μm and 2.9 μm in Ho:YLF. Room temperature cascade laser action was obtained by resonantly pumping the $^5S_2$, $^5F_4$ manifold with 535.5 nm laser radiation from a pulsed dye laser with a 1 μs long pulse.

There are a number of publication, describing multiple mid-infrared laser transitions in Ho^{3+} doped fluoride-glass fiber lasers. In the reference [20] cw laser operation of Ho^{3+}-doped ZBLAN multimode fiber, emitting within the range 2.83-2.95 μm, was achieved by optical pumping with dye-laser at 640 nm. Dual-wavelength cw cascade laser oscillation at 3 μm and 2 μm with a holmium-doped fluoride-glass fiber laser pumped by a Ti:Sapphire laser at 890 nm was reported in the reference [21].

Reproduced with permission of the copyright owner. Further reproduction prohibited without permission.

Several publications report the demonstration of lasing in fibers at 3.9 μm – the wavelength of our interest. In the reference [22] the demonstration of a superfluorescent fiber source at 3.9 μm (77 K) with resonator mirrors was reported. Few months later the same author realized a cw laser at 3.9 μm [23]. The Ho^{3+} doped fluoride fiber was pumped around 640 nm and cascade laser action was achieved at 3.9 μm and 1.2 μm. In the following publication by the same group [24], laser action at 77 K was demonstrated for two different pump wavelength ranges, 640 nm and 890 nm. Lasing at 3.9 μm was achieved with a cascade laser scheme with the laser at 1.38 μm, followed by the 3.9 μm laser, and then the 1.2 μm laser.

2.3. Choice of host material for mid-infrared laser

The extension of laser operation from rare-earth ions in crystals into the mid-infrared is severely limited by nonradiative decay induced by ion-lattice interaction. The heavier the host ions and the lower their binding forces in the crystalline host, the lower the energy of the lattice vibrations or the phonons. Therefore, the possibility of obtaining laser emission from Ho^{3+} at 3.9 μm depends to a great extend on the choice of host crystal. An important requirement for efficient conversion is that the fluorescence lifetime of the intermediate states should be long. Since the lifetimes of these states are often governed largely by nonradiative decay to lower lying states, it is necessary that the optical phonon energies of the host crystal be relatively small and/or the orbital coupling of the ion to the lattice be relatively weak. These are also characteristics, which will permit fluorescence and stimulated emission to occur at longer wavelengths in the

Reproduced with permission of the copyright owner. Further reproduction prohibited without permission.

infrared. Therefore, we have concentrated our attention on fluorides, BaY_2F_8 and $LiYF_4$, where these conditions are satisfied.

The ability to sustain laser oscillation between two given levels is enhanced in fluorides over oxides in many cases because the multiphonon decay rates in fluorides are generally lower. A reduction in the upper state multiphonon decay rate generally means a larger product of the upper state lifetime with the stimulated emission cross section, and therefore a lower cw threshold. The lower refractive indices of fluorides also lead to higher products of stimulated emission cross section with fluorescence lifetime, and therefore lower cw laser thresholds. Fluorides have been found to be less susceptible to thermal lensing than oxides. In many cases they can provide better beam quality at high powers.

2.3.1. $LiYF_4$

$LiYF_4$ (YLF) is a uniaxial crystal, which is optically transparent throughout the visible and up to its absorption edge at 5 μm in infrared. The unit cell is tetragonal with lattice cell parameters a = 526 pm and c = 1094 pm [25] and contains 4 formula units per unit cell. Rare earth ions substitute into the Y^{3+} site, which has site symmetry S_4. YLF is a popular host material because of its low index refraction, low phonon energies and good chemical stability. The high band gap in the ultraviolet not only leads to low linear absorption, but also to low nonlinear refractive indices and multiphonon absorption [26].

2.3.2. BaY_2F_8

BaY_2F_8 has good optical properties: it is transparent from its infrared absorption edge at 9 μm through the visible to beyond 200 nm in the UV [27]. The optical phonon

Reproduced with permission of the copyright owner. Further reproduction prohibited without permission.

energies of BYF are relatively small with the maximum phonon energy of approximately 415 cm^{-1} [28], and it has low nonradiative multiphonon relaxation rates (in comparison to oxides and garnets) [13].

BaY_2F_8 (BYF) is in many ways comparable to $LiYF_4$; the crystal can be grown the same way, and the mechanical and chemical properties are almost the same. But there are important differences. Single crystals of BYF belong to the monoclinic space group C^3_{2h}. The crystallographic axes of this crystal are not orthogonal: the **b**-axis is perpendicular to both **a** and **c**, but the **a** and **c** are separated by 99.7 degrees, allowing the x and z axes of the index of refraction tensor to shift from the crystallographic axes (Figure 3). The lattice constants are: a = 697.2 pm, b = 1050 pm, c = 426.0 pm [29].

Rare earth ions enter substitutionally into the Y^{3+} site, which has site symmetry C_2. As a biaxial crystal, BYF exhibits dispersion in the orientation of its optical axes in the a-c plane. No dispersion of the axes is allowed in the b-a or b-c plane due to symmetry constraints [30].

Three refractive indices are needed to describe the dielectric properties of BYF. The refractive indices have been measured as function of the wavelength in the spectral region 275 nm – 2.65 μm with the method described by Bond [31] which gives in addition to the numerical values of the indices, the direction of the main axes x, y, and z of the index ellipsoid with respect to the crystallographic axes a, b, and c . Visual inspection of BYF crystals between crossed polarizers gives a value for angle ρ between the c and z axes around 23°.

Reproduced with permission of the copyright owner. Further reproduction prohibited without permission.

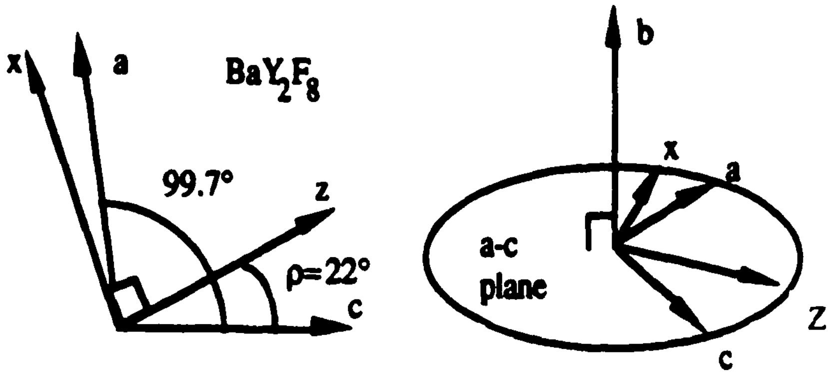

Figure 3. Crystallographic (a, b, c) and optical (x, y, z) axes in BaY_2F_8 [32].

The fluorescence lifetimes of the intermediate states of rare-earth ions in BYF are relatively long. The limit of measurable fluorescence was given by Shinn et al. [33], who stated that the luminescence is totally quenched only if less than four phonons are required for the transition and the transition will occur totally by means of radiative emission if more than ten photons are necessary. The approximate energy gap determines the number of phonons involved in the transition. About six phonons are required for 3.9 μm transition in Ho^{3+} doped fluorides BYF and YLF, which allows luminescence at this wavelength, and makes these crystals attractive materials for realizing mid-infrared laser sources.

Reproduced with permission of the copyright owner. Further reproduction prohibited without permission.

CHAPTER 3. EXPERIMENTAL METHODS FOR INITIAL SPECTROSCOPIC EVALUATIONS

3.1. Absorption measurements

Absorption measurements refer to measurements of the attenuation of light as it passes through material. They can be used not only for determination of the position of energy levels, but also to find the absorption cross-section of a dopant and to measure dopant concentrations.

Absorption and transmission measurements were performed with a Perkin-Elmer 330 and Cary 500 spectrophotometers. Both instruments are a dual-beam comparator devices, with the signal taken to be the ratio of intensities of the sampling beam and the reference beam. The data scans were controlled and stored with a computer. The spectral resolution was generally set to 0.5 nm. Polarized measurements were made by placing a matched set of Glan-Thompson polarizers in the sample and reference beam. The system performed a self-calibration at start up; and the response for any particular configuration of the sample compartment (polarizer, apertures, etc.) was corrected by performing a background calibration scan. Spectra were measured by the instrument in dimensionless units of absorbance (A), where A was given by the relationship $I_S/I_R = 10^{-A}$. Here I_S is the intensity of the beam passing through the sample, and I_R is the intensity of the reference

Reproduced with permission of the copyright owner. Further reproduction prohibited without permission.

beam. Absorbance data were used for the calculations of absorption coefficient in units of [1/cm] with the following formula $\alpha = A \cdot \ln 10 / L$ (here L is the thickness of the sample). Absorption spectra of Ho:BYF, Ho:YLF were used to determine the cross sections of the transitions from the ground level $^5I_8$ to upper levels (Figure 4). For three different pumping schemes of 3.9 µm laser, described in Chapter 4-6, was essential to know the ground state absorption cross sections at 532 nm, 750 nm and 890 nm wavelength ranges.

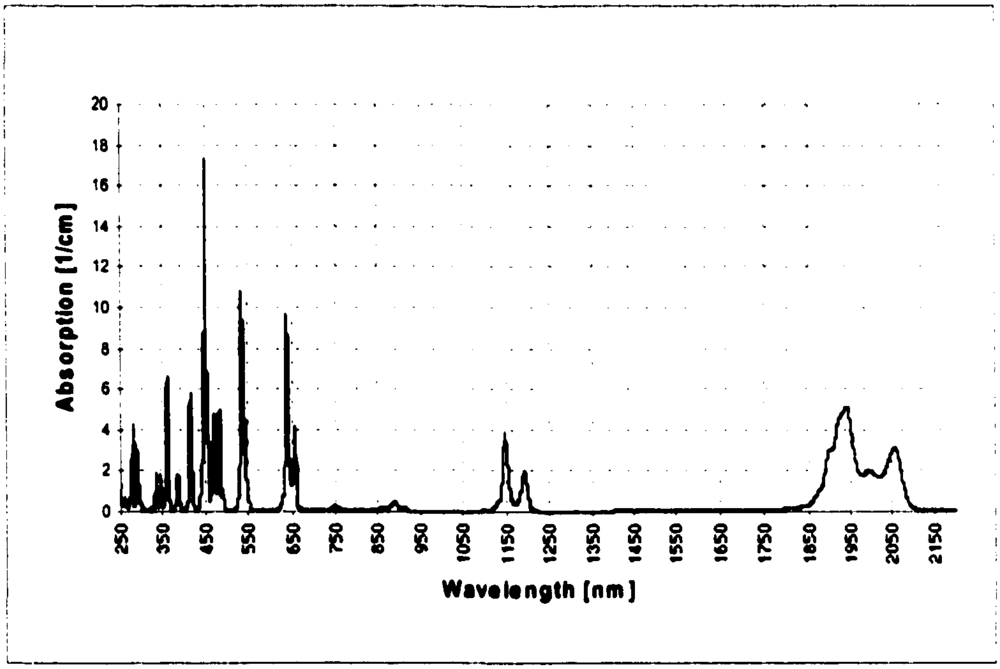

Figure 4. Absorption spectrum of 10% Ho:BYF (random polarization).

Both Ho:BYF and Ho:YLF exhibit strong absorption lines in the visible wavelength range, including the line around 532 nm, which corresponds to $^5I_8 \rightarrow {^5F_4}$ ($^5S_2$). In order to make accurate measurements of the peak of absorption around 535 nm,

Reproduced with permission of the copyright owner. Further reproduction prohibited without permission.

we used lower concentration samples. For the measurements of the absorption cross section at 532 nm we used higher concentration samples. Spectra measured for two different polarizations of light relative to c-axis of uniaxial YLF doped with 2% Ho^{3+} ions are shown in Figure 5. Absorption is significantly stronger in the π–polarization with absorption coefficient α = 0.6 cm^{-1} at 532 nm or cross section σ = $2.2\cdot10^{-21}$ cm^2. Absorption spectrum of 10%Ho:BYF in the same wavelength range is shown in Figure 6 For polarization of light parallel to b-axis of crystal we measured α = 2.4 cm^{-1} at 532 nm or cross section σ = $1.8\cdot10^{-21}$ cm^2.

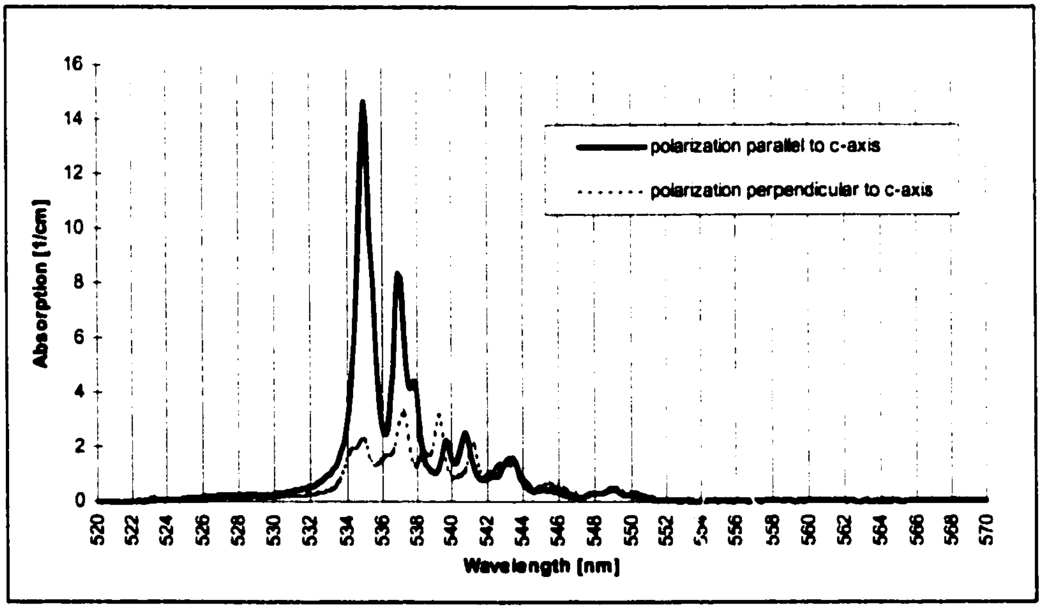

Figure 5. Absorption spectrum of 2% Ho:YLF for 2 different polarizations of light relative to c-axis.

Reproduced with permission of the copyright owner. Further reproduction prohibited without permission.

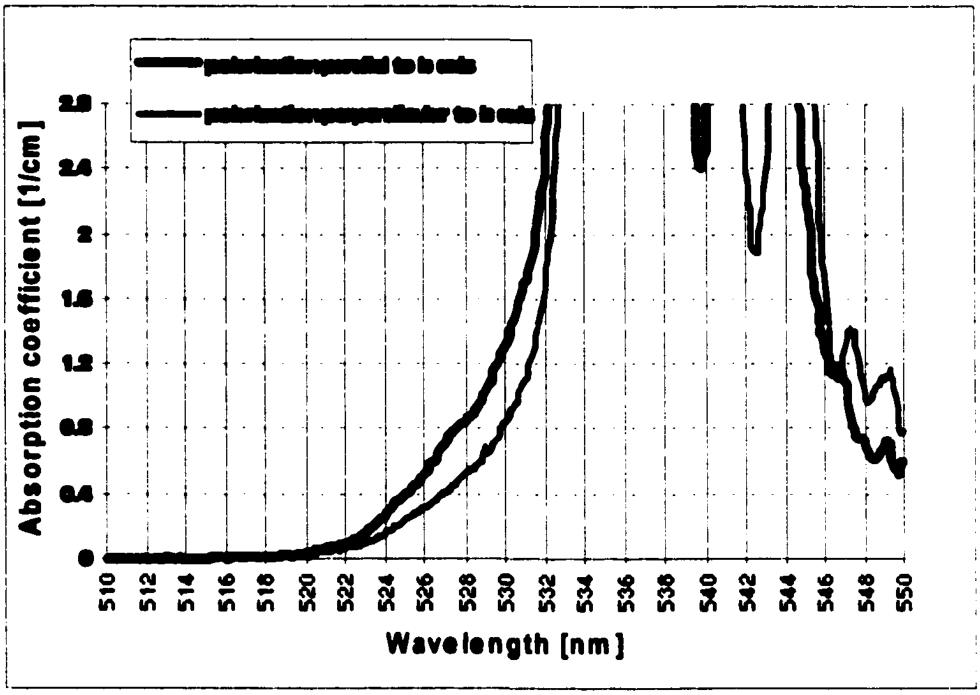

Figure 6. Polarized absorption spectrum of 10% Ho:BYF in the 532 nm range.

Higher concentration samples and/or longer samples were used for the measurements of the very weak absorption line from ground level at ~ 750 nm. The results of measurements for ground state absorption at ~ 750 nm ($^5I_8 \rightarrow {}^5I_4$) in Ho:BYF and Ho:YLF are shown in Figures 7 and 8, respectively. The strongest absorption coefficient in 10% Ho:BYF was measured at 748 nm for polarization parallel to b-axis of the crystal: $\alpha = 0.104$ cm^{-1} and cross section $\sigma = 8 \cdot 10^{-23}$ cm^2. The strongest peak in absorption spectrum of 100% Ho:YLF was observed at exactly 750 nm for polarization parallel to c-axis: $\alpha = 1.3$ cm^{-1} and cross section $\sigma = 9.3 \cdot 10^{-23}$ cm^2.

Figure 9 illustrates the absorption spectrum of 10% Ho:BYF for light polarized parallel and perpendicular to b-axis of the crystal, with the peak of absorption at 888 nm

Reproduced with permission of the copyright owner. Further reproduction prohibited without permission.

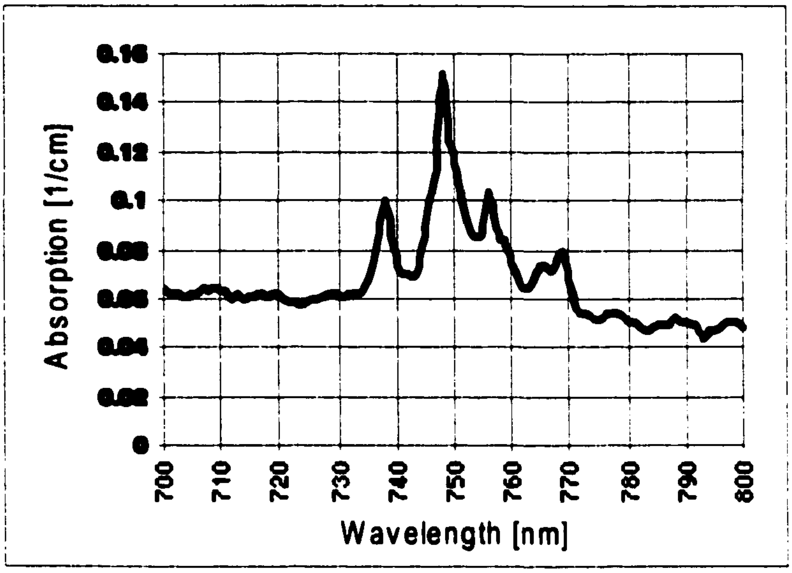

Figure 7. Ground state absorption of Ho:BYF 10% around 750 nm (polarization parallel to b-axis).

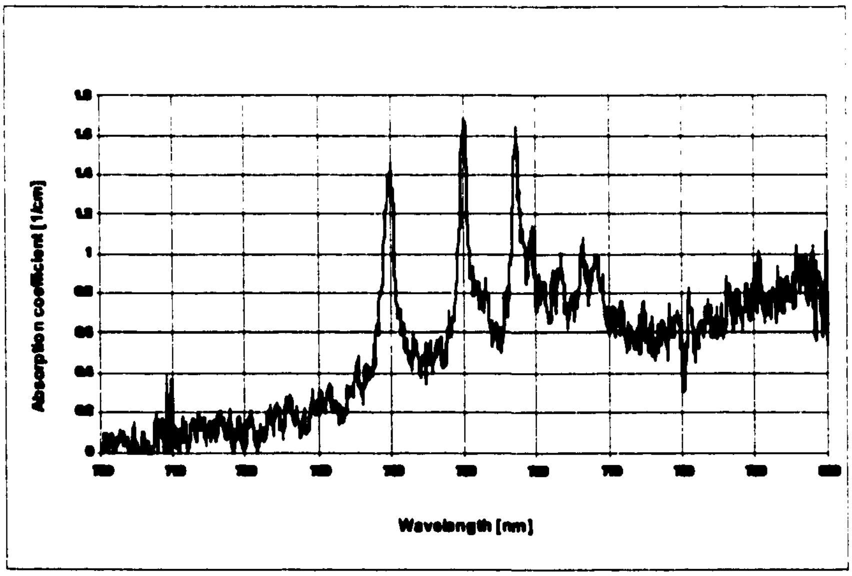

Figure 8. Ground state absorption of Ho:YLF 100% around 750 nm (polarization parallel to c-axis).

Reproduced with permission of the copyright owner. Further reproduction prohibited without permission.

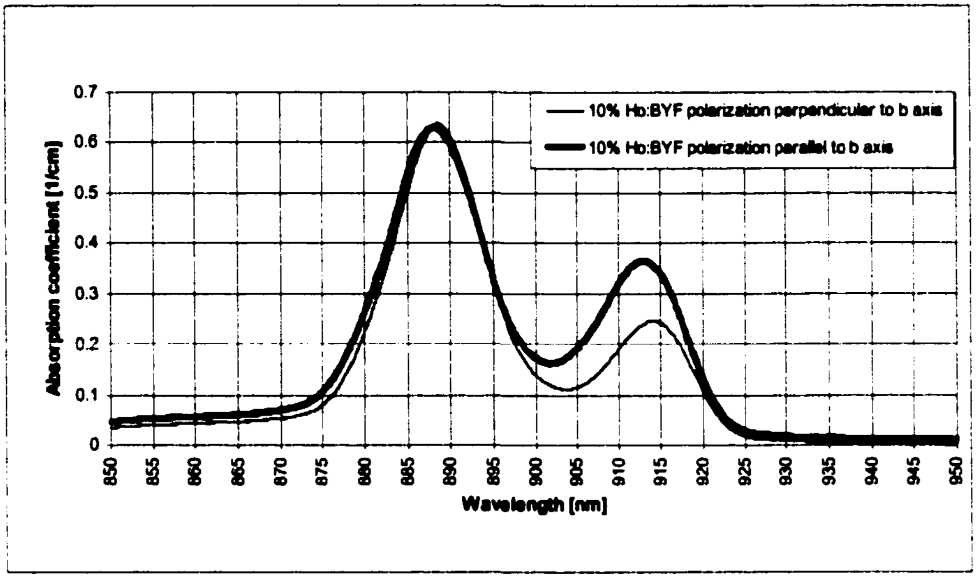

Figure 9. Absorption spectrum of 10% Ho:BYF around 890 nm for light polarized parallel and perpendicular to b-axis of the crystal

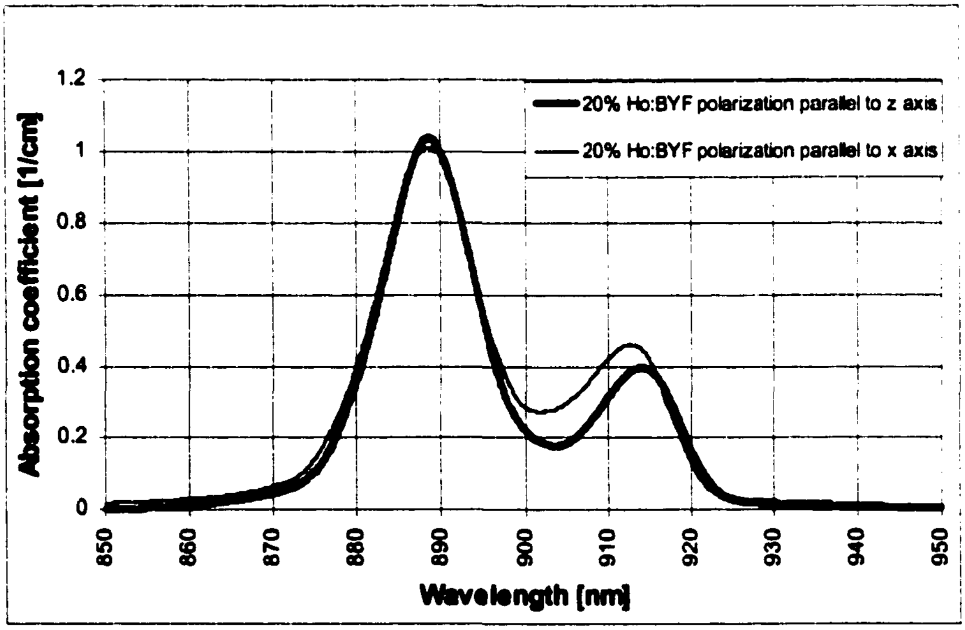

Figure 10. Absorption spectrum of 20% Ho:BYF around 890 nm for light polarized parallel to z- and x-axes of the crystal.

Reproduced with permission of the copyright owner. Further reproduction prohibited without permission.

and absorption coefficient $\alpha = 0.63$ cm^{-1} for both orientations. The absorption spectrum of the 20% Ho:BYF is shown in Figure 10. The following absorption coefficients for two different orientations of the crystal were measured: $\alpha = 1.002$ cm^{-1} for polarization of light parallel to x-axis and $\alpha = 1.04$ cm^{-1} for polarization of light parallel to z-axis.

3.2. Emission and excitation measurements

The fluorescence spectrum of a material is a measure of the spontaneous emission intensity as a function of wavelength (or energy). It can be used to determine the positions of energy levels and to calculate energy transfer parameters. It also can be transformed into the stimulated emission cross-section.

For the initial set of fluorescence emission and excitation spectra we used a double SPEX spectrofluorimeter. It has two double-grating monochromators in the excitation and emission positions. The source of radiation is a Xenon arc lamp. The light from the lamp was filtered by an excitation spectrometer that allows only one wavelength to reach the sample, which is positioned in special sample compartment. The emitted radiation was filtered by an emission spectrometer that was feeding the signal to a detector photomultiplier. Scanning the emission spectrometer with stationary excitation wavelength produces a spectrum of radiation emitted by the sample. Scanning the excitation spectrometer with a constant emission wavelength yields an excitation spectrum. A polarizer and a filter were placed between the sample and the emission monochromator when required. The signal from PMT was amplified with lock-in amplifier and sent to an analog input of the National Instruments data acquisition card AT-MIO-16XE-50 in computer. The instrument driver for the automated data acquisition

Reproduced with permission of the copyright owner. Further reproduction prohibited without permission.

was written by the author using graphical programming language Labview (see Appendix 2). To obtain the true emission spectrum from the data, it is nesessary to correct for system response. The system response is calibrated against a tungsten-filament quartz-iodine lamp EPI – 1363 from Eppley whose spectral characteristics have been established by the National Bureau of Standards.

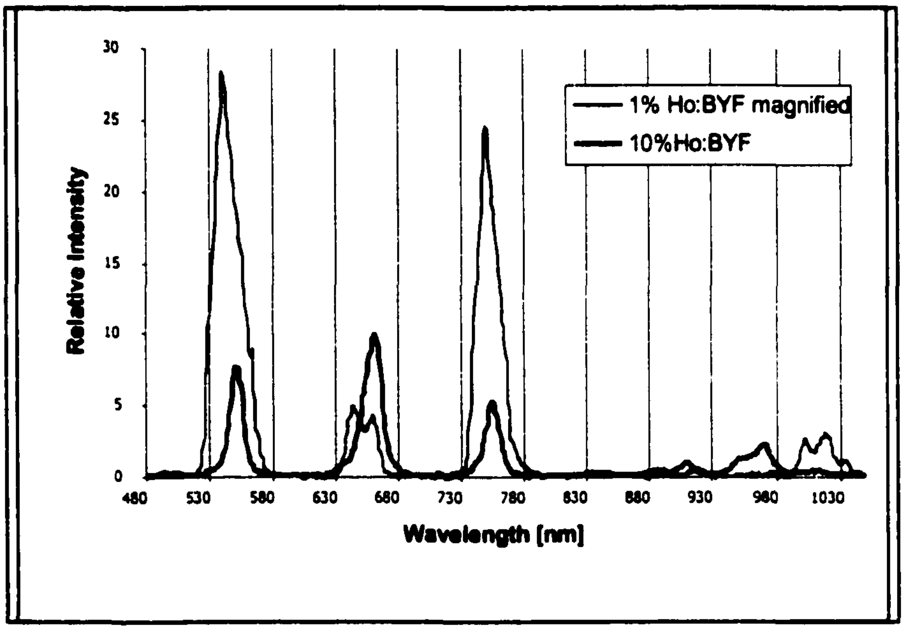

Figure 11. Emission spectrum of Ho:BYF (random polarization).

With the pumping at ~ 455 nm from $^5I_8$ to $^5G_6$ level in low concentration Ho:BYF samples, the excitation relaxes to $^5S_2$ level. Three intense fluorescence lines originate from $^5S_2$ level (Fig. 11): emission line at 546 nm corresponds to transition $^5S_2 \rightarrow {}^5I_8$, 750 nm ($^5S_2 \rightarrow {}^5I_7$), 1020 nm ($^5S_2 \rightarrow {}^5I_6$). Lifetime measurements provided additional proof that all three lines are emitted from $^5S_2$ level: fluorescence decay times for all of them were the same. These emission lines are significantly reduced in the 10% sample, which

Reproduced with permission of the copyright owner. Further reproduction prohibited without permission.

could be attributed to a multiphonon relaxation from the $^5G_6$ to the $^5F_3$ manifold and cross relaxation process from the $^5F_3$ to the $^5F_5$ manifold largely bypassing the $^5S_2$ level. The strong emission lines at 660 nm (due to the $^5F_5$ - $^5I_8$ decay) and 981 nm ($^5F_5$ - $^5I_7$) in high concentration samples are evidences of strong cross relaxation process $^5F_3$ - $^5F_5$ and $^5I_8$ - $^5I_7$.

A similar trend is shown by the emission spectra of Ho:YLF. With the same pumping at ~ 455 nm from $^5I_8$ to $^5G_6$ level in 10% Ho:YLF sample, the excitation transfers, first, from $^5G_6$ to $^5F_3$ level, due to multiphonon relaxation, and from $^5F_3$ level it cross relaxes to $^5F_5$. Two intense lines of emission originate from $^5F_5$ manifold (Figure 12): 659 nm corresponds to transition $^5F_5 \rightarrow {}^5I_8$, 981 nm corresponds to transition $^5F_5 \rightarrow {}^5I_7$. Also, in this case, lifetime measurements provided additional proof that both of these lines are emitted from $^5F_5$ level: fluorescence decay times for both of them were the same.

The trend continues for the 20% Ho:YLF sample (Figure 13), where a marked increase in the relative intensity of emission lines from $^5F_5$ level is seen over emission from the $^5S_2$ level, indicating the further increase in the contribution from cross relaxation processes to the $^5F_5$ level.

The emission at ~ 750 nm corresponds to the transition $^5S_2 \rightarrow {}^5F_7$ (Figure 14 and 15). Although the transition $^5I_4 \rightarrow {}^5I_8$ is also a quite good match to ~750 nm, its contribution, if any, is negligible. The proof of this statement comes from the excitation spectra of Ho^{3+}-doped samples at ~ 752 nm emission wavelength. At ~ 660 nm pump,

Reproduced with permission of the copyright owner. Further reproduction prohibited without permission.

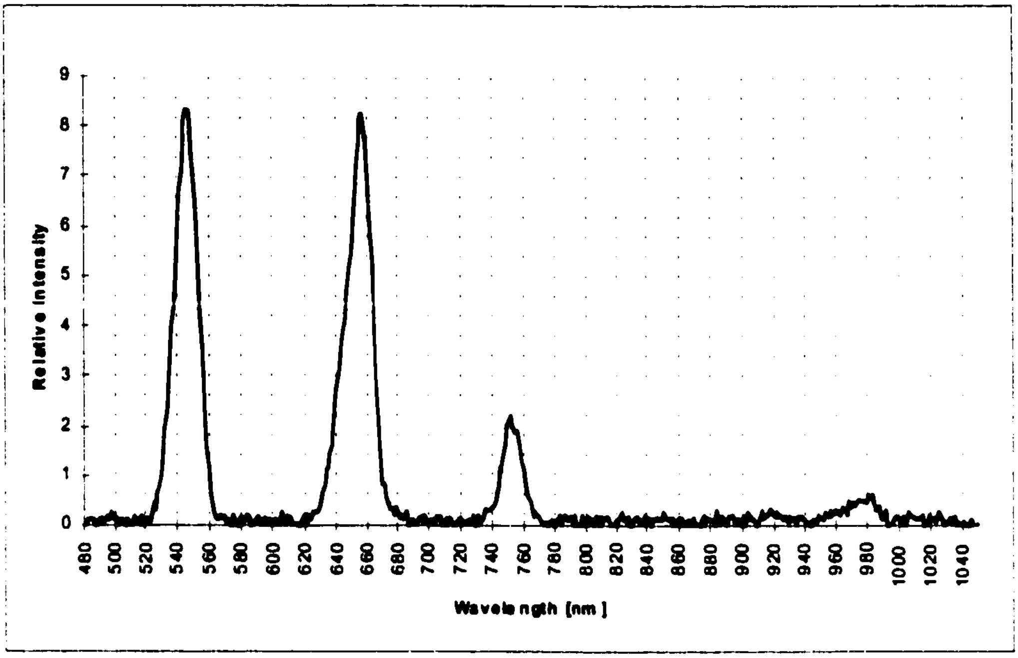

Figure 12. Emission spectrum of 10% Ho:YLF (random polarization).

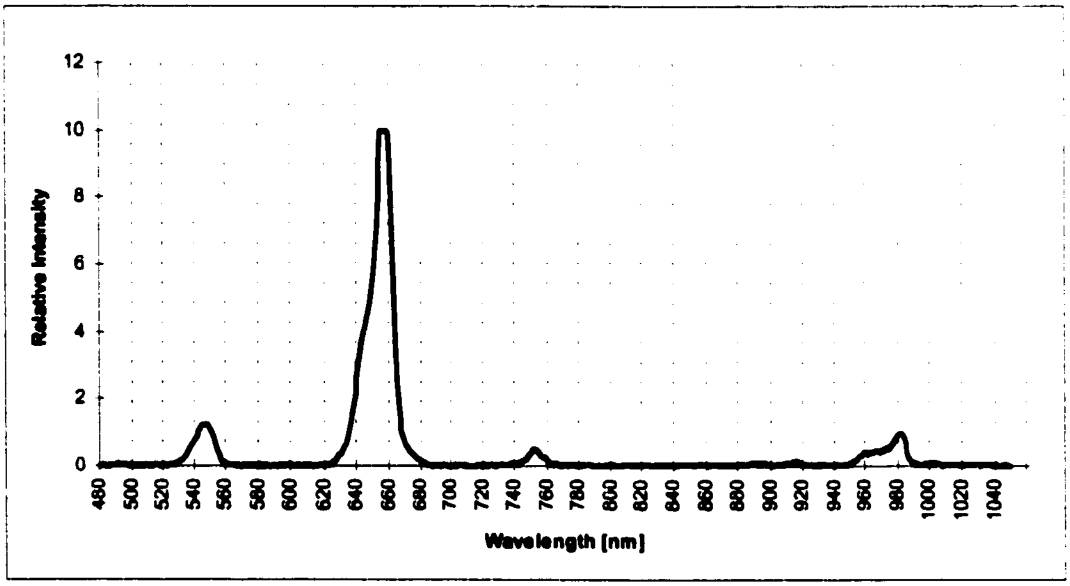

Figure 13. Emission spectrum of 20% Ho:YLF (random polarization).

Reproduced with permission of the copyright owner. Further reproduction prohibited without permission.

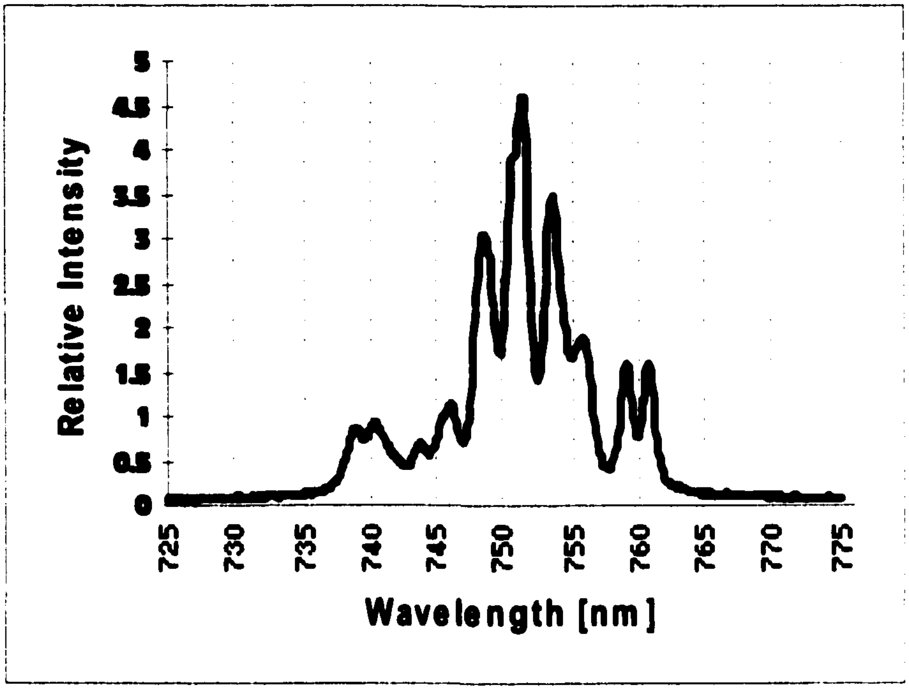

Figure 14. Emission spectrum of 1% Ho:BYF (random polarization).

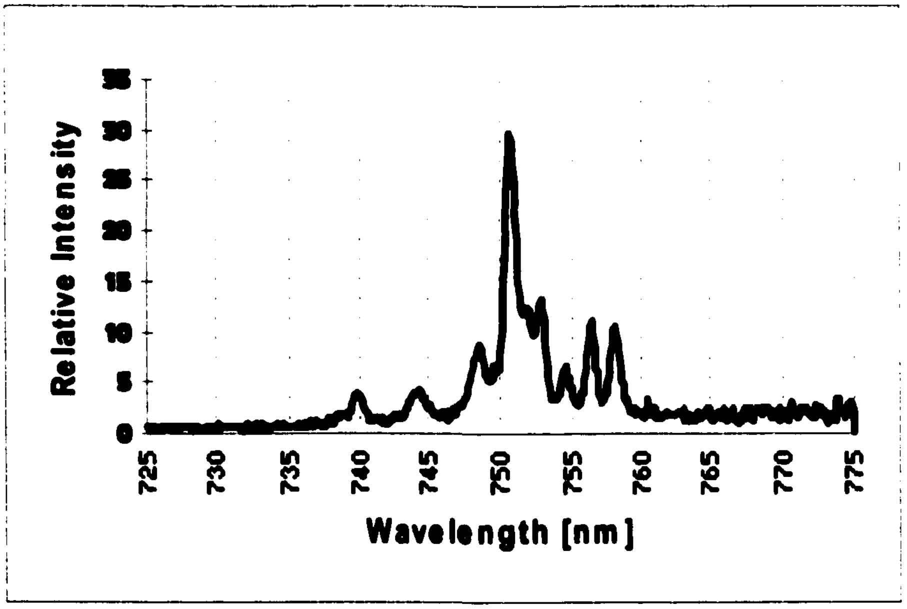

Figure 15. Emission spectrum of 1% Ho:YLF (random polarization).

Reproduced with permission of the copyright owner. Further reproduction prohibited without permission.

which corresponds to excitation from $^5I_8$ to $^5F_5$ level, there is no peak in 750 nm emission (that could be identified as relaxation from $^5F_5$ to $^5I_4$ and emission $^5I_4 \rightarrow {}^5I_8$) (Figures 16 and 17).

Another observation from the emission spectra of Ho:BYF is the following: the ratio of the relative intensities of the emission lines at 660 nm ($^5F_5$ to $^5I_8$) and at 915 nm ($^5I_5$ to $^5I_8$) remains the same for both low (1%) and high (10%) concentrations of Ho:BYF. This suggests that in the feeding of $^5I_5$ level from $^5F_5$ manifold there are no concentration dependent nonlinear processes such as cross relaxation or upconversion.

Additional clues to the energy transfer processes in YLF are provided by the excitation spectra. For example, Figure 18 shows the relative contributions to the emission in 10% Ho:YLF from $^5F_5$ and $^5I_5$ (represented by respective transitions at 981 nm and 915 nm) following absorption to several different levels including $^5G_6$ ($^5F_3$) (450-490 nm), $^5S_2$ ($^5F_4$) (540 nm) and $^5F_5$ (640 nm). This figure shows that emission from $^5F_5$ level, corresponding to 981 nm, is triggered primarily by the absorption to $^5G_6$ ($^5F_3$) and $^5F_5$ and, to a lesser extend, to $^5S_2$. However, the role of the $^5F_5$ level in producing emission from $^5I_5$ (at 915 nm) is diminished compared to that of $^5S_2$. As concentration increases to 20%, the ratio of contributions from higher manifolds mentioned above to $^5I_5$ emission at 915 nm remains basically the same as in 10% (Figure 19). The excitation spectrum for the 981 nm emission from $^5F_5$ level in Ho:YLF, however, exhibits strong concentration dependence. In 10% Ho:YLF the strongest contribution to 981 nm emission is observed due to direct absorption from ground state to $^5F_5$ level at 650 nm. Somewhat less is the contribution due to absorption to $^5G_6$ ($^5F_3$) manifolds, and the smallest contribution is from the $^5S_2$ level. In 20% sample, the contribution to the 981 nm

Reproduced with permission of the copyright owner. Further reproduction prohibited without permission.

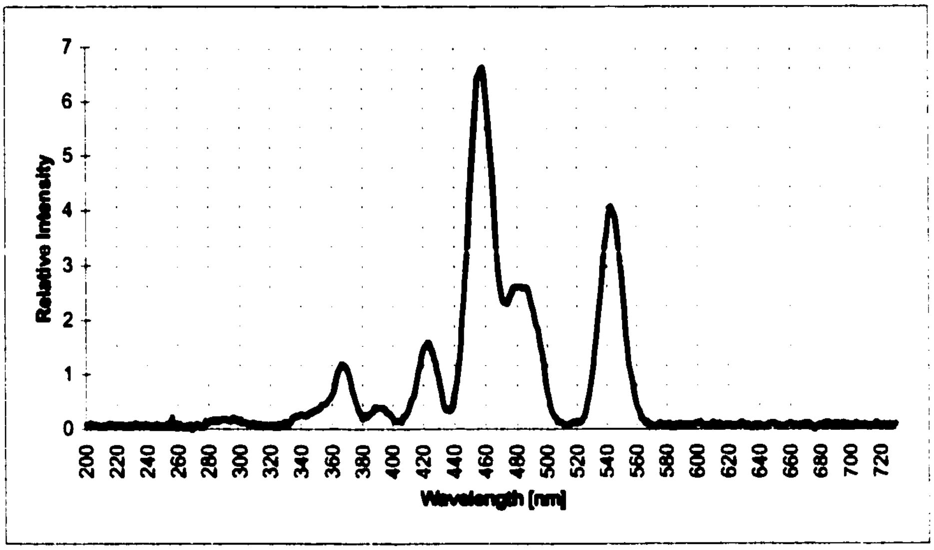

Figure 16. Excitation spectrum of 1% Ho:BYF (random polarization) at emission wavelength 752 nm.

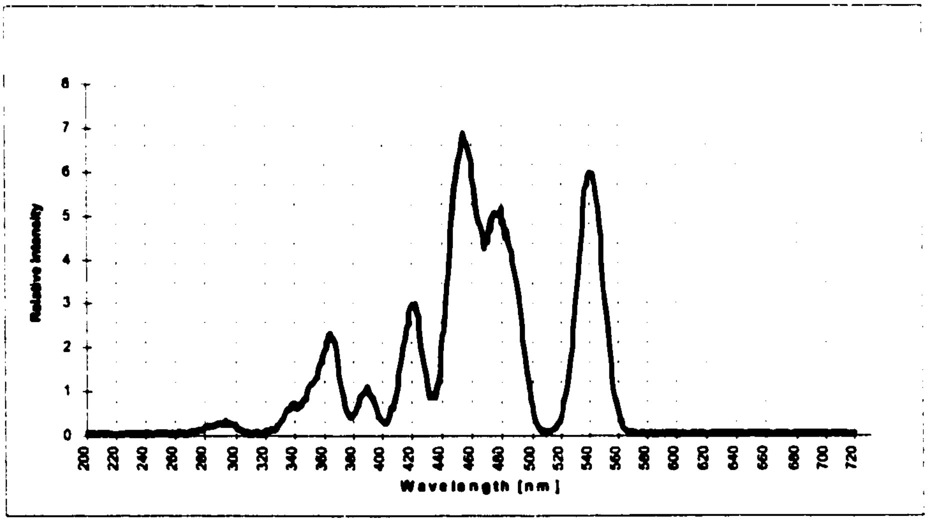

Figure 17. Excitation spectrum of 20% Ho:YLF (random polarization) at emission wavelength 750 nm.

Reproduced with permission of the copyright owner. Further reproduction prohibited without permission.

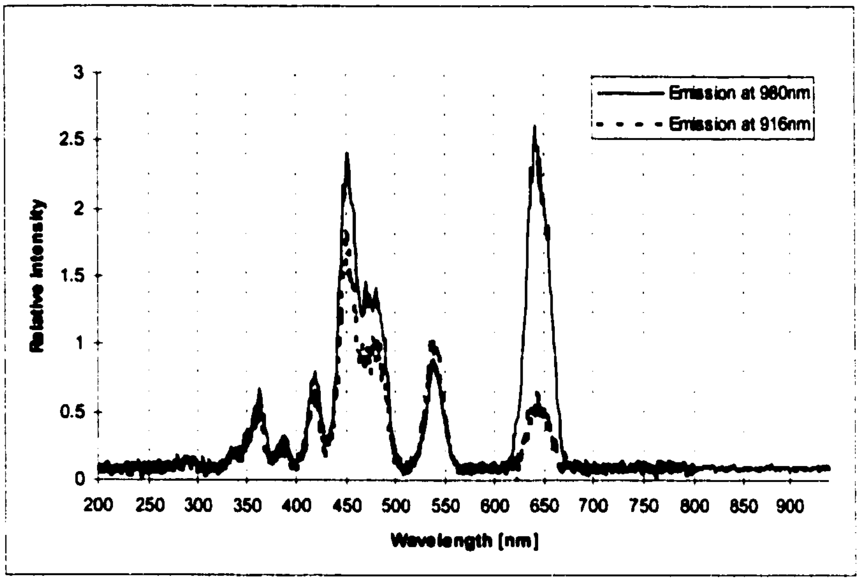

Figure 18. Excitation spectrum of 10% Ho:YLF (random polarization) at two different emission wavelengths 916 nm and 980 nm.

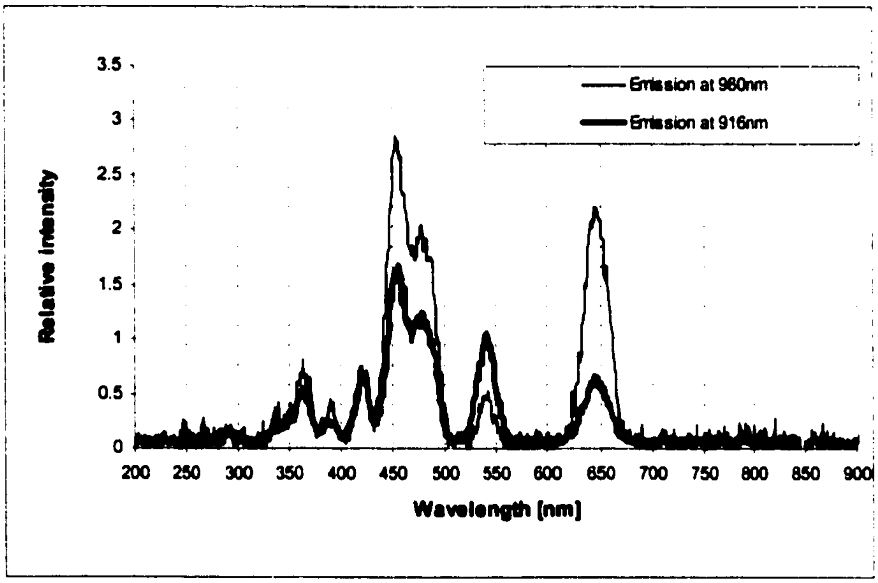

Figure 19. Excitation spectrum of 20% Ho:YLF (random polarization) at two different emission wavelengths 916 nm and 980 nm.

Reproduced with permission of the copyright owner. Further reproduction prohibited without permission.

emission due to absorption to $^5G_6$ ($^5F_3$) manifolds exceeds the direct absorption into $^5F_5$ from which the 981 nm line originates. The absorption to $^5S_2$ level in the 20% sample contributes even less to 981 nm emission than in 10% sample.

These measurements indicate that, in Ho:YLF, a strong cross relaxation process exist between $^5F_3$ and $^5F_5$ multiplets, with the latter exhibiting weaker transition to $^5I_5$. This cross relaxation process bypasses the $^5S_2$ level, with the rate increasing with Ho^{3+} concentration in such a manner that at 20% sample the rate of feeding the population from the $^5F_3$ to $^5F_5$ due to cross relaxation is higher than the rate of decay of the $^5F_5$ level. The $^5S_2$ level contributes to $^5I_5$ through another cross relaxation process between $^5S_2$ and $^5I_4$ followed by multiphonon relaxation to $^5I_5$. Alternatively, the radiative transition at 1.4 µm from $^5S_2$ can also populate the $^5I_5$ level being most effective at lower concentrations, where cross relaxation is less significant.

Another set of emission spectra for the detection of the infrared emission lines, particularly the weak emission from $^5I_5$ manifold in 890 - 915 nm wavelength range, was performed with argon laser used as an excitation source. The experimental set-up is shown in Figure 20. The laser beam was focused on the sample. The fluorescence from the sample was focused with a lens onto the entrance slit of the 0.3m McPherson monochromator. Emitted radiation was filtered by a monochromator that was feeding the signal to a detector photomultiplier. The dry-ice cooled PMT was used in the measurements of emission at 890-915 nm. A polarizer and a filter were placed between the sample and the monochromator when required. In some experiments, the pump beam was chopped instead of fluorescence to reduce the heat load on the crystal. In such cases the chopping rate was always adjusted so that the fluorescence lifetimes of the multiplets

Reproduced with permission of the copyright owner. Further reproduction prohibited without permission.

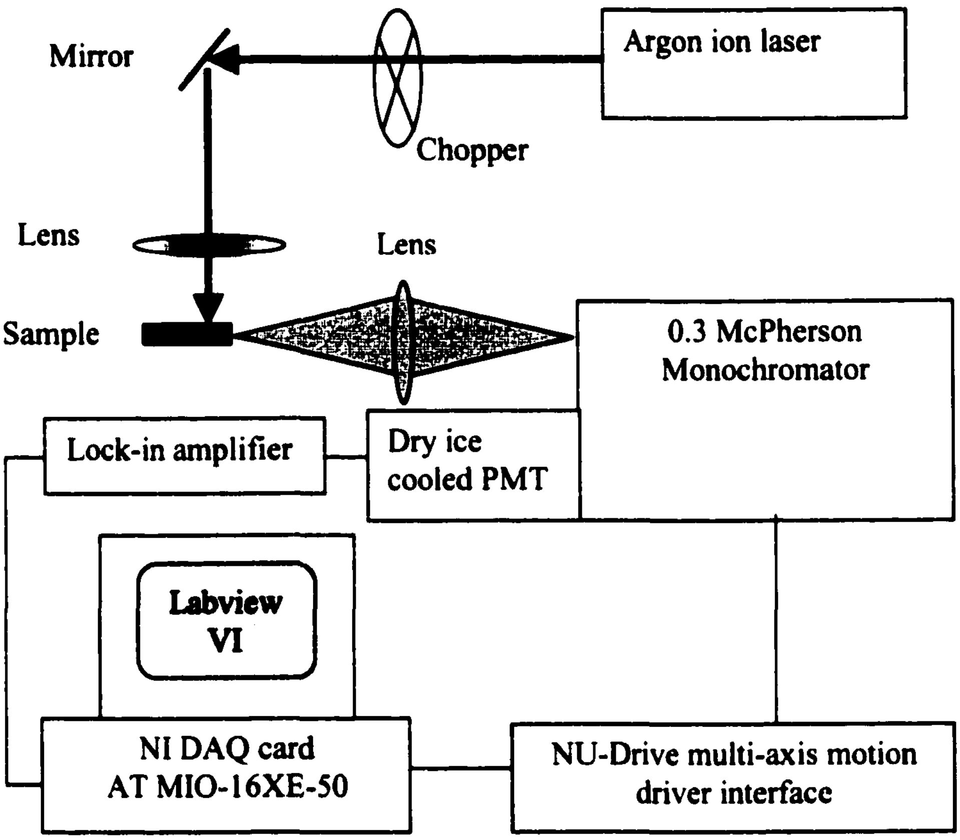

Figure 20. Experimental set-up for fluorescence measurement.

did not interfere with the measurements. The signal from the PMT was amplified with a lock-in amplifier using the reference signal from the chopper, and was sent to analog input of the National Instruments data acquisition card AT-MIO-16XE-50 in computer. Graphical programming language Labview was used for the programming the instrument driver for automated control of 0.3 m McPherson spectrometer with simultaneous real time data acquisition. (see Appendix 1).

Reproduced with permission of the copyright owner. Further reproduction prohibited without permission.

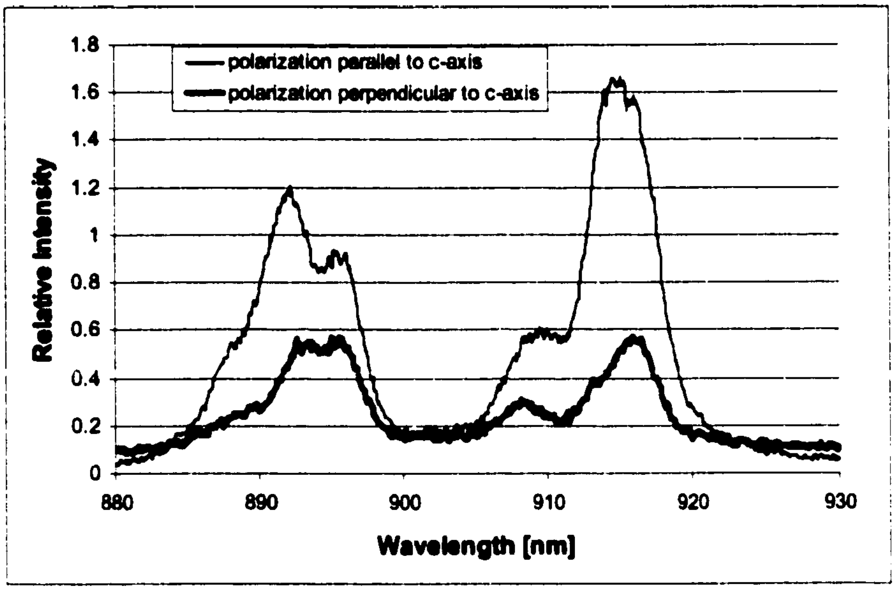

Figure 21. Polarized fluorescence spectrum of 10% Ho:YLF representing the emission from $^5I_5$ manifold to ground state.

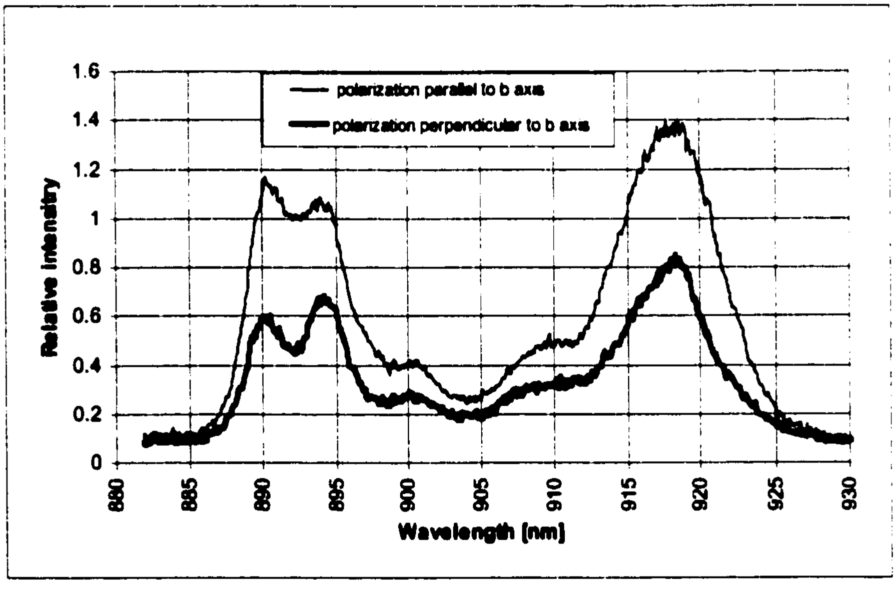

Figure 22. Polarized fluorescence spectrum of 10% Ho:BYF representing the emission from $^5I_5$ manifold to ground state.

Reproduced with permission of the copyright owner. Further reproduction prohibited without permission.

The fluorescence spectra of Ho:BYF and Ho:YLF samples in 900 nm range, representing the emission from $^5I_5$ manifold to ground state are shown in Figure 21 and 22, respectively.

The polarized spectra in 10% Ho:BYF sample with beam propagation along the a-axis show stronger emission for the polarization of light parallel to b-axis than in [001] direction (perpendicular to b-axis). In 20% sample, the beam propagation was along the b-axis, and the emission spectra for polarization parallel to two extinction directions *x*- and *z*- were not significantly different.

We performed calculations of the emission cross section for $^5I_5$ - $^5I_8$ transition with the reciprocity method (RM) [34, 35] which is based on deriving the emission cross section from the absorption spectra, the dopant concentration, and the detailed knowledge of the energy levels of the system. The partial listing of energy levels of Ho^{3+} in BYF can be found in the reference [27], and the analysis of the optical spectrum of Ho^{3+} in YLF is presented in the paper [36].

3.2.1. Reciprocity method of emission cross section determination

The cross sections of the absorption and emission processes arising from the levels of the upper and lower states, as shown schematically in Fig. 23, and characterized by the energies E_i, E_j and the degeneracies d_i, d_j, can be described by the sum of the individual cross sections σ_{ij} between the levels [34,35]:

Reproduced with permission of the copyright owner. Further reproduction prohibited without permission.

$$\sigma_{em}(\nu) = \sum_{ij} \sigma_{ji} d_j d_i \left[\frac{\exp(-E_j / kT)}{Z_u} \right]$$
$$\sigma_{abs}(\nu) = \sum_{ij} \sigma_{ij} d_j d_i \left[\frac{\exp(-E_i / kT)}{Z_l} \right] \qquad (3.1)$$

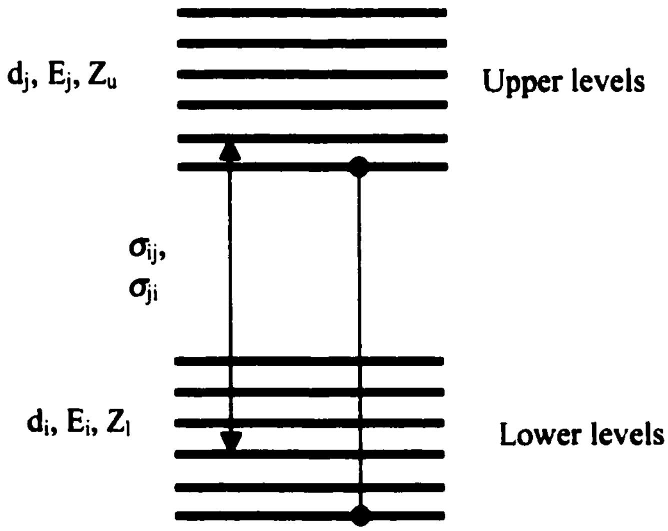

Figure 23. Representation of the crystal field levels of the ground and excited states of a rare-earth doped ion: d denote the degeneracies, E are energies, Z the partition functions of lower (i) and upper (j) electronic states.

where the line shape information is contained in $\sigma(\nu)$. The energies and partition functions (Z_u and Z_l) are measured from the lowest crystal field level of each multiplet. The factor in square brackets represents the fractional thermal occupation of the i_{th} or j_{th} level of the upper (u) or lower (l) states. The partition function is defined as

$$Z = \sum_k d_k \exp(-E_k / kT) \qquad (3.2)$$

Reproduced with permission of the copyright owner. Further reproduction prohibited without permission.

Any particular energy separation between the upper and lower levels can be selected as

$$E_j - E_i = h\nu - E_{ZL} \tag{3.3}$$

where E_{ZL} is the energy separation between the lowest crystal field components of the upper and the lower states (zero-line).

Eqs. (3.1)-(3.3), with account of the reciprocity condition $\sigma_{ij} = \sigma_{ji}$, lead to the following relationship

$$\sigma_{em}(\nu) = \sigma_{abs}(\nu)\frac{Z_l}{Z_u}\exp[(E_{ZL} - h\nu)/kT] \tag{3.4}$$

The expression (3.4) shows that the emission spectrum can be obtained from the absorption cross-section line shape. The additional required information includes the ratio of the partition functions of the lower and upper states Z_l/Z_u and the energy of the zero-line at E_{ZL}. In the high temperature limit, Z_l/Z_u is reduced to the degeneracy weighting of the two states. The low temperature absorption and emission spectra generally provide an adequate value for Z_l/Z_u, which is a number and is independent on spectral energies. The accuracy of the exponential factor is, however, strongly impacted by the precision of determination of the zero-line energy E_{ZL} [37].

According to emission cross section profile derived with reciprocity method (Figure 24) the strongest peak of the $^5I_5$ - $^5I_8$ emission in 10% Ho:BYF is observed at 915 nm for polarization of the light parallel to b-axis of the crystal with the value of cross

Reproduced with permission of the copyright owner. Further reproduction prohibited without permission.

section $\sigma = 1.35 \cdot 10^{-21}$ cm^2. For polarization of the light perpendicular to b-axis the cross section is $\sigma = 9.9 \cdot 10^{-22}$ cm^2.

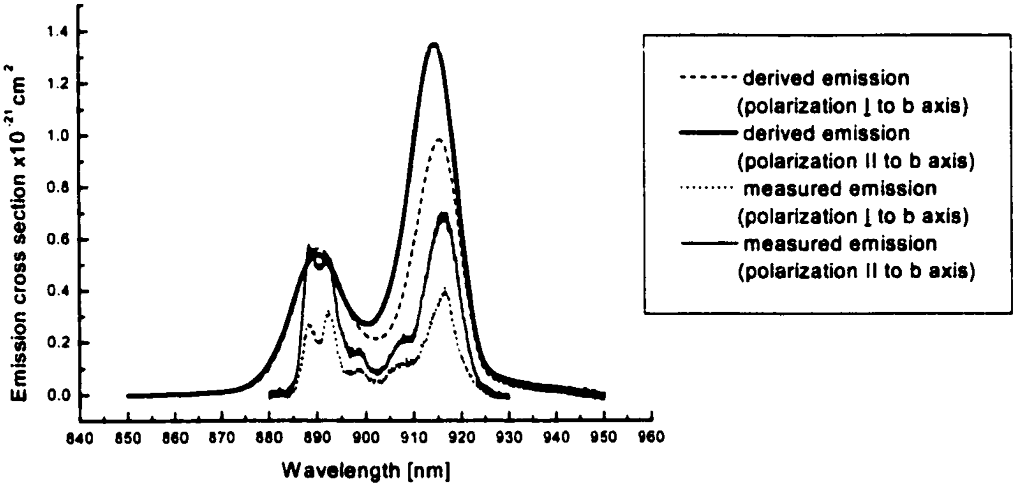

Figure 24. Derived and measured emission cross section of $^5I_5$ - $^5I_8$ fluorescence in 10% Ho:BYF.

The derived emission cross sections for [010] sample is: $\sigma = 7.9 \cdot 10^{-22}$ cm^2 in *x*-axis direction, and $\sigma = 7.3 \cdot 10^{-22}$ cm^2 in z-axis direction (Figure 25). There is some discrepancy, however, with the measured emission spectra, which can be mainly attributed to reabsorption of the emission. The excitation beam was positioned as close as possible to the surface of the crystal to minimize the reabsorption, however, the strong overlap of absorption and emission spectra led to significant attenuation of emission.

Reproduced with permission of the copyright owner. Further reproduction prohibited without permission.

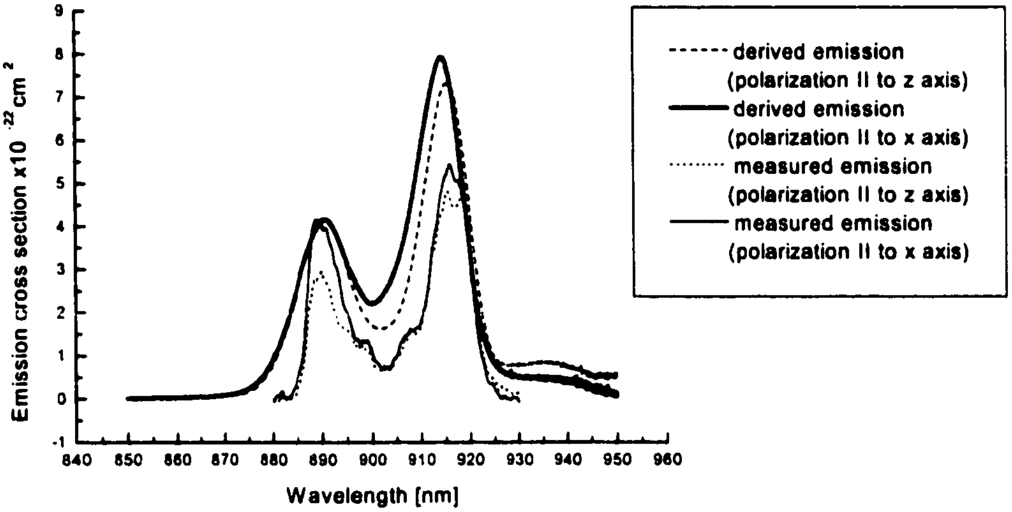

Figure 25. Derived and measured emission cross section of $^5I_5$ - $^5I_8$ fluorescence in 20% Ho:BYF.

3.3. Lifetime measurements

Lifetime measurements were performed primarily for the study of cross relaxation effects in Ho:BYF and Ho:YLF, in particular for the cross relaxation from $^5S_2$ level, which results in $^5S_2$ - $^5I_4$ and $^5I_8$ to $^5I_7$ transitions. The cross relaxation rate can be determined by observing the change in lifetime of the $^5S_2$ manifold with changing Ho^{3+} concentration. For the lifetime measurements we directly pumped the $^5S_2$ manifold with a Q-switched frequency doubled Nd:YAG laser at 532 nm (pulse duration 20 ns).

The time dependent fluorescence was measured at ~540 nm (transition from the bottom of $^5S_2$ manifold to ground level) and at ~752 nm (transition from $^5S_2$ to $^5I_7$). The lifetimes of fluorescence decay were the same at both wavelengths. The typical setup used for lifetime measurements is described, for example, in [38]. The pulsed laser radiation was focused into the sample. Fluorescence from the sample was focused with a

Reproduced with permission of the copyright owner. Further reproduction prohibited without permission.

lens onto the entrance slit of McPherson 0.3m monochromator. In addition to the monochromator, a band pass filter was used to provide additional scattered light rejection. Photomultiplier tube was used for the detection of the fluorescence decay. Time-dependent fluorescence data were acquired with Tektronix TDS 380 digital real time oscilloscope with 400MHz analog bandwidth. Data were fitted using such plotting routines as MicroCal Origin or Microsoft Excel (Figure 26, 27 and 28). Lifetimes were interpreted as the 1/e time of the linear portion of the natural logarithm of the time-dependent fluorescence intensity.

Eight different samples were used for the measurements: 1%, 2%, 10%, 20% Ho:BYF and 1%, 2%, 10%, 20% Ho:YLF. The measured lifetimes of the fluorescence decay from $^5S_2$ level are presented in Table 1.

The decrease of the measured lifetimes clearly showed the significant increase of the cross-relaxation rate with the increase of Ho^{3+} concentration.

Table 1. The lifetimes of the fluorescence decay from $^5S_2$ level

Concentration of Ho^{3+} ions	Ho:BYF	Ho:YLF
1%	284.5 μs	97 μs
2%	252 μs	70 μs
10%	15.5 μs	5.2 μs
20%	3.7 μs	2 μs

Reproduced with permission of the copyright owner. Further reproduction prohibited without permission.

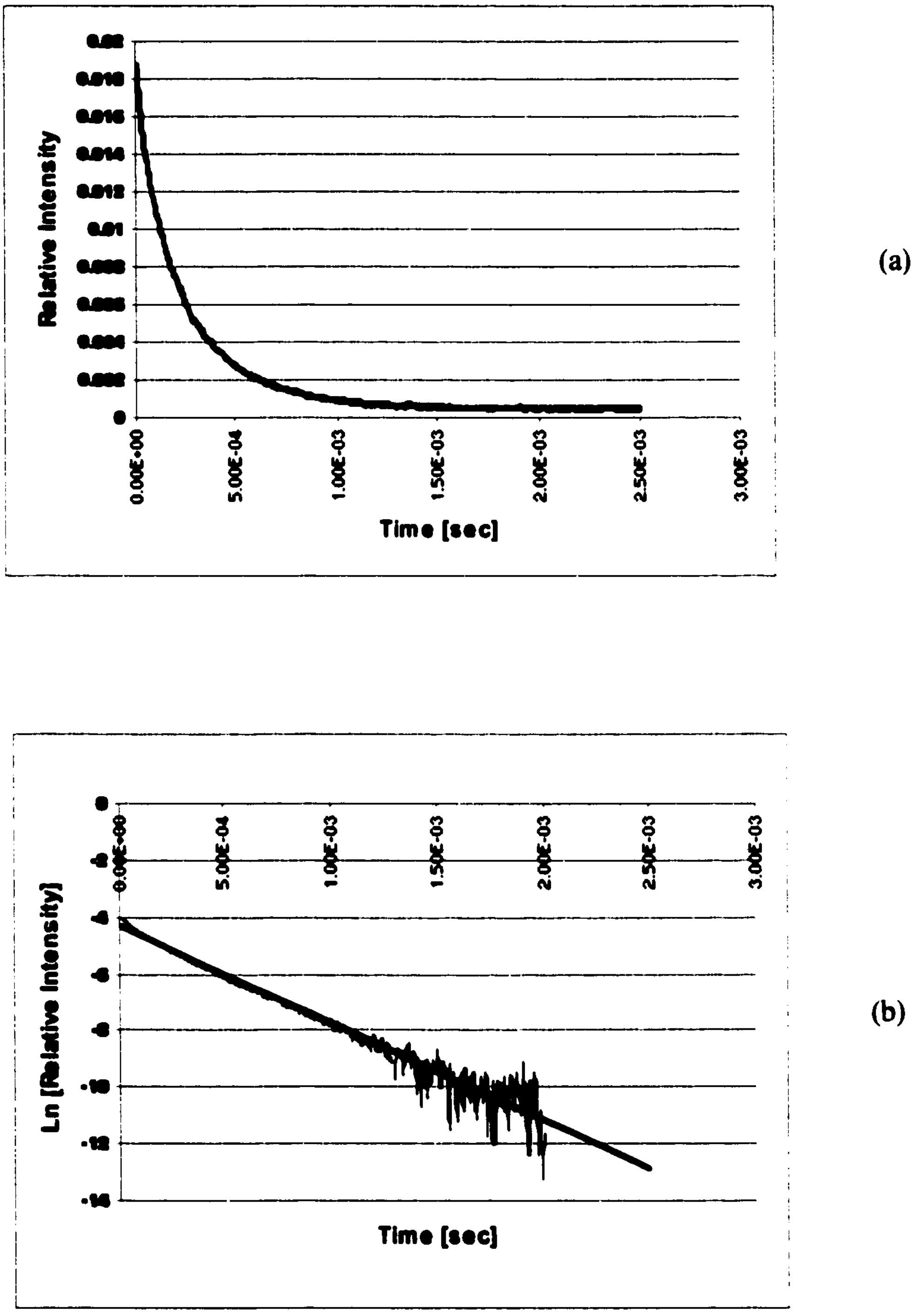

Figure 26. Fluorescence decay from $^5S_2$ level in 1% Ho:BYF with the lifetime τ=284.5 μsec: (a) fluorescence intensity vs. time; (b) natural logarithm of fluorescence intensity vs. time.

Reproduced with permission of the copyright owner. Further reproduction prohibited without permission.

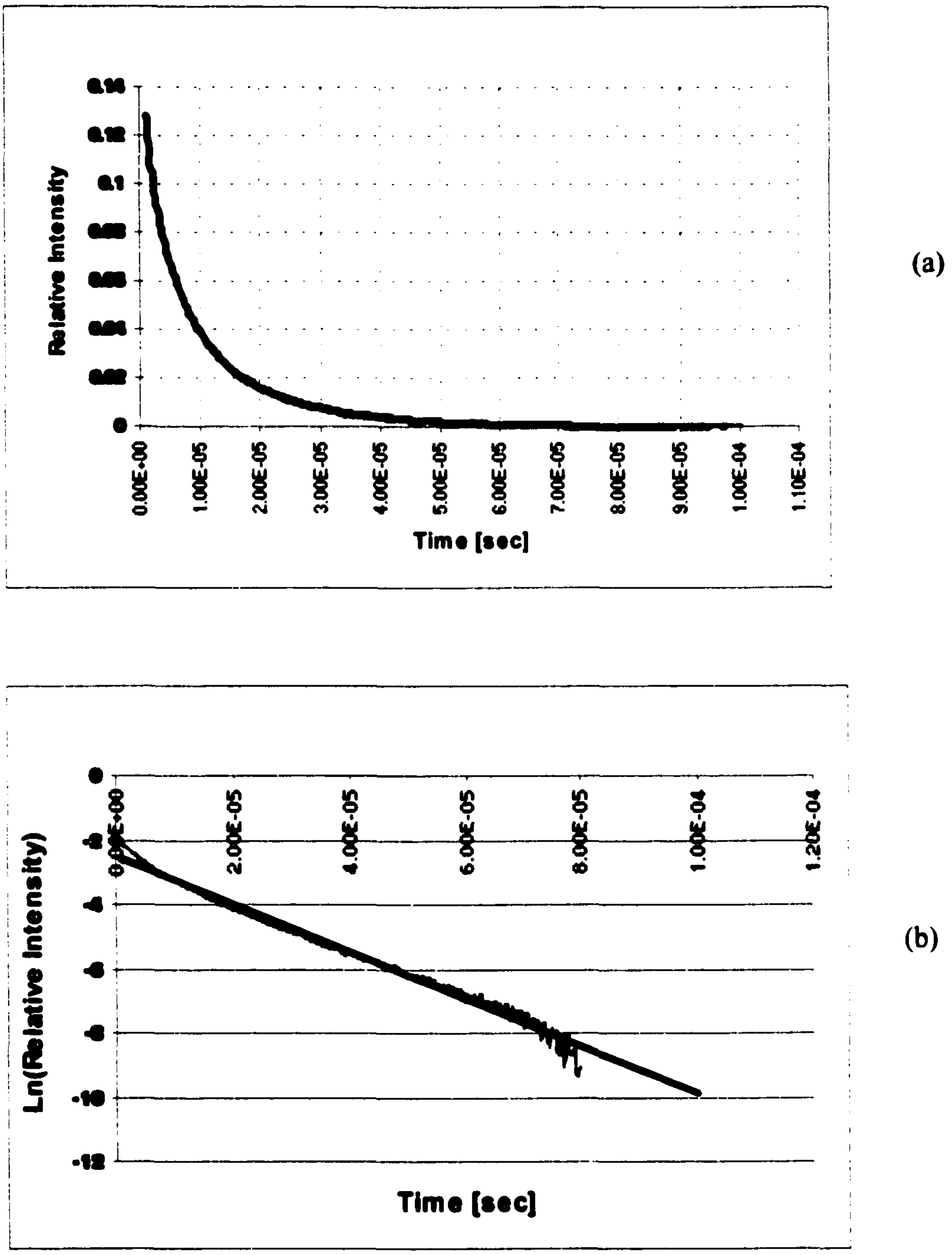

Figure 27. Fluorescence decay from $^5S_2$ level in 10% Ho:BYF with the lifetime $\tau = 15.5$ μs: a) fluorescence intensity vs. time; b) natural logarithm of fluorescence intensity vs. time.

Reproduced with permission of the copyright owner. Further reproduction prohibited without permission.

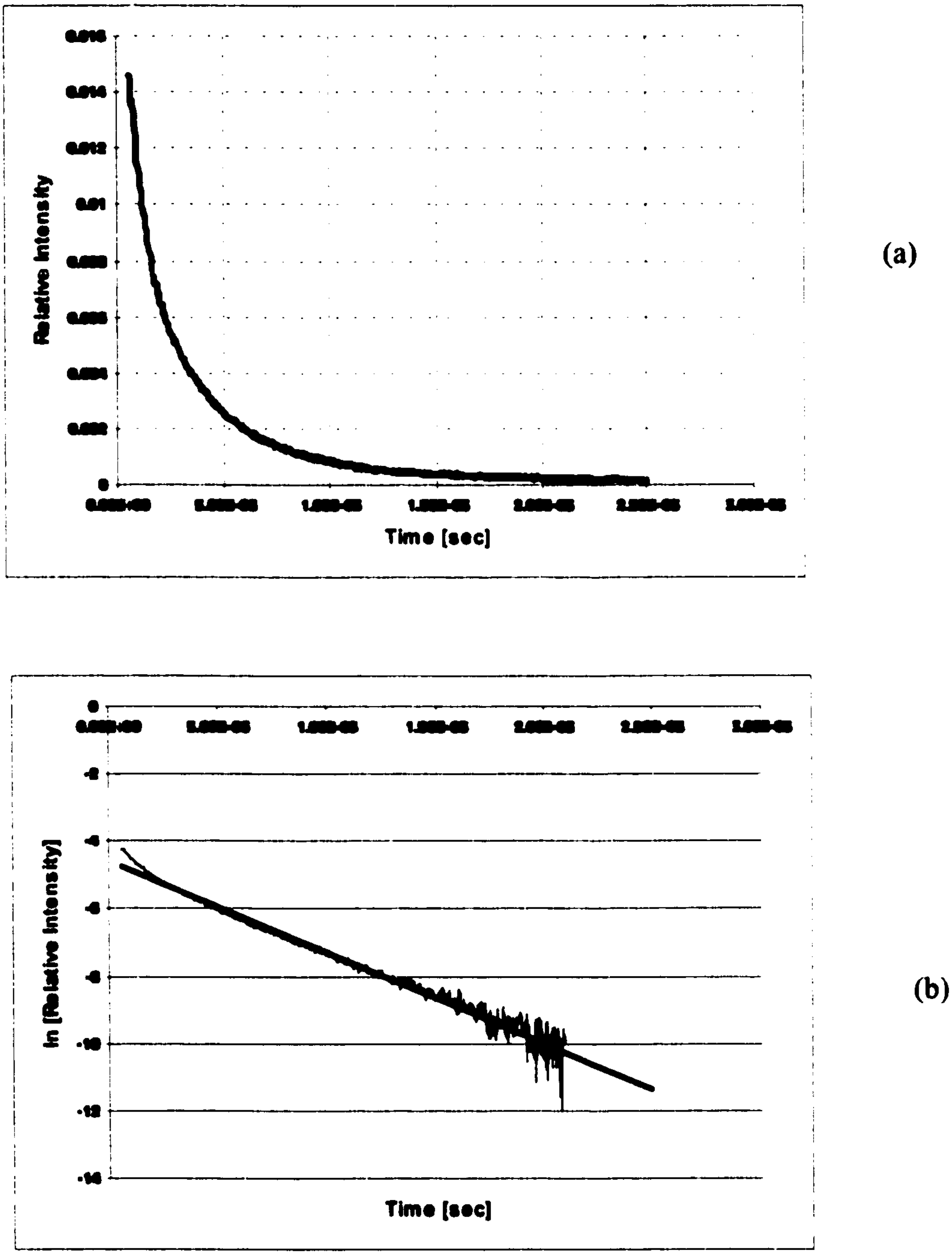

Figure 28. Fluorescence decay from $^5S_2$ level in 20% Ho:BYF with the lifetime $\tau = 3.7$ μs: (a) fluorescence intensity vs. time; (b) natural logarithm of fluorescence intensity vs.time.

Reproduced with permission of the copyright owner. Further reproduction prohibited without permission.

CHAPTER 4. STUDY AND CHOICE OF THREE DIFFERENT PUMPING SCHEMES OF THE 3.9 μM LASER

4.1. Linear down-conversion lasers

Spectral diversity in laser materials may be greatly extended through laser pumping that "shifts" the laser energy downward. As opposed to non-linear parametric oscillators, this is a linear process. Resonant pumping of rare-earth-doped solid state lasers using appropriate pump lasers (linear down-conversion) is a viable way of obtaining high-efficiency, multiple-wavelength, high average power sources. In comparison to typical flashlamp pumped solid state laser, linear down-converters offer several operating advantages: 1) resonant pumping of the upper laser level permits high conversion efficiency; 2) radiative upper and lower laser levels result in very low heat loading permitting high average power operation; 3) resonant pumping permits access to states difficult or impossible to pump with incoherent sources (long lifetimes or broad-band absorption are not required), and 4) brightness enhancement of the source is possible.

An important case of linear down-conversion lasers is reported by Knights et al. [17] on frequency conversion of doubled Nd:YAG operating at 532nm in both Ho:YLF

Reproduced with permission of the copyright owner. Further reproduction prohibited without permission.

and Er:YLF. By resonantly pumping the laser transitions in the solid medium, conversion efficiencies up to 25% were demonstrated at pump limited repetition rates of up to 40Hz.

Apart from the customary transition in holmium at 2.06 μm from the $^5I_7$ level to the ground state, other higher level transitions can be very difficult to lase using standard excitation techniques such as flashlamps, which, being broad-band, require upper laser levels with long fluorescent lifetimes and small non-radiative decay rate. Yet, some of the most interesting laser transitions, such as 3.9 μm one between $^5I_5$ and $^5I_6$ manifolds, originate on levels characterized by lifetimes that are short compared with those of the lower levels. This effectively turns the transition into a three level laser system, resulting in very high thresholds and self-terminating laser action. Other difficulties associated with long wavelength transitions, as we mentioned before, include high multiphonon non-radiative decay rates between closely spaced levels and smaller stimulated emission cross-sections.

As it was stated before, the main purpose and motivation for this work was an investigation of the feasibility of achieving 3.9 μm laser emission in holmium doped fluoride crystals Ho:BYF and Ho:YLF based on our spectroscopic measurements and theoretical calculations.

Energy level diagram for $Ho^{3+}$is depicted in (Figure 29). Energy level lifetimes for Ho^{3+} in two different hosts are presented in Table 2. The 3.9 μm transition is between the $^5I_5$ and $^5I_6$ manifolds. The short lifetime of the upper laser level $^5I_5$ compared to that of the lower level $^5I_6$, combined with the rapid nonradiative decay rates between closely spaced levels produce conditions, which are, in general, unfavorable for lasing.

Reproduced with permission of the copyright owner. Further reproduction prohibited without permission.

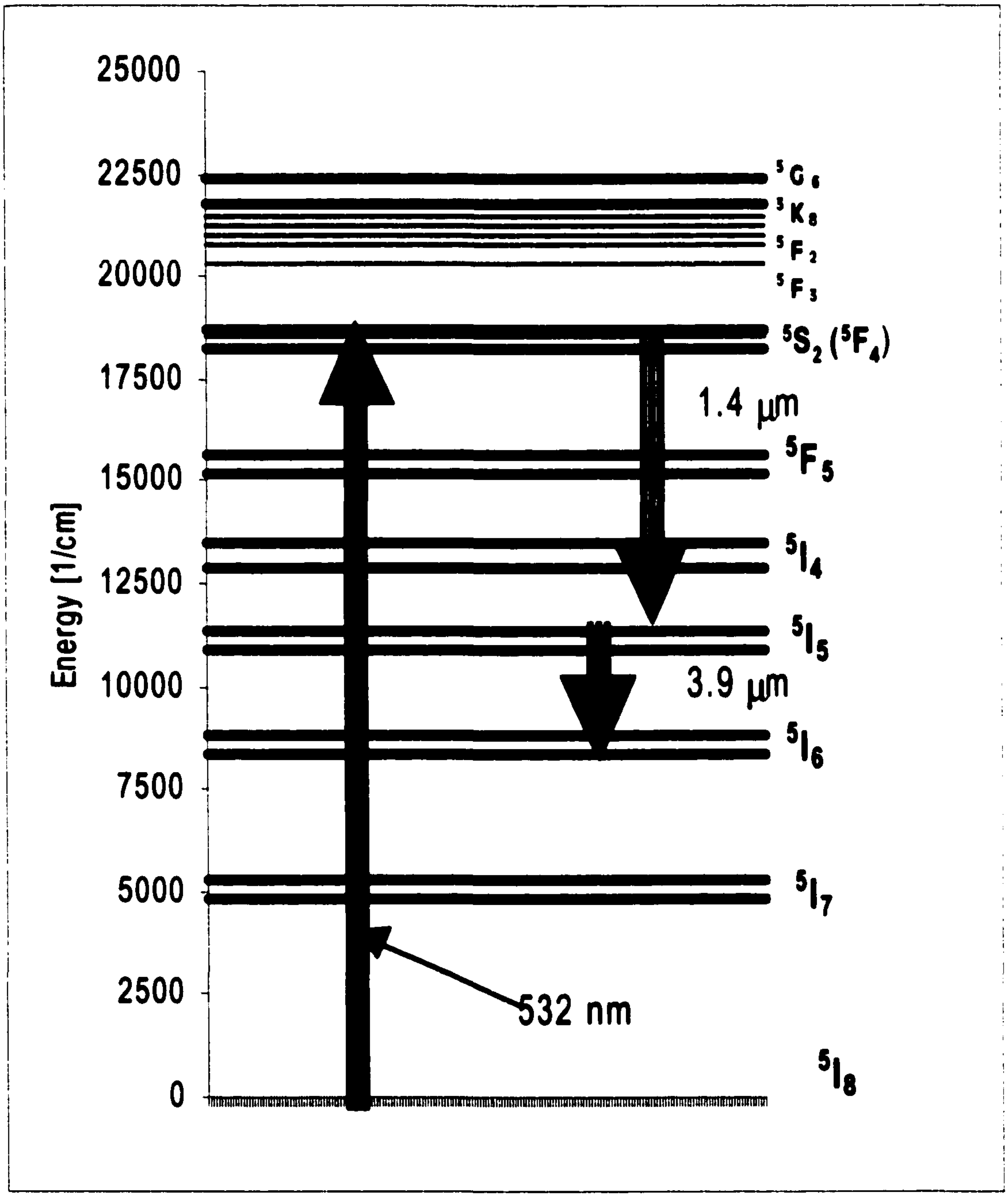

Figure 29. Pulsed resonant pumping scheme of Ho^{3+} doped fluorides at 532 nm.

Reproduced with permission of the copyright owner. Further reproduction prohibited without permission.

Table 2. Summary of the Ho^{3+} energy level lifetimes in YLF and BYF

τ	Ho:YLF	Ho:BYF
$^5I_7$	14 ms [38]	17 ms [38]
$^5I_6$	2050 μs [39]	5000 μs [40]
$^5I_5$	20 μs [38]	50 μs [38]
$^5I_4$	<10 μs	<10 μs
$^5F_5$	30 μs [39]	40 μs [38]
$^5S_2$	100 μs	280 μs

One way to force laser action under such unfavorable conditions is to cool the gain material, which allows its operation as a four-level laser. Moreover, at lower temperatures the non-radiative transition rates decrease thereby increasing upper level life-times and reducing reabsorption losses resulting in lower lasing thresholds.

Another option, which does not require cooling, is through use of linear down-conversion with short pulse resonant pumping. With direct excitation to the upper laser level, a population inversion can be created even from levels where long fluorescence lifetimes are not available thus circumventing the limitation suffered by broadband excitation techniques. Furthermore, in certain cases, advantage can be taken of cascaded processes whereby laser oscillation between intermediate levels is exploited for increasing the rate of transition to the upper level of a lower lying manifold thus achieving inversion on an otherwise unfavorable laser transition. This removes the requirement that the upper laser level have a long fluorescent lifetime and a small

Reproduced with permission of the copyright owner. Further reproduction prohibited without permission.

nonradiative decay rate, since population can be transferred to the desired level through the cascade laser process, with resultant multiwavelength sequential emission.

Three different pumping schemes of 3.9 μm laser using linear down conversion were studied: short pulse resonant pumping at 532 nm, cw cascade resonant pumping at 750 nm, and long pulse resonant direct pumping of the upper level of laser transition at 890 nm.

4.2. Pulsed resonant pumping of Ho:BYF and Ho:YLF at 532 nm

The first laser concept is based on a novel combination of resonant pumping and cascade laser transitions, inspired by experiments conducted by Esterowitz et al [18].

Cascade laser action has been observed in 1% Ho^{3+}-doped YLF using short pulse resonant pumping of the $^5S_2$ manifold by frequency-doubled Nd:glass [18] and a dye [19] lasers. The cascade process involving the $^5S_2$ - $^5I_5$ and $^5I_5$ - $^5I_6$ transitions is shown in Figure 29. By lasing the $^5S_2$ - $^5I_5$ transition at 1.39 μm, the excited state population could be directly transferred to the intermediate level $^5I_5$, which serves as the upper level for a subsequent laser transition. In this manner, both the $^5S_2$ - $^5I_5$, $^5I_5$ - $^5I_6$ (1.392 μm, 3.914 μm) and $^5S_2$ - $^5I_5$, $^5I_5$ - $^5I_7$ (1.392 μm, 1.673 μm) cascade transitions were successfully lased [18]. Operation at these wavelengths has been limited, however, by the need to tune the pump to the absorption peak of the $^5S_2$ manifold, near 535 nm. This wavelength matches up poorly with most readily available lasers, which was one of the factors precluding practical application of such cascade lasers. Our approach for solving this problem was to use a Q-switched, frequency doubled Nd:YAG laser at 532 nm for pumping of Ho:BYF crystal.

Reproduced with permission of the copyright owner. Further reproduction prohibited without permission.

Linear down-converters are of practical interest when pumped by efficient, well developed sources. Frequency doubled Nd:YAG laser systems are a convenient laser pump source because considerable number of high performance (high peak and high average power) systems based on 532 nm are commonly available. Instead of low concentration laser materials described in the references [18,19], however, we used higher concentrations of the active ion to increase pump absorption. At 10% concentration of holmium ions in BYF, we measured an absorption coefficient of 2.42 cm^{-1} at 532 nm for polarization parallel to the **b**-axis (Figure 6), which is adequate for end pumping.

The 532 nm pump excites the Ho^{3+} ions into the $^5F_4$ manifold, which is in thermal equilibrium with the $^5S_2$ manifold. Rapid multiphonon relaxation brings the ions to the lowest sublevel of the $^5S_2$ manifold which serves as the upper laser level for the first transition at 1.39 μm followed by the 3.9 μm transition in the cascade laser sequence $^5S_2$ - $^5I_5$ - $^5I_6$. Several factors affect the efficiency at which absorbed pump energy is converted to 1.39 μm and then to 3.9 μm output in the resonantly pumped oscillator. These are the quantum efficiencies with which the absorbed energy appears in the upper laser level, the storage efficiency of the crystal, the input-output photon-energy decrement, the extraction efficiency, and the output coupling efficiency.

The conversion process is linear and the photon energy decrement is simply the input-to-output photon-energy ratio: 0.38 for the first transition at 1.39 μm.

Since the pump level is in thermal equilibrium with the upper laser level, the quantum efficiency of pump-band to metastable level transition is unity. As the thermal relaxation times between J manifolds in rare-earth ions, which are typically much less

Reproduced with permission of the copyright owner. Further reproduction prohibited without permission.

than 10^{-9} s, are much faster than rates associated with nonradiative decay due to "concentration quenching", the near unity quantum efficiency of 532 nm pump to the upper laser level is expected to be concentration independent.

The storage efficiency is the fraction of energy stored in the upper laser level that remains in that level up to the time the output pulse is generated. For the assessment of the expected efficiency of the cascade laser process in high concentration samples, it was important to measure the changes in the lifetime of the upper energy level $^5S_2$ of the sequence of transitions at 1.39 μm and 3.9 μm. At higher Ho^{3+} concentrations desirable for laser applications (10% to 20%), the resonant cross relaxation (CR) process – simultaneous transitions from $^5S_2$ to $^5I_4$ and from $^5I_8$ to $^5I_7$ - is very efficient. It shortens the lifetime of the $^5S_2$ level through rapid relaxation from $^5S_2$ to $^5I_4$. The cross relaxation rate can be determined by observing the change in lifetime of the $^5S_2$ manifold with changing Ho^{3+} concentration. Using the lifetime measurement apparatus described in Chapter 3, we directly pumped the $^5S_2$ manifold with a pulsed frequency doubled Nd:YAG laser and monitored the fluorescence to the ground state.

The unquenched lifetime of the $^5S_2$ manifold, measured for low concentration (1%) samples, was found to be 285 μs for Ho:BYF and 97 μs for Ho:YLF. As the concentration of Ho^{3+} was increased to 10%, the lifetime of $^5S_2$ shortened significantly: 15.5 μs for Ho:BYF and 5.2 μs for Ho:YLF (see Table 1). Thus, the pulse duration of 20 ns of Q-switched, frequency-doubled Nd:YAG laser is much shorter than the smallest time constant (in this case, the lifetime of $^5S_2$ manifold) in the system of energy levels participating in the cascade process. This allows the cascade lasing to take place on much shorter time scale than the decay lifetimes of Ho^{3+} energy levels. Since the input-to-

Reproduced with permission of the copyright owner. Further reproduction prohibited without permission.

output pulse delay is typically less than 100 ns and the fluorescence lifetime of $^5S_2$ is much longer, even in high concentration samples, the storage efficiency is essentially unity.

4.3. Demonstration of laser action at 3.9 μm in Ho:BaY$_2$F$_8$ with short pulse excitation at 532 nm

In our experiments we achieved cascade laser action at 1.39 μm and 3.9 μm in 10% Ho:BaY$_2$F$_8$ (Ho:BYF) pumped by Q-switched, frequency-doubled Nd:YAG laser at 532 nm. The laser cavity (Figure 30) consisted of a 1 m radius of curvature input mirror HR-coated near 1.4 and 3.9 μm, and a flat output coupler coated for high reflection at 1.4 μm and 94% reflection at 3.9 μm. The 6 mm long (uncoated) Ho:BYF crystal was placed near the output coupler.

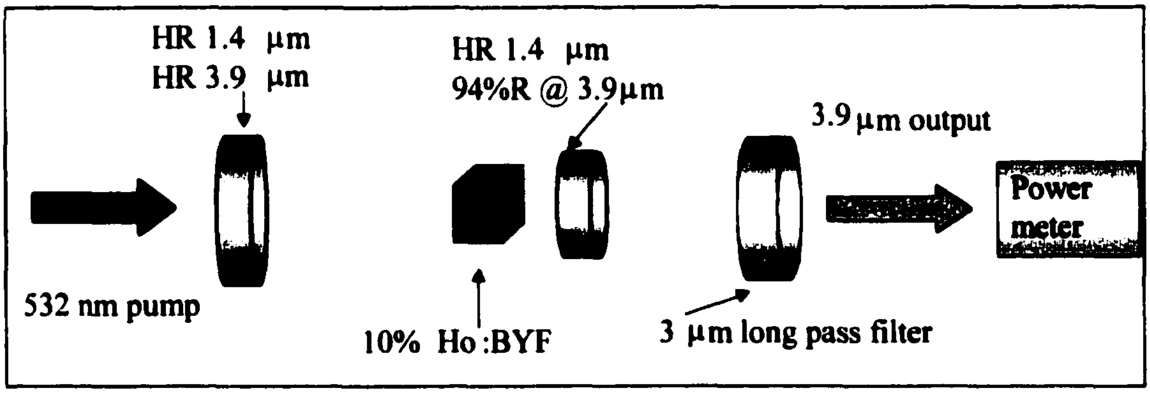

Figure 30. Cavity layout for 3.9 μm Ho:BYF laser with pulsed resonant pumping at 532nm.

Reproduced with permission of the copyright owner. Further reproduction prohibited without permission.

The cavity was end-pumped with 20 ns pulses at 532 nm, at a repetition rate of 10 Hz. A halfwave plate/polarizer combination was used to continuously vary the pump energy, and a second halfwave plate allowed optimal alignment of the pump polarization with respect to the crystal axis. Lasing at 1.39 μm was achieved with a low threshold of 1mJ absorbed pump energy. Threshold for cascade lasing at 3.9 μm was reached at approximately 5 mJ of absorbed pump energy at 532 nm. A maximum output of 2.6 mJ was achieved at absorbed pump energy of 30 mJ. This corresponds to a slope efficiency of 10.4% (Figure 31) or quantum efficiency of 76.5%, which is near theoretical.

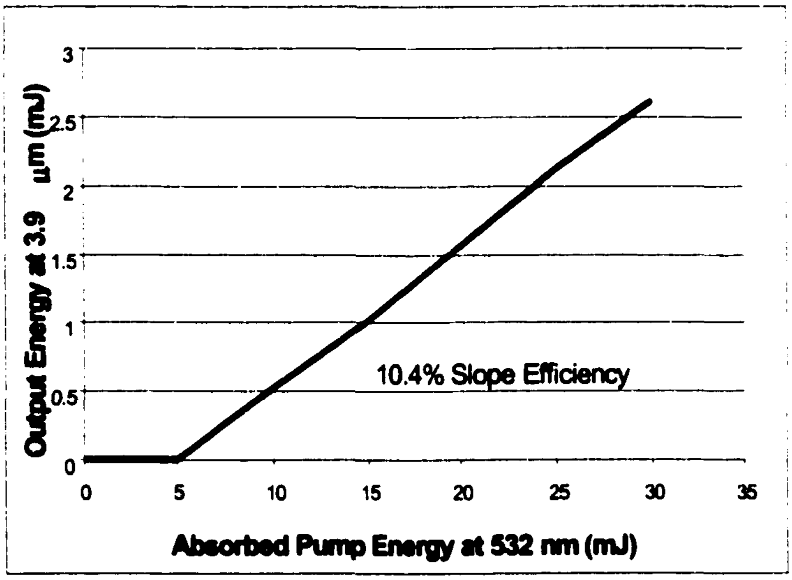

Figure 31. Performance of the 3.9 μm laser transition in 10% Ho:BYF with pulsed resonant pumping at 532nm.

Some problems associated with pulsed pumping have to be taken into account. First, the repetition rate is limited by the long lifetime of $^5I_6$, the lower level of the 3.9 μm transition, which creates a bottleneck effect and causes laser action to be self-terminating.

Reproduced with permission of the copyright owner. Further reproduction prohibited without permission.

Second, if the laser crystal is end-pumped, the Q-switched pump pulse can damage the optics in the cavity.

To extend the mid-infrared laser operation to higher repetition rates, or even to cw regime, a mechanism has to be found to empty the population in the long lived lower energy levels, thereby maintaining population inversion by effectively reducing the lower level lifetimes.

Reproduced with permission of the copyright owner. Further reproduction prohibited without permission.

CHAPTER 5. NEAR IR CASCADE CW PUMPING SCHEME OF HO:BYF AND HO:YLF AT 750 NM

5.1 Mid-infrared 3.9 μm laser concept with cw pumping at 750 nm

Spectroscopic evaluations of Ho:YLF and Ho:BYF indicates that 3.9 μm $^5I_5 \rightarrow {}^5I_6$ laser dynamics may lend itself to resonant cascade pumping by cw laser radiation at 750 nm due to a fortuitous coincidence of ground state absorption $^5I_8 \rightarrow {}^5I_4$, and excited state absorption $^5I_7 \rightarrow {}^5S_2$ (Figure 32) combined with the efficient cross relaxation in high concentration crystals.

Later spectroscopic studies also pointed to the intriguing possibility that a third absorption process from the $^5I_6$ level may exist at the same wavelength of 750 nm, which would make it possible to break the bottleneck on the $^5I_5 \rightarrow {}^5I_6$ transition at 3.9 μm, using a single wavelength pump. Initial modeling of the cw resonant pumping at 750 nm of the 3.9 μm laser, however, was based on two step cascade pump absorption and efficient cross relaxation in high concentration Ho:BYF and Ho:YLF.

A pump at 750 nm excites Ho ions from the ground state $^5I_8$ to the upper manifold $^5I_4$ with a relatively weak cross section, $\sigma_{5I8\text{-}5I4} = 8 \cdot 10^{-23}\text{cm}^2$. This is followed by multiphonon relaxation to lower levels, in particular the $^5I_7$ level, providing these levels an initial population. Ions are then pumped from the $^5I_7$ level to the $^5S_2$ level by the same

Reproduced with permission of the copyright owner. Further reproduction prohibited without permission.

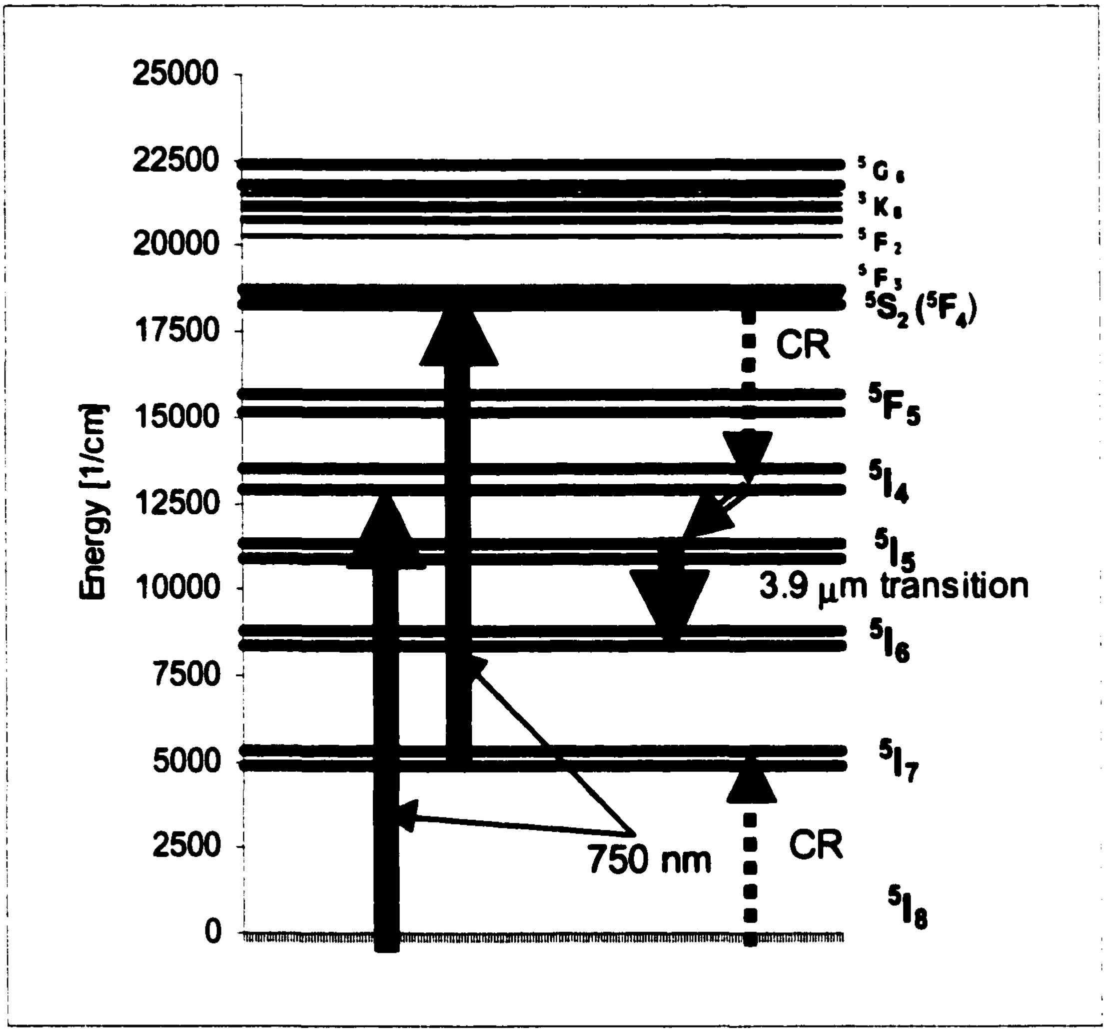

Figure 32. Mid-infrared 3.9 µm laser concept in Ho^{3+} doped fluorides with cw pumping at 750 nm.

750 nm pump, but the cross section of this transition is much larger: $\sigma_{5I7\text{-}5S2} = 4\cdot10^{-20}$ cm^2.

Resonant cross relaxation (CR) process – simultaneous transitions from $^5S_2$ to $^5I_4$ and from $^5I_8$ to $^5I_7$ - is very efficient at the higher Ho^{3+} concentrations desirable for laser

Reproduced with permission of the copyright owner. Further reproduction prohibited without permission.

applications (10% to 20%). It shortens the lifetime of the $^5S_2$ level through rapid relaxation from $^5S_2$ to $^5I_4$, followed by multiphonon relaxation from $^5I_4$ to $^5I_5$, and efficiently contributes to the buildup of population on $^5I_5$, the upper level of the 3.9 μm laser transition. The cross relaxation rate, as it was described in Chapter 3, can be determined by observing the change in lifetime of the $^5S_2$ manifold with changing Ho^{3+} concentration. The model we will use for the calculation of population dynamics on Ho^{3+} energy levels describes the rate of population removal from $^5S_2$ level due to cross relaxation as:

$$dN_{5S2}/dt \text{ (due to cross relaxation)} = -\alpha_{CR} N_{5I8} N_{5S2}$$

where α_{CR} is the cross relaxation rate constant, N_{5I8} is the ground state $^5I_8$ population, N_{5S2} is the population of the $^5S_2$ level.

In the nonlinear term $\alpha_{CR} N_{5I8} N_{5S2}$ responsible for cross relaxation, the product $\alpha_{CR} N_{5I8}$ can be interpreted as a cross relaxation rate or reciprocal of the lifetime of $^5S_2$ level shortened by cross relaxation as:

$$1/\tau_{CR} = \alpha_{CR} N_{5I8}$$

Using the lifetime measurement apparatus described in Chapter 3 we measured the values of τ_{CR} for different concentration samples (see Table 1). The unquenched lifetimes of $^5S_2$ manifold were found to be 97 μs for Ho:YLF and 280 μs for Ho:BYF in low concentration (1%) samples. As the concentration of Ho was increased, the lifetime

Reproduced with permission of the copyright owner. Further reproduction prohibited without permission.

of $^5S_2$ shortened dramatically: τ_{CR} = 2 μs in 20% Ho:YLF, and τ_{CR} = 3.7 μs in 20% Ho:BYF.

The rate of cross relaxation, as we can see, depends on population of the ground state. The analysis has shown that with high enough pumping density, it is possible to deplete effectively the ground state population of Ho^{3+} ions without the direct influence on this state by external radiation (ground state absorption). The necessary condition for this process is the cross relaxation duplication of excitations in the system of interacting particles and the effective excited state absorption. The depletion of the ground state will lead to the slowing of the cross relaxation process by increasing the τ_{CR} time constant.

5.2. Numerical modeling of near IR cw pumping of Ho:BYF and Ho:YLF at 750 nm

Numerical modeling of the 3.9 μm laser operation is based on the energy level diagram of Ho^{3+}, shown on Figure 32. The goal of our calculations was to determine under what conditions a population inversion could be achieved between the $^5I_5$ and $^5I_6$ levels using a cw pump at 750 nm.

A system of 7 coupled differential rate equations was used to describe the temporal development of the populations of the Ho^{3+} energy levels $^5I_8$, $^5I_7$, $^5I_6$, $^5I_5$, $^5I_4$, $^5F_5$, and $^5S_2$. Initially the model assumed that pumping at 750 nm results in transitions from $^5I_8$ to $^5I_4$ – ground state absorption (GSA) and from $^5I_7$ to $^5S_2$ – excited state absorption (ESA). The resonant cross relaxation process was taken into account for high concentration samples. These considerations mean that the nonlinear terms due to cross relaxation are included in the system of rate equations. As it was mentioned above, these

Reproduced with permission of the copyright owner. Further reproduction prohibited without permission.

terms are proportional to the product of the population of the ground level ${}^5I_8$ and the population of level ${}^5S_2$.

The system of equations was solved for the case of threshold for 3.9 μm lasing, without taking into account stimulated emission and stimulated absorption between the levels ${}^5I_5$ and ${}^5I_6$. The rate equations describing our model are:

$$
\begin{aligned}
&N_{{}^5I_8} = N_0 - N_{{}^5I_7} - N_{{}^5I_6} - N_{{}^5I_5} - N_{{}^5I_4} - N_{{}^5F_5} - N_{{}^5S_2} \\
&\frac{dN_{{}^5I_7}}{dt} = -\sigma_{{}^5I_7-{}^5S_2} R_{{}^5I_7-{}^5S_2} N_{{}^5I_7} - \frac{N_{{}^5I_7}}{\tau_{{}^5I_7}} + \beta_1 \frac{N_{{}^5I_6}}{\tau_{{}^5I_6}} + \alpha_{CR} N_{{}^5I_8} N_{{}^5S_2} \\
&\frac{dN_{{}^5I_6}}{dt} = -\frac{N_{{}^5I_6}}{\tau_{{}^5I_6}} + \frac{N_{{}^5I_5}}{\tau_{{}^5I_5}} \\
&\frac{dN_{{}^5I_5}}{dt} = -\frac{N_{{}^5I_5}}{\tau_{{}^5I_5}} + \frac{N_{{}^5I_4}}{\tau_{{}^5I_4}} \\
&\frac{dN_{{}^5I_4}}{dt} = \sigma_{{}^5I_8-{}^5I_4} R_{{}^5I_8-{}^5I_4} N_{{}^5I_8} - \frac{N_{{}^5I_4}}{\tau_{{}^5I_4}} + \beta_2 \frac{N_{{}^5F_5}}{\tau_{{}^5F_5}} + \alpha_{CR} N_{{}^5I_8} N_{{}^5S_2} \\
&\frac{dN_{{}^5F_5}}{dt} = -\frac{N_{{}^5F_5}}{\tau_{{}^5F_5}} + \beta_3 \frac{N_{{}^5S_2}}{\tau_{{}^5S_2}} \\
&\frac{dN_{{}^5S_2}}{dt} = \sigma_{{}^5I_7-{}^5S_2} R_{{}^5I_7-{}^5S_2} N_{{}^5I_7} - \frac{N_{{}^5S_2}}{\tau_{{}^5S_2}} - \alpha_{CR} N_{{}^5I_8} N_{{}^5S_2} \qquad (5.2.1)
\end{aligned}
$$

where, N_0 is the concentration of Ho^{3+} ions in crystal; τ are the lifetimes of corresponding levels; σ – the cross sections of corresponding transitions; R – the number of pump photons per unit area per unit time; $\alpha_{CR} N_{5I8} = \alpha'$ is the cross relaxation rate; β – the feeding efficiencies to corresponding levels from the levels above them.

Reproduced with permission of the copyright owner. Further reproduction prohibited without permission.

The time dependencies of energy level populations were calculated using the forward Euler procedure [41], with the time increment equal to the smallest time constant in the rate equations. The steady-state solutions for different pump conditions were found using *Mathematica* software. The initial population of the ground state was calculated taking into account the concentration of the Ho^{3+} ions. Since the rare earth ions of Ho^{3+} enter substitutionally into the Y^{3+} site, the initial population of the ground state at each particular concentration can be found using the values of densities of Y^{3+} sites in YLF ($1.39 \cdot 10^{22}$ 1/cm^3) and in BYF ($1.30 \cdot 10^{22}$ 1/cm^3).

5.3. Calculations of population dynamics on Ho^{3+} energy levels

The original system of 7 coupled differential equations is quite complex, and interpretation of its solutions is not always trivial. For that reason, we began with a simplified model including fewer energy levels, and then included the others one by one.

In the starting model, the pump term $^5I_8 \rightarrow {}^5I_4$ was omitted, and instead we assumed an initial population in the $^5I_7$ level which is being pumped to the $^5S_2$ level. Cross relaxation results in transitions from $^5I_8 \rightarrow {}^5I_7$ and simultaneously from $^5S_2 \rightarrow {}^5I_4$. We also assumed relaxation from the $^5I_4$ level to the $^5I_7$ level. As a result, excitation of a single ion from $^5I_7$ to $^5S_2$ results in two ions in the $^5I_7$ level: one through relaxation from upper levels ($^5S_2 \rightarrow {}^5I_4 \rightarrow {}^5I_7$) and one through cross relaxation ($^5I_8 \rightarrow {}^5I_7$). The actual outcome depends on the quantum efficiencies of various processes. As an example, if both, the cross relaxation ($^5S_2 \rightarrow {}^5I_4$ and $^5I_8 \rightarrow {}^5I_7$) and the multiphonon relaxation ($^5I_4 \rightarrow {}^5I_7$) are 90% efficient, one excitation from $^5I_7$ to $^5S_2$ results in 1.7 ions in the $^5I_7$ level. By solving this simplified model we can conclude, that the steady state population of the $^5I_7$

Reproduced with permission of the copyright owner. Further reproduction prohibited without permission.

level is independent of the initial population on that level. This held true at every power level specified for the 750 nm pump as well. A higher initial population in $^5I_7$ served only to bring the system to a steady state faster. In this manner we were able to check the significance for building up the steady state population of $^5I_7$ of the pump term $^5I_8 \rightarrow {}^5I_4$ that we have neglected so far. It turns out that the final steady state values are not affected by pumping from the ground state. The transition $^5I_8 \rightarrow {}^5I_4$ only provides an initial population for the $^5I_7$ level. The other processes in the system (cross relaxation, pumping from $^5I_7$ to $^5S_2$) take over later and bring the system to the same steady state populations.

The next step in the numerical modeling of the system was the addition of the $^5I_6$ and $^5I_5$ levels. The calculations for this system show that the steady state population of the $^5I_6$ level increases with the pump rate (Figure 33). Meanwhile the steady state population of $^5I_7$ first increases, then, starting from 4 kW/cm^2 of pump intensity, it decreases as pump rate is increased further.

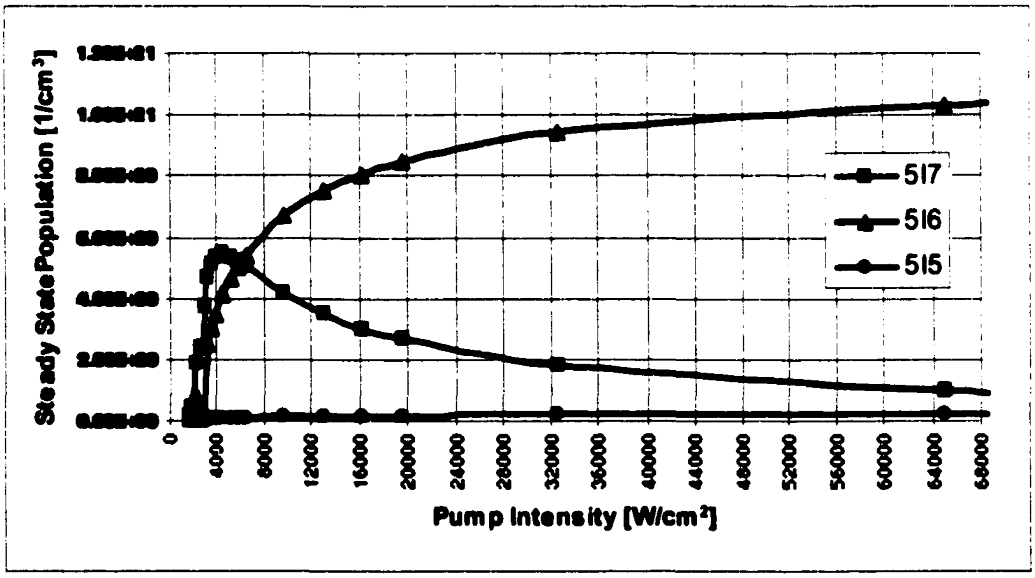

Figure 33. Calculated steady state populations of Ho^{3+} energy levels vs. pump intensity.

Reproduced with permission of the copyright owner. Further reproduction prohibited without permission.

The $^5I_6$ population builds up to quite large values due to the long lifetime of the level (2.2 ms for Ho:YLF and 5.5 ms for Ho:BYF). The $^5I_7$ population decreases, however, in spite of having an even longer lifetime and being fed through cross relaxation, since increasing pump power efficiently empties this level. We believed that the population inversion between $^5I_6$ and $^5I_7$ obtained at pump intensities as low as 6 kW/cm^2 can be used to deplete the $^5I_6$ level through lasing from $^5I_6$ to $^5I_7$. The steady state population of $^5I_5$ is lower than that of $^5I_6$ throughout the entire range of pump rates.

As we see, we cannot obtain a population inversion between the $^5I_5$ and $^5I_6$ levels using only a cw pump at 750 nm. The main culprit here is the long lifetime of the lower laser level $^5I_6$ compared with that of the upper level $^5I_5$, which results in the so-called bottleneck effect. The only way to break the bottleneck due to this unfavorable lifetime ratio is to find a mechanism whereby the population of $^5I_6$ is emptied effectively reducing the corresponding level lifetime and helping to maintain a population inversion.

There are two possible ways of depleting the population on level $^5I_6$: pumping from $^5I_6$ to some higher manifold, or lasing from $^5I_6$ to $^5I_7$ at 2.96 μm. In the final step of our model we've included depletion of the $^5I_6$ level, and added in pumping from the ground state. Everything else was kept the same as in the previous step. The depletion of the $^5I_6$ level through lasing from $^5I_6$ to $^5I_7$ at 2.9μm was taken into account (Figure 34) by changing the effective lifetime of $^5I_6$.

The calculations result in the following steady state populations, assuming 2 W pump power at 750 nm focused in 30 μm spot, and the effective lifetime of $^5I_6$ reduced to 50 μs through lasing from $^5I_6$ to $^5I_7$: $N = 9.4\cdot10^{19}$ cm^{-3} for $^5I_7$ level, $N = 2.1\cdot10^{20}$ cm^{-3} for $^5I_6$ level, and $N = 1.39\cdot10^{20}$ cm^{-3} for $^5I_5$ level. There is still no population inversion

Reproduced with permission of the copyright owner. Further reproduction prohibited without permission.

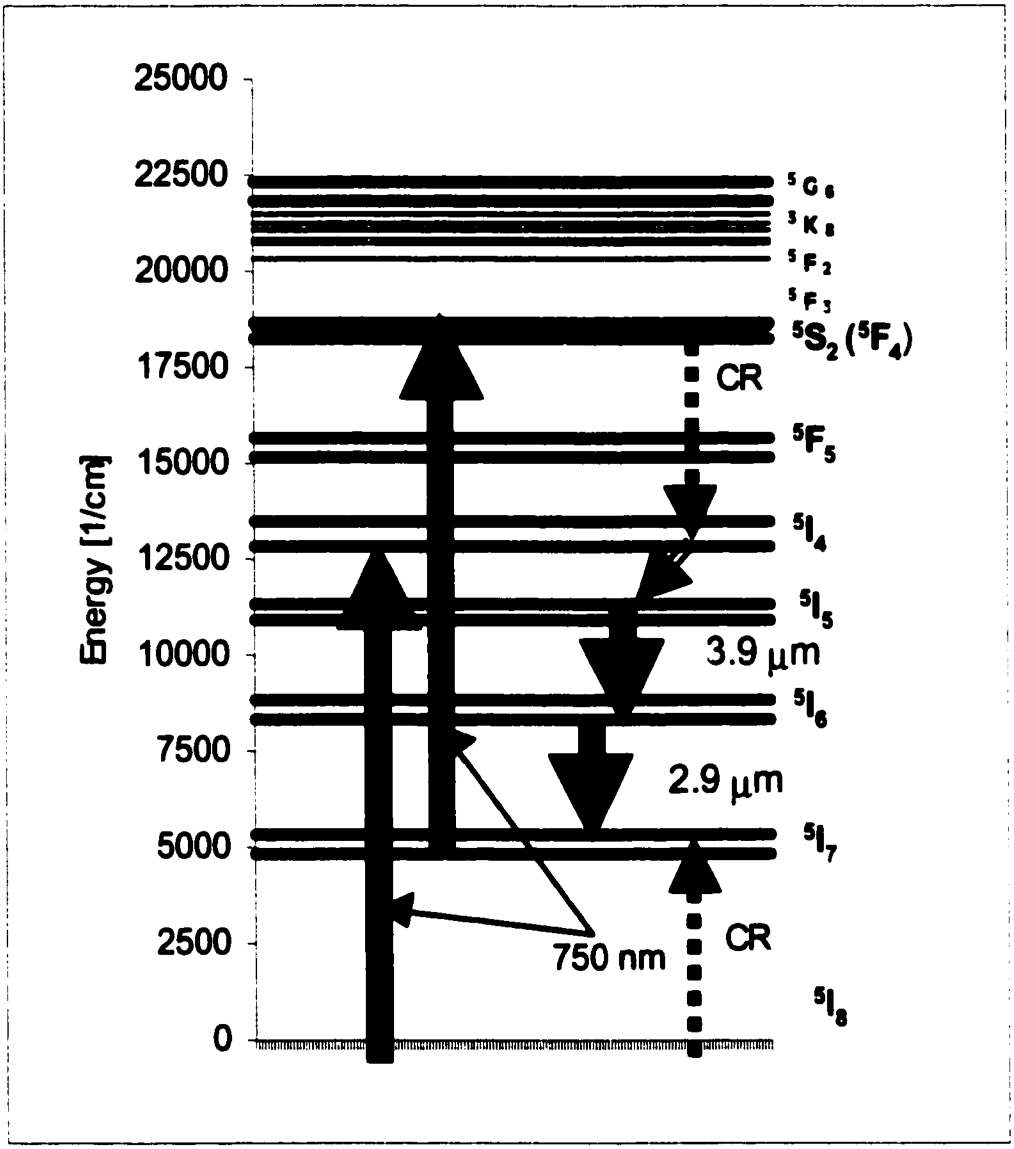

Figure 34. Resonant cw pumping scheme at 750 nm with cascade lasing at 3.9 μm and 2.9 μm.

between the levels $^5I_5$ and $^5I_6$. If we assume, however, that lasing from $^5I_6$ to $^5I_7$ reduces the effective lifetime of $^5I_6$ to 20 μs, the steady state populations become: $N = 9.97 \cdot 10^{19}$ cm^{-3} for $^5I_7$ level, $N = 1.42 \cdot 10^{20}$ cm^{-3} for $^5I_6$ level, and $N = 1.48 \cdot 10^{20}$ cm^{-3} for $^5I_5$ level. In

Reproduced with permission of the copyright owner. Further reproduction prohibited without permission.

this case, there is a population inversion between $^5I_6$ and $^5I_7$ ($\Delta N = 4.2 \cdot 10^{19}$ cm^{-3}), as well as between $^5I_5$ and $^5I_6$ ($\Delta N = 6 \cdot 10^{18}$ cm^{-3}). If the pump power is reduced to 1.6 W and the effective lifetime of $^5I_6$ to 10 μs, the steady state populations are: $N = 1.23 \cdot 10^{20}$ cm^{-3} for $^5I_7$ level, $N = 1.34 \cdot 10^{20}$ cm^{-3} for $^5I_6$ level, and $N = 1.46 \cdot 10^{20}$ cm^{-3} for $^5I_5$ level. Again, there is a population inversion both between $^5I_6$ and $^5I_7$ ($\Delta N = 1.1 \cdot 10^{19}$ cm^{-3}), and between $^5I_5$ and $^5I_6$ ($\Delta N = 1.2 \cdot 10^{19}$ cm^{-3}).

These population inversions $\Delta N \sim 10^{19}$ cm^{-3} and the typical cross sections $\sigma \sim 10^{-20}$ cm^2 imply a small-signal gain coefficient γ on the order of 0.1 cm^{-1}. The small signal power gain is given by $G = \exp(\sigma \Delta N L)$ where L is the length of the crystal. Threshold for laser oscillation is determined by the requirement that the round-trip gain in the cavity exceed 1. If one considers only mirror losses, then the threshold condition is:

$$R_1 R_2 \exp(\sigma \Delta N 2L) \geq 1 \quad \text{or}$$

$$\gamma \geq 1/2L \ \ln(1/R_1 R_2)$$

where R_1 and R_2 are the reflectivities of the cavity mirrors. Assuming both mirrors have a reflectivity of 99%, the gain per unit length at a population inversion $\Delta N \sim 10^{19}$ cm^{-3} exceeds the loss.

In order to check the results of theoretical calculations, Z-scan measurements (described later) have been done. The numerical model is in a good agreement with experimental Z-scan measurements of fluorescence for Ho:YLF. In Ho:BYF, however, we discovered new energy transfer processes that efficiently deplete $^5I_6$ level, and can be used to break the bottleneck created by long lifetime of that level.

Reproduced with permission of the copyright owner. Further reproduction prohibited without permission.

The numerical model for 3.9 μm Ho:BYF laser with cw pumping at 750 nm was upgraded with the account of the depletion of lower level of the 3.9 μm transition due to the third step absorption at 750 nm. The cross section of this possible excited state absorption is not known, therefore it was used as an input parameter in the model. Assuming that the $^5I_6$ – $^5G_6$ excited state absorption cross section is of the same order of magnitude as $^5I_7$ – $^5S_2$ cross section, the following results were obtained:

-the population on $^5I_5$ level in steady state will reach the value of $^5I_6$ population with 800 mW cw pump radiation at 750 nm focused in 30 μm spot;

-increasing pump power to 1 W will allow to achieve inversion of population $\Delta N \sim 10^{19}$ cm^{-3}, which would be adequate for obtaining efficient laser action.

5.4. Z-scan measurements: synergy of fluorescence and nonlinear transmission data

The fortuitous coincidence of ground state absorption $^5I_8 \rightarrow {}^5I_4$ and excited state absorption $^5I_7 \rightarrow {}^5S_2$ at 750 nm, combined with efficient cross relaxation processes in high concentrations samples, leads to certain redistribution of populations on Ho^{3+} energy levels. Numerical modeling for Ho^{3+} energy levels has allowed determining steady state values for populations of levels at different pump intensities as well as their temporal development. In order to check the results of model calculations, Z-scan measurements have been carried out.

5.4.1. Z-scan measurements of nonlinear transmission

The measurements of nonlinear transmission were performed with the sensitive single-beam technique, widely known as a Z-scan method [42]. Using a single Gaussian

Reproduced with permission of the copyright owner. Further reproduction prohibited without permission.

laser beam in a tight focus geometry, as depicted in Figure 35, we measured the transmission of nonlinear medium (Ho:BYF crystal) through an open aperture in the near field upon the translation of the crystal along the focused pump beam.

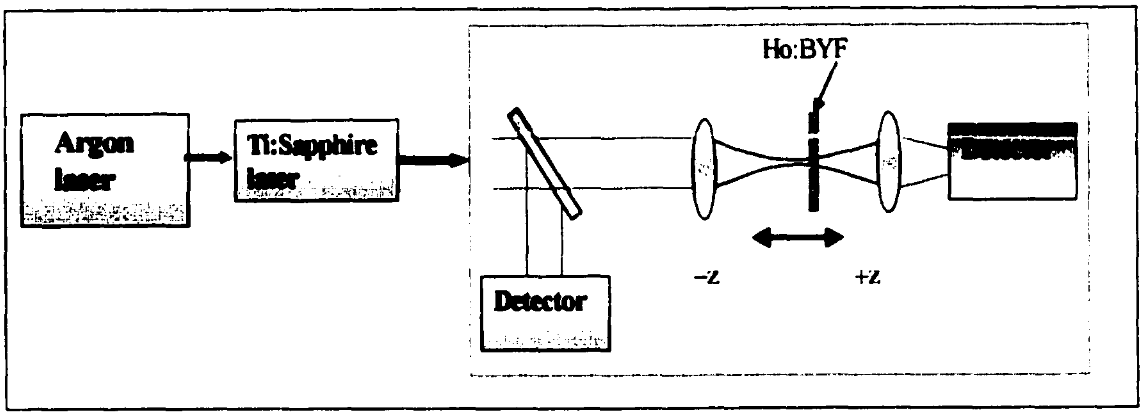

Figure 35. Set-up for measurements of nonlinear absorption of Ho^{3+} doped fluorides at 750nm.

The absorption of Ho-doped YLF and BYF at 750 nm increases with the pump intensity. This type of nonlinear absorption is known as "Reverse Saturable Absorption" (RSA). It arises from cascade two step absorption at 750 nm in Ho^{3+}: ground state absorption from $^5I_8$ to $^5I_4$ and excited state absorption from $^5I_7$ to $^5S_2$. The cross section of ground state absorption (GSA) is much smaller than cross section of the excited state absorption (ESA) $\sigma_{5I8\text{-}5I4} < \sigma_{5I7\text{-}5S2}$, which leads to RSA. As we demonstrated in Chapter 3, the ground state absorption cross section at 750 nm is $\sigma_{5I8\text{-}5I4} = 8 \cdot 10^{-23}$ cm^2 in Ho:BYF, and $\sigma_{5I8\text{-}5I4} = 9.3 \cdot 10^{-23}$ cm^2 in Ho:YLF, whereas the excited state absorption cross section is reported in the literature $\sigma_{5I7\text{-}5S2} = 4 \cdot 10^{-20}$ cm^2 for Ho:YLF, and it is expected to be the same order of magnitude for Ho:BYF.

Reproduced with permission of the copyright owner. Further reproduction prohibited without permission.

In the experiment we have measured the transmission of Ho^{3+} doped samples at 750 nm as a function of pump intensity. A Ti:Sapphire laser pumped by argon ion laser was used as a pump source. The configuration of the 4-mirror X-fold cavity was based on the design of Schwartz Electro-Optics. A birefringent filter, installed within the cavity, was used for wavelength tuning. Ti:Sapphire laser was assembled and optimized by the author. It could provide up to 650 mW of cw radiation continuously tunable from 710 nm to 760 nm. The beam from Ti:Sapphire laser was directed through the beam splitter to the sample (Figure 35). Small part of the beam was reflected to the reference detector #1 for the simultaneous monitoring of incident pump power. Another part of the pump beam was focused by a 38.1 mm focal length lens on the sample. The sample was mounted on a motorized micrometer stage to permit its translation along the focused gaussian beam. The light transmitted through the sample was collected with the second lens on the detector #2. For the measurements of nonlinear absorption we used optically thin samples (the thickness of the sample should be comparable with the depth of focus of the lens, that focuses the pump into the sample).

The measurements were performed for two different samples of Ho:BYF (10% and 20%) for the pump intensities ranging from about 9.46 kW/cm^2 to 64.081 kW/cm^2. For 10% Ho:BYF, we observed 15% drop in transmission compared to linear transmission, which is about 99% (Figure 36). For 20% Ho:BYF, we observed 25% drop in transmission for pump polarization parallel to x-axis of crystal, and 35% drop in transmission for pump polarization parallel to z-axis of crystal (Figure 37).

Reproduced with permission of the copyright owner. Further reproduction prohibited without permission.

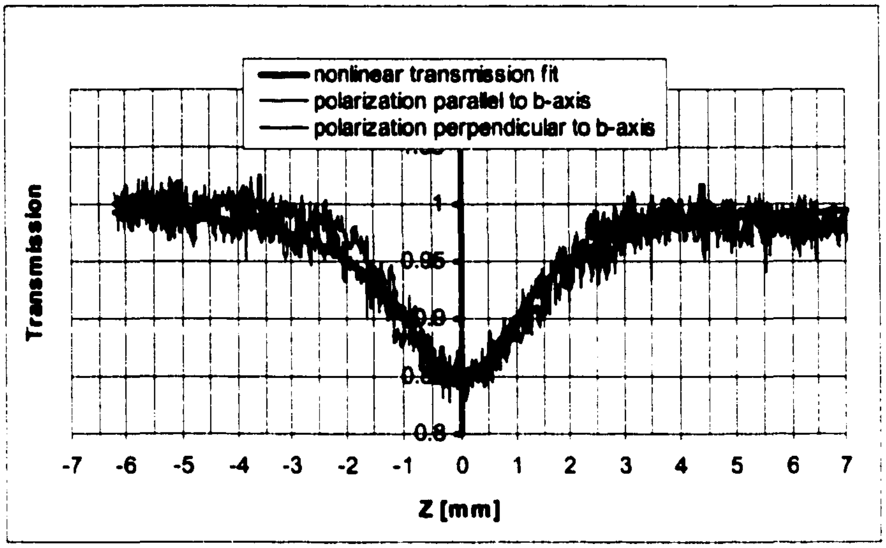

Figure 36. Nonlinear transmission of 10% Ho:BYF at 750 nm as a function of Z and theoretical fit.

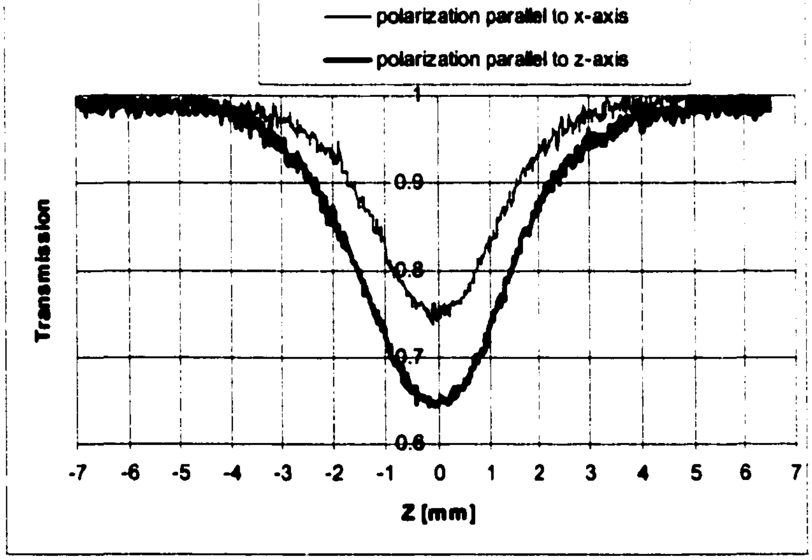

Figure 37. Nonlinear transmission of 20% Ho:BYF at 750 nm as a function of Z.

Reproduced with permission of the copyright owner. Further reproduction prohibited without permission.

5.4.2. Theory of nonlinear transmission

The simple model of nonlinear transmission one can develop shall assume a linear dependence of the absorption coefficient on the intensity of radiation. Thus,

$$\alpha = \alpha_0 + \alpha_2 I(z) \tag{5.1}$$

where α is the effective absorption coefficient; α_0 is the linear part of the absorption coefficient, and α_2, measured in cm/W, determines the strength of the nonlinear absorption. The dependence of the effective absorption coefficient on the coordinate is determined by its dependence on the intensity of the incident radiation I.

The equation describing the attenuation of the light intensity is

$$\frac{dI}{dz} = -(\alpha_0 + \alpha_2 I)I \tag{5.2}$$

where the diffraction effects are neglected. The Eq. (5.2) describes the standard two-photon absorption. In our case, however, the mechanism of nonlinearity is the cascade two step absorption.

The solution of Eq. (2) is

$$I(z) = \frac{I_i e^{-\alpha_0 z}}{1 + \alpha_2 I_i \left(1 - e^{-\alpha_0 z}\right)/\alpha_0} \tag{5.3}$$

where I_i is the intensity of radiation incident on the material. To find out the transmission of the material (of thickness L) for the total power, let us assume a Gaussian transverse profile for the incident beam:

Reproduced with permission of the copyright owner. Further reproduction prohibited without permission.

$$I_i = I_0 e^{-2r^2/w^2} \tag{5.4}$$

Integrating the expression (3.5) yields

$$P = P_0 e^{-\alpha_0 L} \frac{\ln(1+\eta)}{\eta} \tag{5.5}$$

where

$$\eta = \alpha_2 I_0(z) \frac{1-e^{-\alpha_0 L}}{\alpha_0} \tag{5.6}$$

In our experiments, $I_0(z)$ is the peak intensity on axis at z position of the crystal relative to focal plane of the lens. Therefore,

$$I_0(z) = \frac{2P_0}{\pi w_0^2} \frac{1}{1+(z/z_0)^2} \tag{5.7}$$

In Eq. (5.7), z_0 is the Rayleigh range, $z_0 = \pi w_0^2/\lambda$, and w_0 is the beam waist radius at the focal spot, $w_0 = \lambda f/\pi w$, where w is the beam radius at the focusing lens, and f is the focal length of the lens. Thus

Reproduced with permission of the copyright owner. Further reproduction prohibited without permission.

$$z_0 = \frac{\lambda f^2}{\pi w^2} \tag{5.8}$$

and

$$\eta = \alpha_2 \frac{2P_0}{\pi w_0^{\;2}} \frac{1-e^{-\alpha_0 L}}{\alpha_0} \frac{1}{1+(z/z_0)^2} \equiv \frac{A}{1+(z/z_0)^2} \tag{5.9}$$

where

$$A = \alpha_2 \frac{2P_0}{\pi w_0^{\;2}} \frac{1-e^{-\alpha_0 L}}{\alpha_0} = \frac{2\pi\alpha_2 w^{\;2}}{\lambda^2} \frac{1-e^{-\alpha_0 L}}{\alpha_0} \frac{P_0}{f^2} \tag{5.10}$$

Since we can measure in a single experiment both the transmitted power in the linear regime $P_L = P_0\exp(-\alpha_0 L)$ and the transmitted power in the nonlinear regime, P_{NL}, we will fit the experimental results with the aid of the formula

$$T = \frac{P_{NL}}{P_L} = \frac{\ln(1+\eta)}{\eta} \tag{5.11}$$

The results of the fits are shown in Figure 36. In 10% Ho:BYF we observed similar drop in transmission for two different orientations of the crystal relative to polarization of the incident light. The theoretical curve fits both of nonlinear transmission

Reproduced with permission of the copyright owner. Further reproduction prohibited without permission.

curves very well. The fitted curve allows to estimate the population of $^5I_7$ level, from which the second step absorption originates.

Considering the fact that the excited state absorption is about three orders of magnitude stronger than ground state absorption, we can analyze the limiting case with $\alpha_0 \rightarrow 0$, which will result in simplified version of theoretical treatment presented above. All the notations in simplified theory are kept the same as before.

Thus, in the case when $\alpha_0 \rightarrow 0$ the expression for absorption coefficient will be:

$$\alpha = \alpha_2 I(z) \tag{5.12}$$

The equation describing the attenuation of the light intensity as a function of crystal position relative to the focal plane will change to:

$$\frac{dI}{dz} = -\alpha_2 I^2 \tag{5.13}$$

The solution of Eq. (5.13) is

$$I(z) = \frac{I_i}{1 + \alpha_2 I_i z} \tag{5.14}$$

where I_i is the intensity of radiation incident on the material. Again, assuming a Gaussian transverse profile for the incident beam (4) and integrating the expression (5.14) in order to find the transmission of the material (of thickness L) for the total power yields

$$P = P_0 e^{-\alpha_0 L} \frac{\ln(1+\eta)}{\eta} \tag{5.15}$$

Reproduced with permission of the copyright owner. Further reproduction prohibited without permission.

where

$$\eta = \alpha_2 I_0(z) L \tag{5.16}$$

As before, I_0 is the peak intensity on axis at certain position z of the crystal. Therefore,

$$I_0(z) = \frac{2P_0}{\pi w_0^2} \frac{1}{1+(z/z_0)^2} = I_{\max} \frac{1}{1+(z/z_0)^2} \tag{5.17}$$

with the on axis intensity in a focal plane (pump beam waist) $I_{max} = I_0(z = 0)$. By substituting simplified expression (5.16) into (5.11) we obtain:

$$T = \frac{P_{NL}}{P_L} = \frac{\ln(1+\alpha_2 I_0(z)L)}{\alpha_2 I_0(z)L} \tag{5.18}$$

The theoretical fit of nonlinear transmission curves in 10% Ho:BYF allows one to estimate the nonlinear absorption coefficient $\alpha_2 = 5.85 \cdot 10^{-5}$ cm/W. The knowledge of α_2 allows to estimate the population of $^5I_7$ level, from which the second step absorption originates in a following manner. The absorption coefficient can also be expressed through populations of energy levels and cross sections of transitions as :

$$\alpha = \sigma_{5I8-5I4}(N_{5I8} - N_{5I4}) + \sigma_{5I7-5S2}(N_{5I7} - N_{5S2}) \tag{5.19}$$

Reproduced with permission of the copyright owner. Further reproduction prohibited without permission.

where the first term in the sum is simply ground state absorption α_0 and the second is excited state absorption. Comparing the equations (5.2) and (5.19) and equalizing the right hand sides we obtain:

$$\alpha_2 I_0(z) = \sigma_{5I7-5S2} N_{5I7} \tag{5.20}$$

where the valid assumption was made that $N_{5I7} >> N_{5S2}$. From equation (5.20), the value of the $N(^5I_7) = 9 \cdot 10^{19}$ cm^{-3} was estimated, which is about 7.2% of total concentration of Ho^{3+} ions deposited in $^5I_7$ manifold. Substituting (5.20) into (5.18) we obtained the value of nonlinear transmission in the pump beam waist $T(z = 0) = 85\%$, which is in excellent agreement with experimentally observed 15% decrease in transmission at maximum pump intensity in10% Ho:BYF (Figure 36).

The nonlinear transmission curve of 20% Ho:BYF (Figure 37), however, was not possible to fit with the theoretical curve assuming cascade two step absorption. The actual drop in transmission was higher than predicted with theory. The possible explanation of this effect is the presence of strong upconversion process in 20% Ho:BYF (described more in details in the following sections) which deposits some additional population in $^5I_7$ manifold, thereby increasing nonlinear absorption.

5.4.3. Z-scan measurements of fluorescence

The alternative way of characterizing two step absorption combined with cross relaxation process was measurement of efficiency of fluorescence from $^5S_2$ and $^5I_5$ manifolds as a function of pump intensity. The beam from Ti:Sapphire laser was focused into the sample (Figure 38). Fluorescence from the sample was collected in the direction

Reproduced with permission of the copyright owner. Further reproduction prohibited without permission.

perpendicular to the direction of propagation of pump beam. Since the sample had to be aligned with detection system, its position was fixed. Instead, focusing lens, mounted on a motorized stage, was moving along Z direction to permit translation of the focus with respect to the sample, and therefore changing the intensity of pump at 750nm.

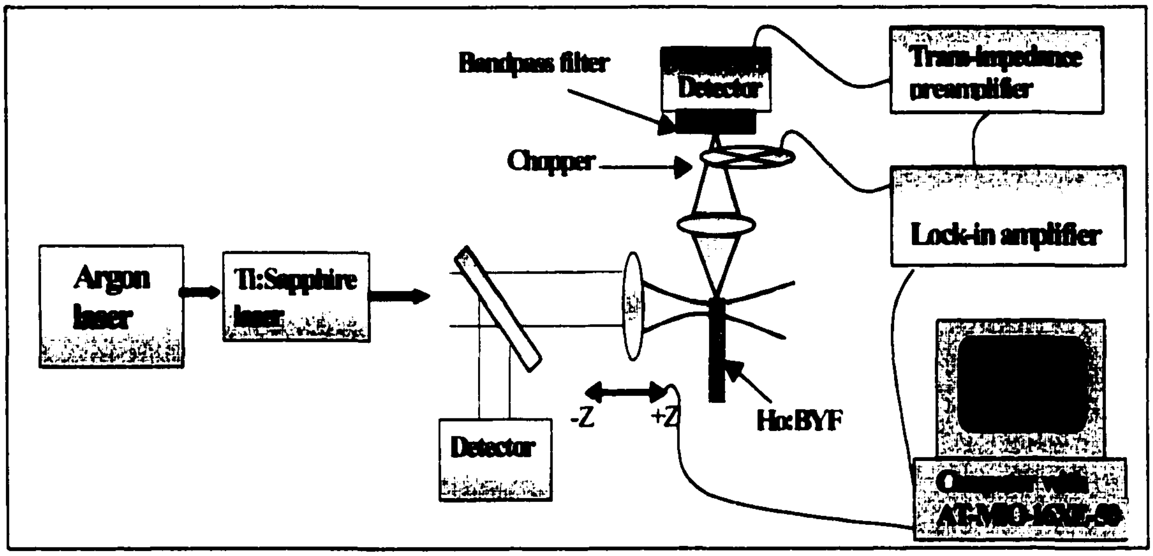

Figure 38. Set-up for Z-scan measurements of fluorescence from Ho^{3+} energy levels.

We found that this method of Z-scan measurements of fluorescence could serve as a direct way of monitoring the population on every single level of Ho^{3+} as a function of pump intensity. By using appropriate detectors and bandpass filters we could selectively monitor the fluorescence at 540 nm, 900 nm, 1200 nm, 2060 nm, 490 nm and 640 nm, representing emission from $^5S_2$, $^5I_5$, $^5I_6$, $^5I_7$, $^5F_3$, and $^5F_5$ levels, respectively to the ground state $^5I_8$. For Z-scan measurements in visible and 900nm, we used silicon detector, while in infrared we used germanium detector and InSb detector. Chopped fluorescence signal was directed to the detector through a bandpass filter. The signal was amplified with trans-impedance preamplifier and then evaluated with the lock-in amplifier, synchronized

Reproduced with permission of the copyright owner. Further reproduction prohibited without permission.

with the reference signal of the chopper. From the lock-in ampiifier, signal was sent to analog input of data acquisition board in computer. The instrument driver for Z-scan measurements of fluorescence was written in graphical programming language Labview.

Generally, Z-scan measurements with 10% and 20% Ho:YLF and Ho:BYF samples show substantial increase in green emission at 540 nm (Figure 39) with the expected quadratic dependence on pump intensity, indicative of two step absorption at 750 nm.

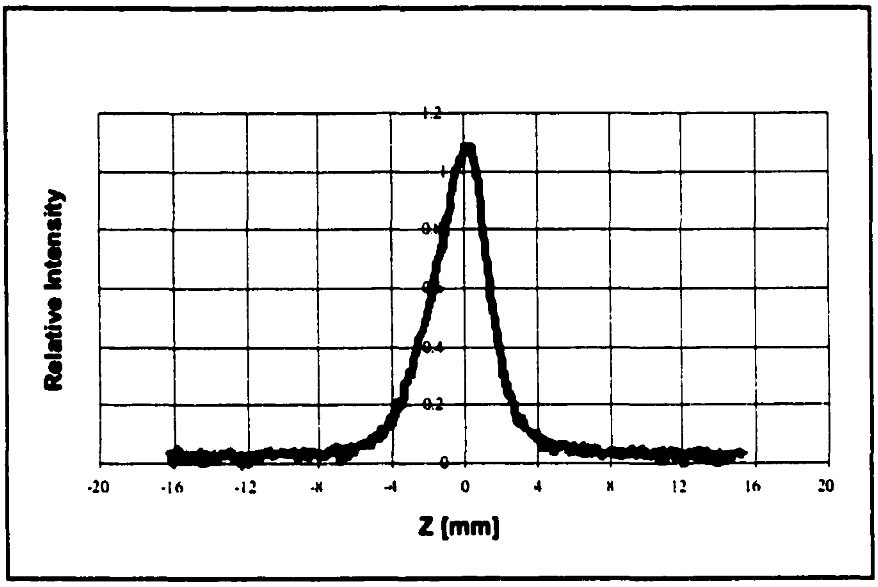

Figure 39. Fluorescence Z-scan curve for emission from $^5S_2$ level at 540 nm in 10% Ho:BYF.

The 900 nm emission ($^5I_5$-$^5I_8$) was very weak in the low doped samples (1%) due to the weak absorption and very low cross relaxation. But with higher Ho^{3+} concentrations 10% and 20% Ho:YLF and Ho:BYF, the cross relaxation rate increases and we can see nonlinear increase of fluorescence efficiency at 900 nm while moving focal plane of the lens to the samples (Figure 40 and 41).

Reproduced with permission of the copyright owner. Further reproduction prohibited without permission.

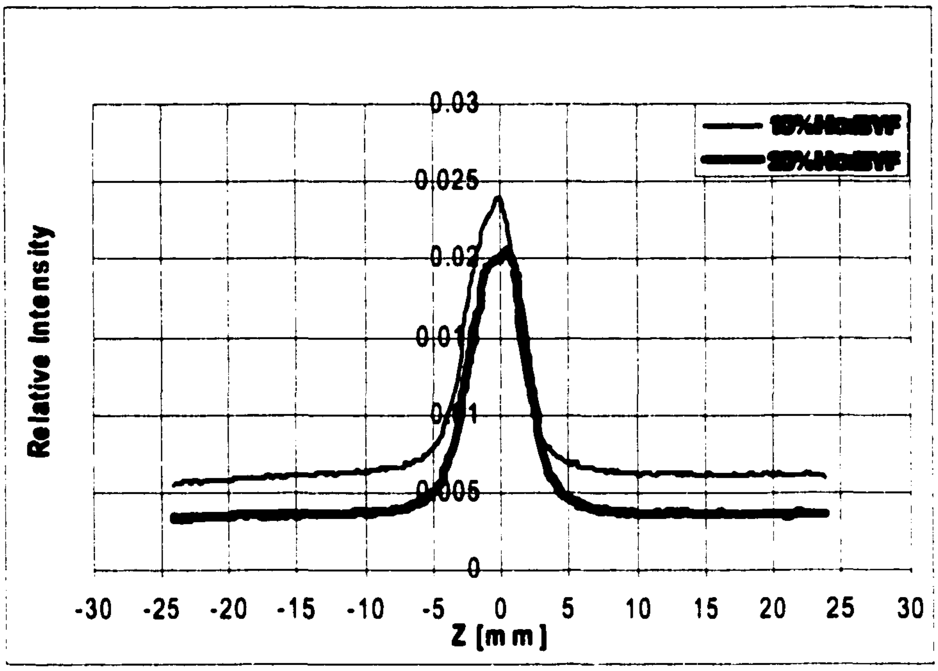

Figure 40. Emission from $^5I_5$ level at 900 nm in Ho:BYF with cw pumping at 750 nm.

The behavior of 1200 nm emission from $^5I_6$ to $^5I_8$ in Ho:BYF was highly surprising. From the model we expected to see the build up of the population on $^5I_6$ with increase of pump intensity due to long lifetime of that level. The sample of 10% Ho:YLF clearly showed the increase of fluorescence signal with pump intensity in a good agreement with the model (Figure 42). Fluorescence from $^5I_6$ in Ho:BYF, however, drops significantly at higher pump intensities (Figure 43). This effect could be caused by upconversion process from $^5I_6$ due to high population on that level. It could be also due to third step absorption at ~ 750 nm, which corresponds to transition from $^5I_6$ to $^5G_6$.

Reproduced with permission of the copyright owner. Further reproduction prohibited without permission.

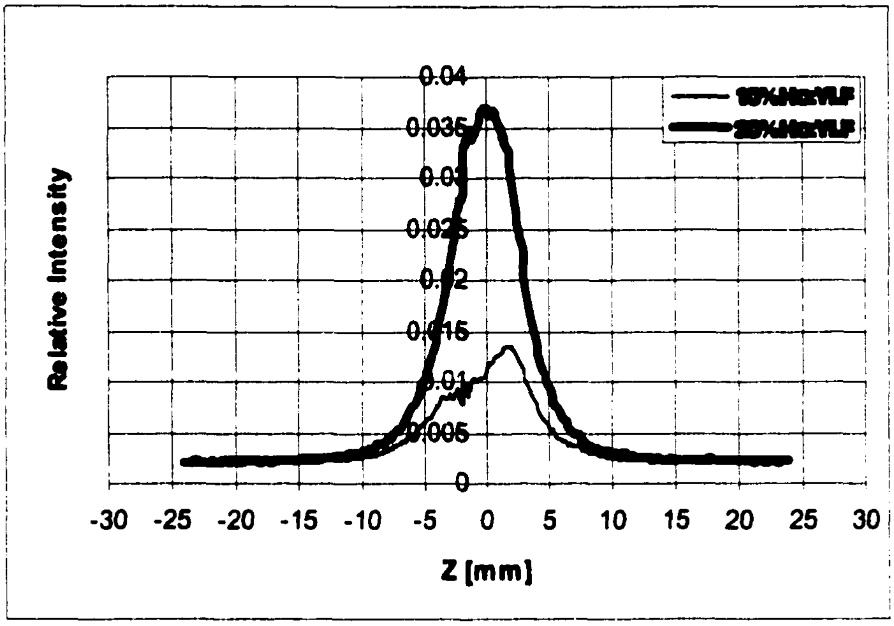

Figure 41. Emission from $^5I_5$ level at 900 nm in Ho:YLF with cw pumping at 750 nm.

To test the later hypothesis, the 490-nm emission was measured for both the 10% and 20% Ho: BYF samples as shown in Figure 44. The increase in blue emission at higher pump intensities indicates that some mechanism is in place elevating photons to the upper $^5G_6$ level with following multiphonon relaxation to $^5F_3$ level, and thus emptying the long lived $^5I_6$ level. We considered these newly observed features to be encouraging, since they provided for the first time an indication that there may be a way of breaking the bottleneck at the $^5I_6$ level in Ho:BYF. Taking into account strong cross relaxation effect $^5F_3$-$^5F_5$ and $^5I_8$-$^5I_7$, observed in emission spectra earlier, we performed the measurements of intensity dependent fluorescence at 640 nm, corresponding to $^5F_5$-$^5I_8$ transition.

Reproduced with permission of the copyright owner. Further reproduction prohibited without permission.

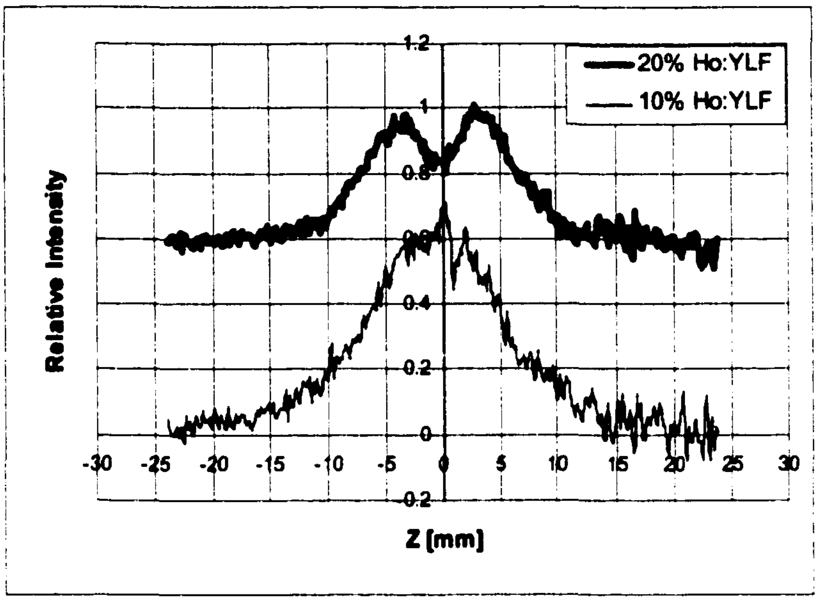

Figure 42. Emission from $^5I_6$ level at 1200 nm in Ho:YLF with cw pumping at 750 nm.

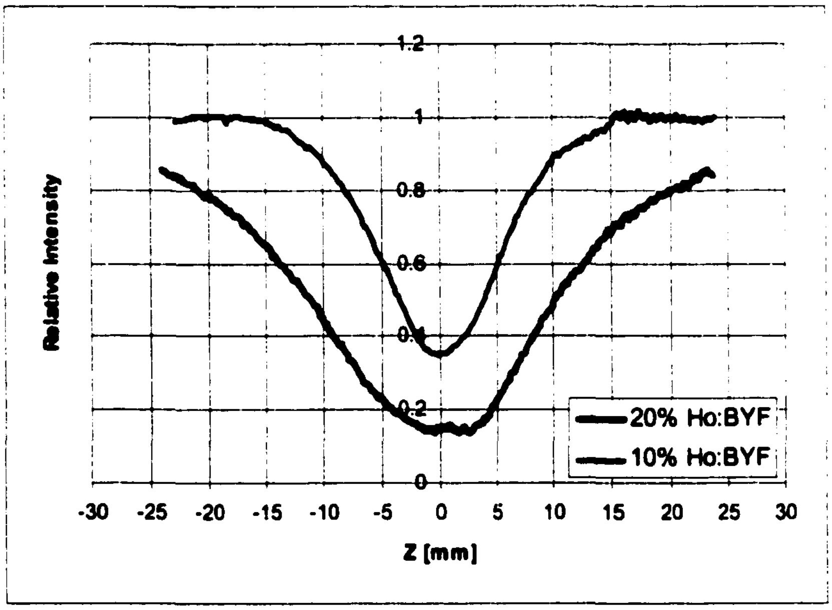

Figure 43. Emission from $^5I_6$ level at 1200 nm in Ho:BYF with cw pumping at 750 nm.

Reproduced with permission of the copyright owner. Further reproduction prohibited without permission.

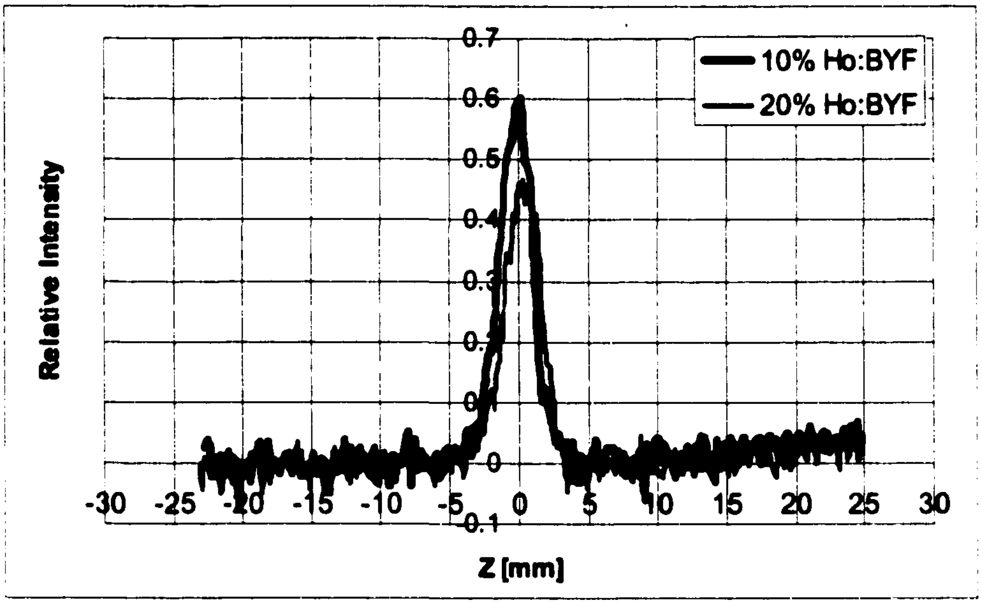

Figure 44. Emission from $^5F_3$ level at 490 nm in Ho:BYF with cw pumping at 750 nm.

Indeed, the nonlinear increase of fluorescence efficiency at 640 nm, was reproducing the profile of 490 nm emission while moving focal plane of the lens to the samples.

The 2060 nm emission ($^5I_7$-$^5I_8$) in both Ho:YLF and Ho:BYF first increases with pump, but then it drops at higher pump intensities (Figure 45 and 46). This was expected from the model: due to long lifetime of $^5I_7$ the population first builds up, but then the 750 nm pumping at high intensities depletes the $^5I_7$ by bringing ions from $^5I_7$ to $^5S_2$.

Reproduced with permission of the copyright owner. Further reproduction prohibited without permission.

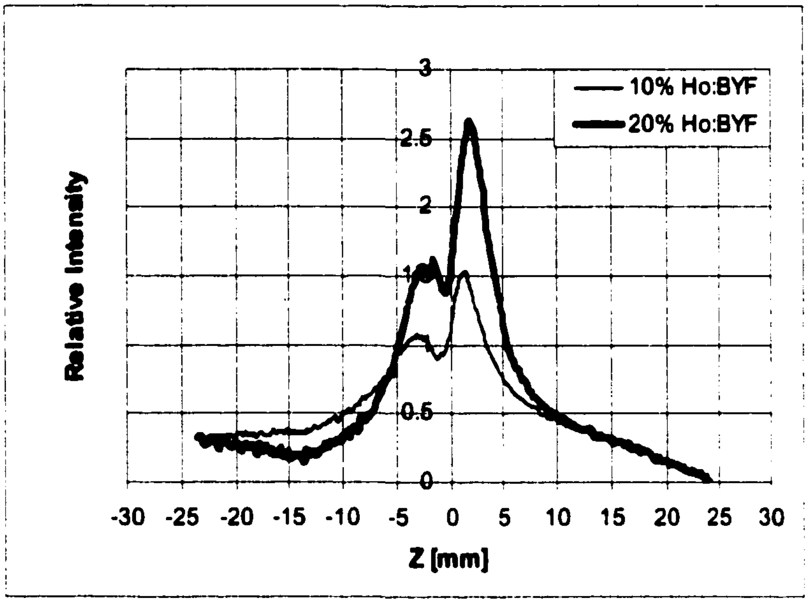

Figure 45. Emission from $^5I_7$ level at 2060 nm in Ho:BYF with cw pumping at 750 nm.

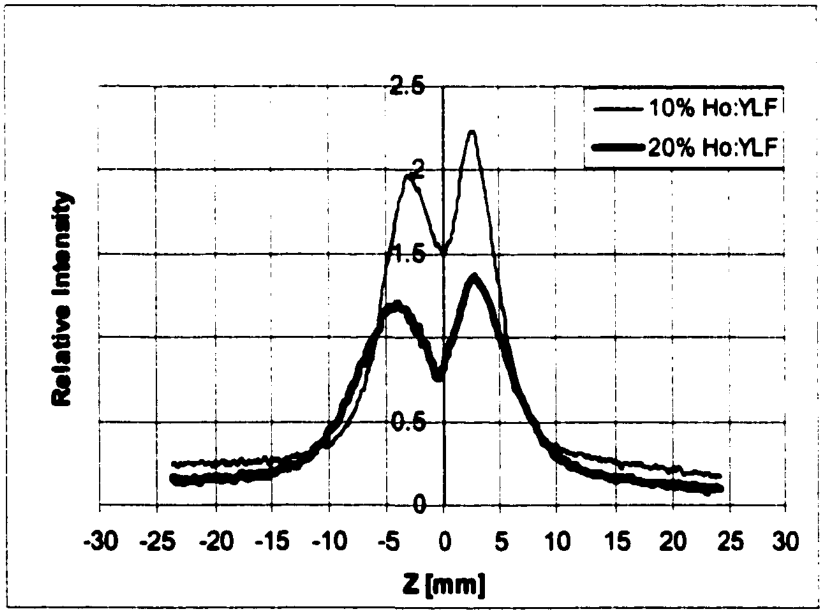

Figure 46. Emission from $^5I_7$ level at 2060 nm in Ho:YLF with cw pumping at 750 nm.

Reproduced with permission of the copyright owner. Further reproduction prohibited without permission.

One comment that applies to all the Z-scan experiments is that results may be somewhat modified if the rise in the temperature of the sample as the pump intensity increases is taken into account. This may affect the magnitude of the relative intensity curves near the center.

5.5. Visible emission spectroscopy of Ho:YLF and Ho:BYF with near IR laser excitation at 750 nm

In addition to Z-scan experiments, we performed measurements of the fluorescence spectra of Ho:YLF and Ho:BYF in visible range under high power pumping at 750 nm. The main purpose of these experiments was evaluation of relative strengths of fluorescence lines from higher energy levels of Ho^{3+} as a measure of populations on that levels, created by cascade cw pumping at 750 nm and energy transfer processes. The experimental set-up was described in the previous section and is shown on Figure 47.

The samples of Ho:YLF and Ho:BYF usually exhibit bright green fluorescence when pumped by Ti:Sapphire laser at ~750 nm. The 20% Ho:BYF sample was, however, glowing white, which was clear indication that in the fluorescence there are other components of spectrum present besides green. Our expectations were confirmed with the measurement of emission spectrum of Ho:BYF. Three strong emission lines in the visible were indeed present in spectrum centered around blue (490 nm), green (540 nm) and red (660 nm), corresponding to transitions from $^5F_3$, $^5S_2$, and $^5F_5$ manifolds to ground state respectively. The emission spectra were corrected for the system response.

Reproduced with permission of the copyright owner. Further reproduction prohibited without permission.

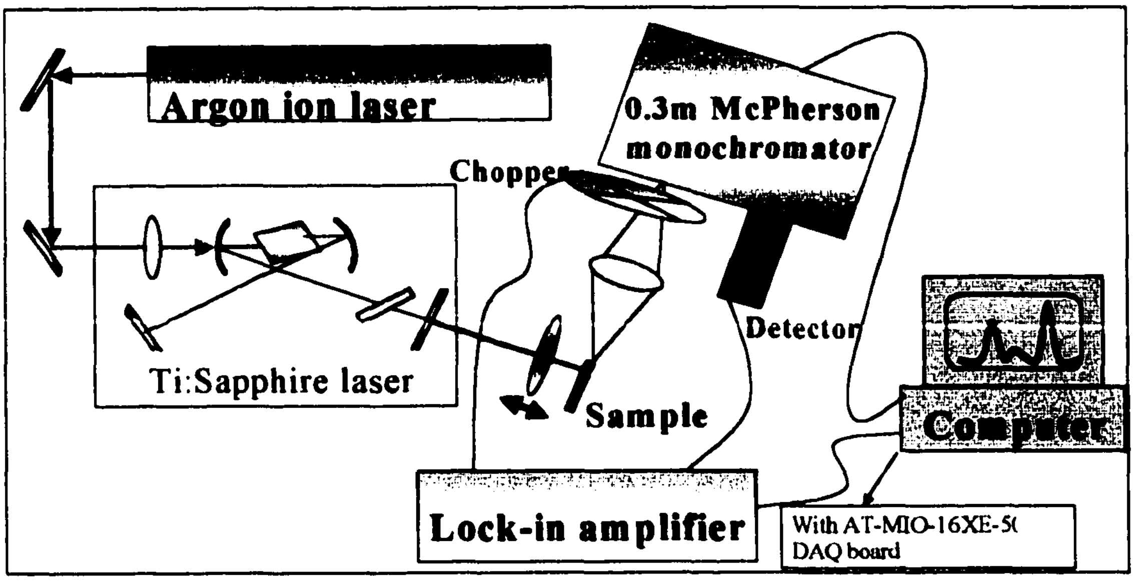

Figure 47. Experimental set-up for emission spectroscopy of Ho:YLF and Ho:BYF with Ti:Sapphire laser excitation at 750 nm

Strong fluorescence in blue (from $^5F_3$ level) was an indication of very efficient energy transfer process from the lower Ho^{3+} manifolds. By correlating these observations with Z-scan measurements we came to conclusion that the feeding of $^5F_3$ could be due to depletion of $^5I_6$. Two mechanisms of population build up on $^5F_3$ were suggested: third step absorption at ~750 nm $^5I_6$-$^5G_6$ followed by multiphonon relaxation from $^5G_6$ to $^5F_3$ or/and upconversion from $^5I_6$. Unlike Er^{3+} energy levels, where there are several resonant matches in energy spacings, and upconversion processes are very efficient [43], Ho^{3+} energy levels do not offer multiple choices of possible upconversion paths from $^5I_6$. Our assumption is that upconversion takes place between $^5I_6$ and $^5G_6$ with the simultaneous transition from $^5S_2$ to $^5I_7$.

Reproduced with permission of the copyright owner. Further reproduction prohibited without permission.

We took emission spectra of 20% Ho:BYF at different pump wavelengths (Figure 48). All fluorescence lines were more intense when the pump wavelength was tuned to the peaks of ground state absorption (GSA) compared to valleys. The strongest peaks, however, were observed at 750.3 nm pump, which probably corresponds to the peak in excited state absorption.

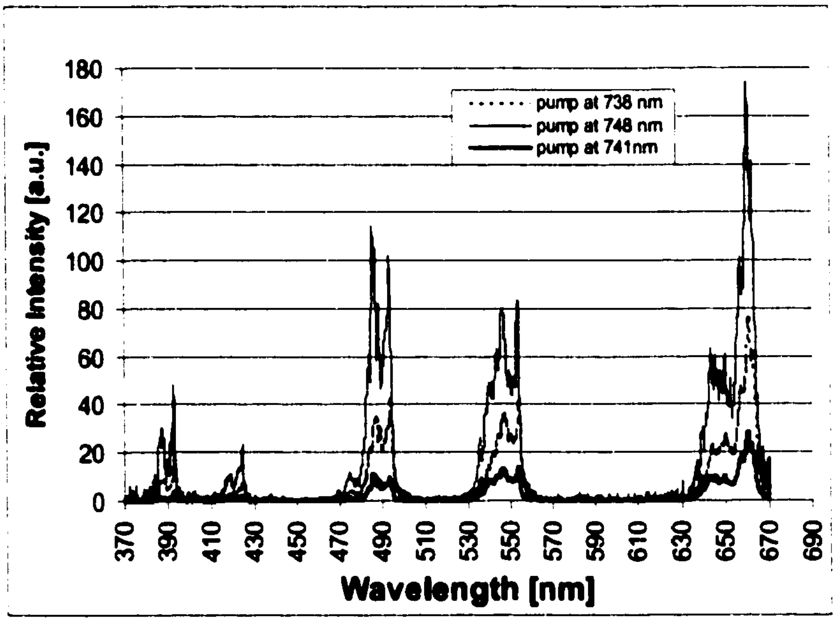

Figure 48. Emission of 20% Ho:BYF at different pump wavelengths of Ti:Sapphire laser.

The wavelength range of excited state absorption ($^5I_7$-$^5S_2$) overlaps quite well with ground state absorption ($^5I_8$-$^5I_4$), while potential third step absorption is expected to be in a slightly shorter wavelength range [36]. We decided to check if upconversion from $^5I_6$ indeed takes place, by pumping Ho^{3+} samples with the Ti:Sapphire laser tuned to the longer wavelength absorption peak in GSA (where the third step absorption is impossible) and monitoring fluorescence in the blue. Indeed, we observed quite strong

Reproduced with permission of the copyright owner. Further reproduction prohibited without permission.

emission at ~490 nm from $^5F_3$ level, which obviously was fed by upconversion from $^5I_6$ level.

The strongest emission line in the visible spectrum of 20% Ho:BYF is at 660 nm, which corresponds to $^5F_5$ - $^5I_8$ transition. As we observed earlier in high concentration Ho:BYF and Ho:YLF, the $^5F_3$ level exhibits strong cross relaxation, which results in an efficient feeding of population from $^5F_3$ to $^5F_5$ manifold, followed by emission from $^5F_5$ to $^5I_8$ at 660 nm. The blue emission at 490 nm from $^5F_3$ is somewhat weaker than red emission. Since the cross relaxation from $^5F_3$ to $^5F_5$ bypasses the $^5S_2$ level, the strength of green emission from $^5S_2$ at 540 nm is mostly determined by the cascade two step absorption at 750 nm, and does not depend on feeding from $^5F_3$ manifold.

Comparison of emission spectra of 20% Ho:BYF and 10% Ho:BYF clearly showed, that blue and red emission in 10% sample is not as efficient as in 20% sample. The strongest emission line in 10% Ho:BYF is green around ~545 nm (Figure 49). Obviously the third order process (which is in this case upconversion from $^5I_6$) elevating ions to levels above $^5S_2$ manifold is not as efficient as in 20% sample.

Fluorescence of Ho:BYF is strongly dependent on orientation of crystallographic axes relative to polarization of pump light. The 10% sample was cut and polished with its faces perpendicular to a-axis, which means that b-axis and [001] direction lie in the plane of crystal's surface, and they are orthogonal to each other. The visible emission lines for polarization parallel to b-axis were weaker than for polarization along the [001] direction (Figure 49). The 20% sample was cut in [010] direction with two extinction directions in the plane of the crystal. Emission lines for 20% of Ho:BYF (Figure 50) were maximal for the polarization of pump light parallel to *z*-axis (or perpenducular to *x*-axis).

Reproduced with permission of the copyright owner. Further reproduction prohibited without permission.

Fluorescence measurements for 10% Ho:YLF showed very strong emission in the green, but very little in the blue (Figure 51). Obviously, there is not much excitation, being elevated above $^5S_2$ level in 10% Ho:YLF. These measurements also confirmed the validity of numerical model for 10% Ho:YLF.

Finally, we measured fluorescence spectra in 20% Ho:BYF for different pump intensities. As we expected the green fluorescence exhibited the quadratic dependence on pump intensity while blue fluorescence showed cubic dependence (Figure 52 and 53).

Comparison of the fluorescence measurements for three different samples, 10% and 20% Ho:BYF and 10% Ho:YLF, provided evidences that 20% Ho:BYF sample could present an interest as a potential material for multiple applications: creation of solid state visible upconversion laser pumped at 750 nm or 3-D color displays.

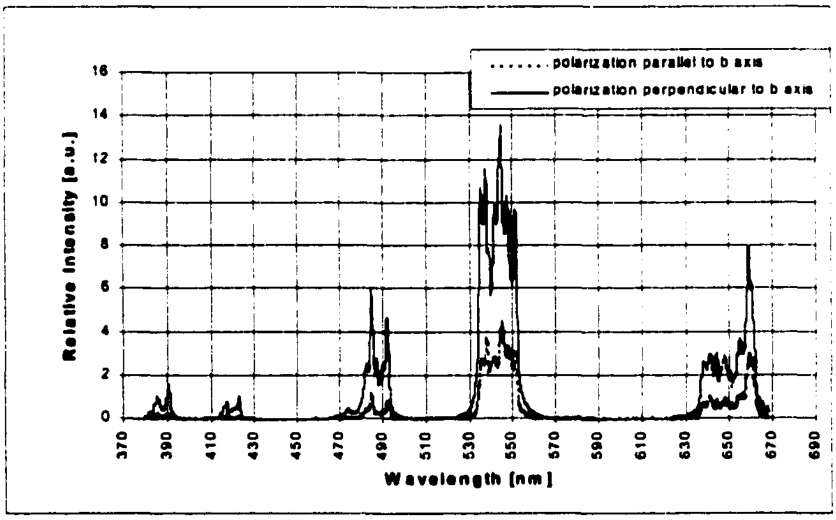

Figure 49. Emission of 10% Ho:BYF with pump at 748.2 nm at two different orientations of crystal relative to pump polarization.

Reproduced with permission of the copyright owner. Further reproduction prohibited without permission.

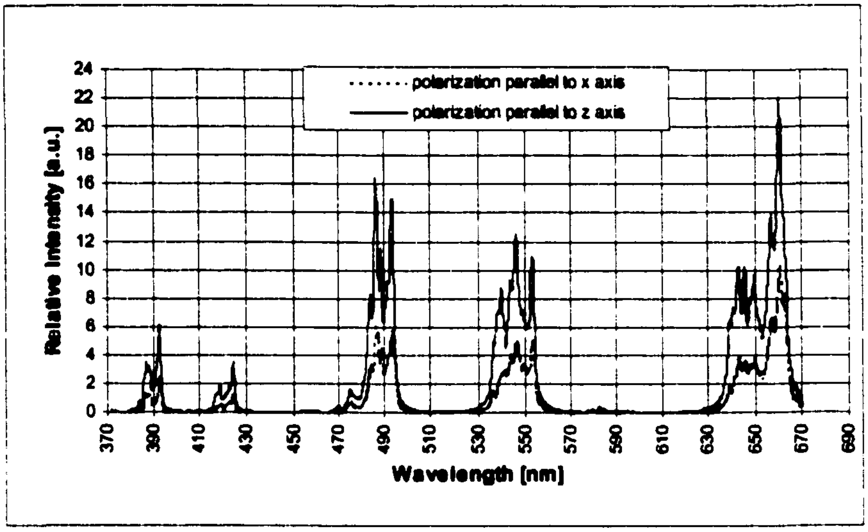

Figure 50. Emission of 20% Ho:BYF at two different orientations of crystal relative to pump polarization with cw pumping at 748 nm.

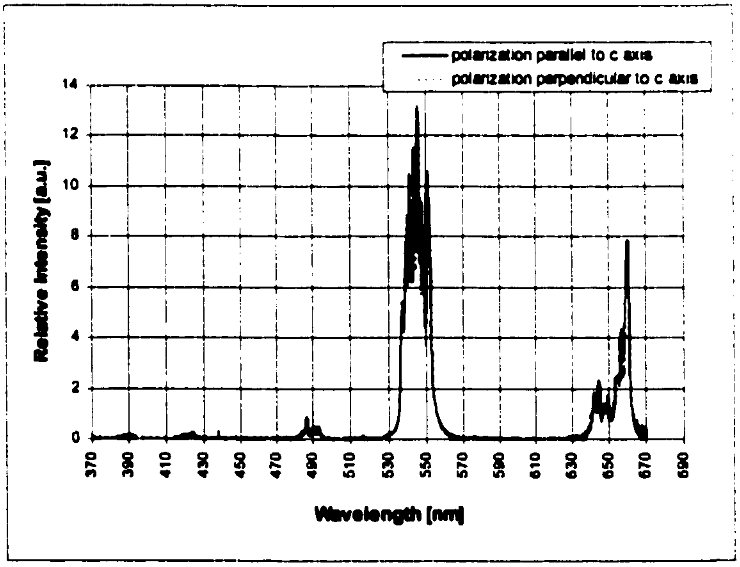

Figure 51. Emission of 10% Ho:BYF with pump at 750.4 nm at two different orientations of crystal relative to pump polarization.

Reproduced with permission of the copyright owner. Further reproduction prohibited without permission.

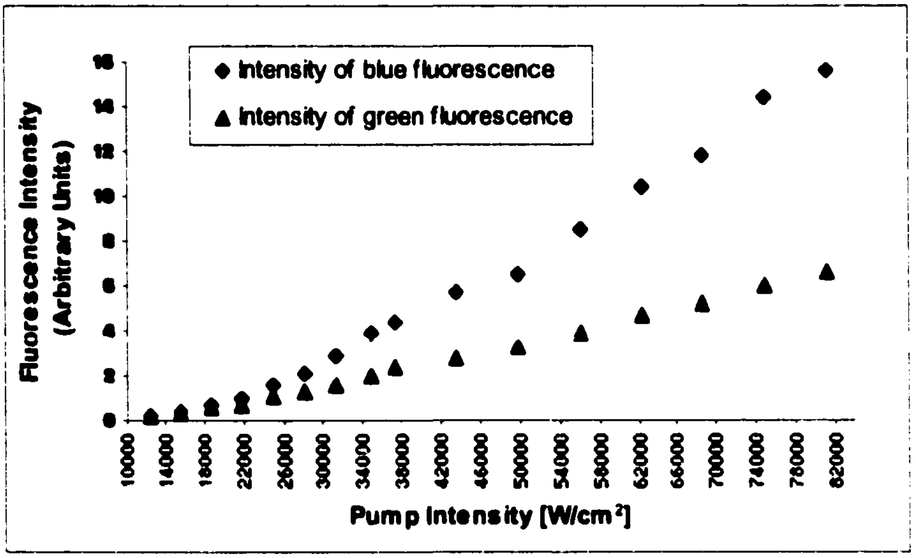

Figure 52. Dependence of blue and green fluorescence in 20% Ho:BYF on pump intensity at 748 nm.

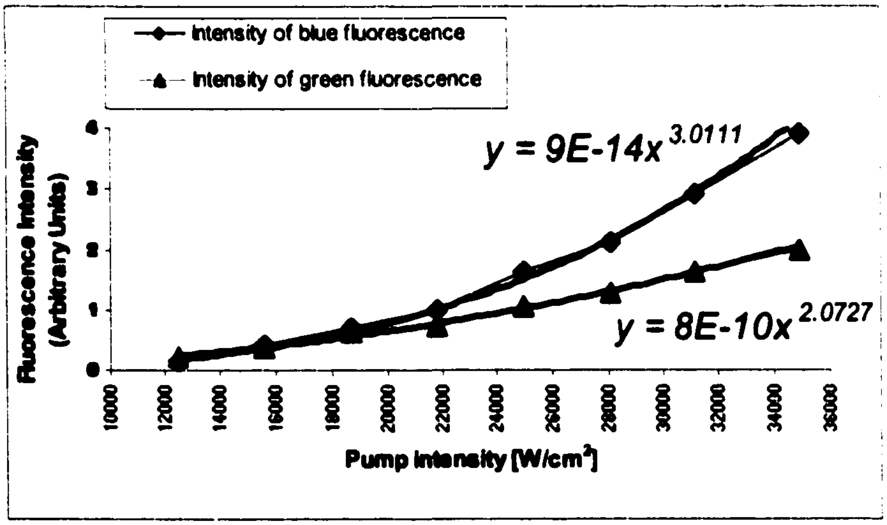

Figure 53. Dependence of blue and green fluorescence in 20% Ho:BYF on pump intensity with power fits. This graph is the first part of the graph above. It shows the dependencies at low pump intensities, before system reaches saturation.

Reproduced with permission of the copyright owner. Further reproduction prohibited without permission.

CHAPTER 6. DIRECT PULSED RESONANT PUMPING SCHEME OF UPPER LEVEL OF THE 3.9 μM TRANSITION IN HO^{3+} DOPED FLUORIDES

6.1. Mid-infrared 3.9 μm laser concept with long pulse pumping

As a third alternative pumping scheme of the 3.9 μm laser, the author suggested the new idea of linear down conversion in Ho^{3+} doped BYF or YLF by direct long pulse resonant pumping of the upper laser level and lasing the 3.9 μm transition (Figure 54). Our recent experimental observations and theoretical calculations provided evidences that the direct resonant pumping of the upper level $^5I_5$ of the 3.9 μm transition will allow achieving laser action with higher efficiency than in the configuration with 532 nm pump. Both BYF and YLF doped with Ho^{3+} ions exhibit ground state absorption at 890 nm to the metastable $^5I_5$ level (Figure 9 and 10). The $^5I_5$ level serves as the upper laser level for the 3.9 μm $^5I_5$– $^5I_6$ laser transition.

As it was already discussed in the previous sections, the upper laser level $^5I_5$ level has a rather short lifetime (50 μs in Ho:BYF and 20 μs in Ho:YLF) compared to the long lifetime of the terminal laser level (5450 μs in Ho:BYF and 2050 μs in Ho:YLF), which, in general, creates conditions unfavorable for lasing. The experimental measurements of dynamics of build up and decay rates of the populations

Reproduced with permission of the copyright owner. Further reproduction prohibited without permission.

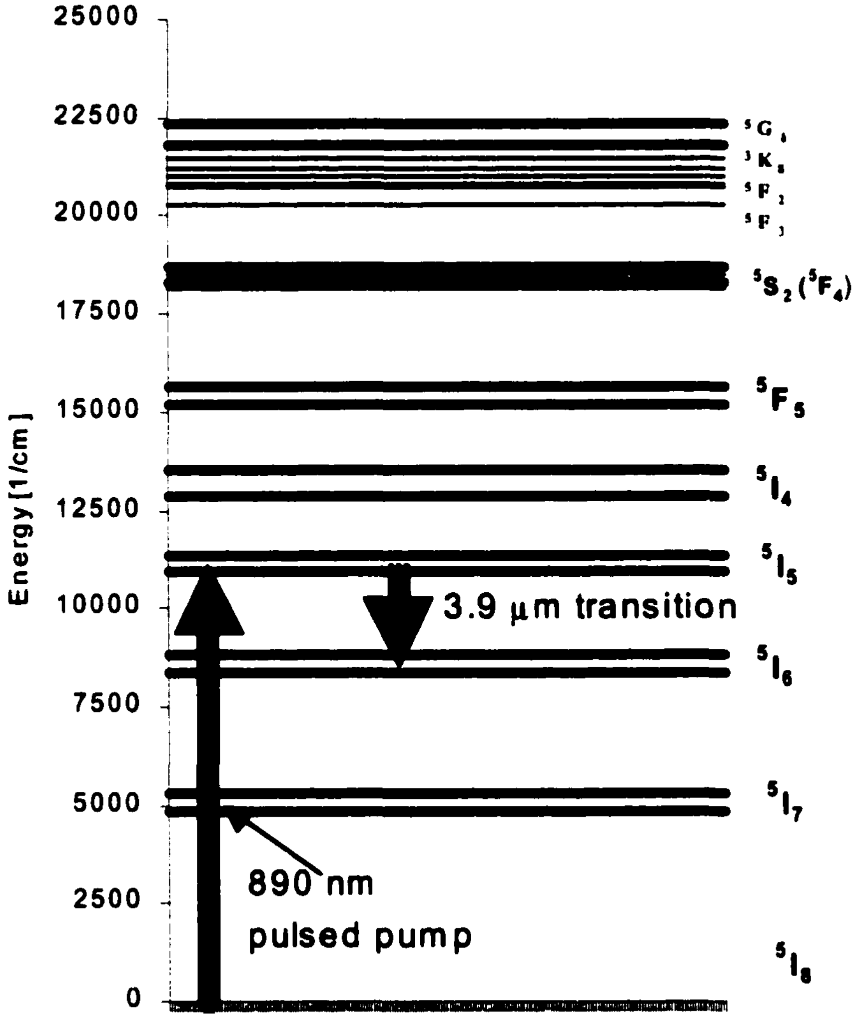

Figure 54. Direct pulsed resonant pumping scheme of upper level of 3.9 μm mid-IR laser transition in Ho^{3+} doped fluorides.

Reproduced with permission of the copyright owner. Further reproduction prohibited without permission.

on Ho^{3+} levels upon direct pulsed pumping of $^5I_5$ level, have shown however, that the inversion of population between the levels $^5I_5$ and $^5I_6$ can be achieved for the initial interval of time comparable with the lifetime of $^5I_5$ level. Our numerical simulations of theoretical model of the system have confirmed the same conclusions. For an efficient 3.9 μm laser it was, therefore, necessary to pump Ho^{3+} ions with a 890 nm laser pulse of comparable length, 10 to 50 μs.

As we mentioned before, linear down-converters are of practical interest when pumped by efficient, well-developed sources. We have demonstrated 1-1.5 J 50μs long pulse Cr:LiSAF laser tuned to 890 nm (described in Chapter 7) for the direct resonant pumping of the upper level $^5I_5$ of the 3.9 μm transition.

A series of theoretical calculations and experimental measurements was performed in order to determine the optimal conditions for achieving the 3.9 μm laser emission from holmium-doped fluoride crystals Ho:BYF and Ho:YLF upon pumping with long pulses at 980 nm.

6.2. Numerical modeling of the direct resonant pulsed pumping scheme of the upper level of the 3.9 μm laser

Numerical modeling of 3.9 μm laser operation with direct pumping of the upper laser level is based on the energy level diagram of Ho^{3+}, shown on Figure 54. The goal of our calculations was to determine under what conditions a population inversion could be achieved between the $^5I_5$ and $^5I_6$ levels using a long pulse excitation at 890 nm.

A system of 4 coupled differential rate equations was used to describe the temporal development of the populations of Ho^{3+} energy levels $^5I_8$, $^5I_7$, $^5I_6$ and $^5I_5$.

Reproduced with permission of the copyright owner. Further reproduction prohibited without permission.

In the model, we assumed that pumping at 890 nm results in ground state absorption from $^5I_8$ to $^5I_5$ with cross section $\sigma_{518\text{-}515} = 3.85 \cdot 10^{-22}\text{cm}^2$. There is also some excited state absorption of 890 nm from $^5I_5$ to $^5G_6$, however, the amount of the ions elevated above the $^5I_5$ level was assumed to be negligibly small compared to population circulating between the $^5I_8$ and $^5I_5$ levels. The resonant cross relaxation process involving the $^5I_8$ and $^5S_2$ manifolds, discussed in the previous sections, was not taken into account due to the same assumption of low population of $^5S_2$ level.

The system of equations was solved for the case of threshold for 3.9 μm lasing, without taking into account stimulated emission and stimulated absorption between the levels $^5I_5$ and $^5I_6$. The population dynamics of Ho^{3+} ions in laser crystal upon pumping with the long laser pulse at 890 nm can be described by the following system of linear differential equations:

$$\begin{aligned}
&N_{^5I_8} = N_0 - N_{^5I_7} - N_{^5I_6} - N_{^5I_5} \\
&\frac{dN_{^5I_7}}{dt} = -\frac{N_{^5I_7}}{\tau_{^5I_7}} + \left(1 - \beta_{^5I_5-^5I_6}\right)\frac{N_{^5I_5}}{\tau_{^5I_5}} + \beta_{^5I_6-^5I_7}\frac{N_{^5I_6}}{\tau_{^5I_6}} \\
&\frac{dN_{^5I_6}}{dt} = -\frac{N_{^5I_6}}{\tau_{^5I_6}} + \beta_{^5I_5-^5I_6}\frac{N_{^5I_5}}{\tau_{^5I_5}} \\
&\frac{dN_{^5I_5}}{dt} = \sigma_{^5I_8-^5I_5} R_{^5I_8-^5I_5} N_{^5I_8} - \frac{N_{^5I_5}}{\tau_{^5I_5}}
\end{aligned} \qquad (6.1)$$

where, N_0 is the concentration of Ho^{3+} ions in the crystal; τ are the lifetimes of corresponding levels; $\sigma_{5I8\rightarrow 5I5}$ is the cross sections of ground state absorption; $R_{5I8\rightarrow 5I5}$

Reproduced with permission of the copyright owner. Further reproduction prohibited without permission.

– the number of pump photons per unit area per unit time that excite Ho^{3+} ions to $^5I_5$ level during the laser pulse; β are the feeding efficiencies to corresponding levels from the levels above them. The assumption was made that the pump is applied in the form of square pulses, and the calculations were carried out for different repetition rates. The initial population of the ground state was calculated taking into account the concentration of Ho^{3+} ions.

The time dependencies of energy level populations were calculated using the forward Euler procedure [41], similar to one used in the modeling of cw pumping at 750 nm, with the time increment equal to the smallest time constant in the rate equations. The steady-state solutions for different pump conditions could be found not only numerically but also analytically. However, they were of little importance in this particular scheme, since the creation of the inversion of population between the levels $^5I_5$ and $^5I_6$ is possible only within the lifetime of $^5I_5$ matched by the duration of the pump pulse. After the pump pulse is turned off, the population builds up on the two lower energy manifolds $^5I_6$ and $^5I_7$, which then decay with their respective relaxation rates, before the next pump pulse arrives.

In the starting model, we performed numerical simulations for low concentration (1%) of Ho^{3+} ions doped in YLF and BYF. Our experimental measurements indicated that in low concentration samples there was negligible if any influence of nonlinear processes, such as cross relaxation or upconversion effects from/to $^5I_5$ level, which significantly simplified the calculations. In the reference [38], the author reports no measurable change in the lifetime of the $^5I_5$ manifold on Ho:YLF for concentrations in the range of 1% to 10%, which implies that the $^5I_5$ level does not cross relax efficiently in

Reproduced with permission of the copyright owner. Further reproduction prohibited without permission.

Ho:YLF. The reported expected ratio of upconversion parameter to cross relaxation parameter is 0.01 for $^5I_7$ - $^5I_8$ and $^5I_7$ - $^5I_5$ upconversion in Ho:YLF [38], which rules out the upconversion process too. Similar results should be expected in BYF as the multiphonon relaxation rates in this material are smaller than in YLF for similar energy gaps.

We did not intend to use the low concentration samples for actual laser experiments due to weak ground state absorption at 890 nm, however, the comparison of the numerical model results and experimentally measured temporal profiles of populations of participating energy levels in low concentration samples allowed us to check the validity of the model and its applicability for higher concentrations samples. Examples of the solutions compared with experimentally observed waveforms will be described below.

The calculations for the system (6.1) show that the population of the $^5I_5$ manifold starts building up (to a value determined by the pump rate and duration of the pump pulse) as soon as the pump pulse is turned on (Figure 55). For example, according to calculations with 50 μs long 12 mJ pump laser pulse at 890 nm, the population of $6.7 \cdot 10^{16}$ 1/cm^3 can be achieved on $^5I_5$ manifold in 1% Ho:BYF. When the pump pulse is turned off, the $^5I_5$ population decays with its characteristic decay rate. The significant part of the population in $^5I_5$ relaxes to $^5I_6$ level and is characterized by the branching ratio $\beta_{5I5\text{-}5I6}$. Meanwhile, the population of the $^5I_6$ level builds up in time determined by the decay from $^5I_5$ level, achieving its maximum at about 400 μs, then it decays with its lifetime of 5.45

Reproduced with permission of the copyright owner. Further reproduction prohibited without permission.

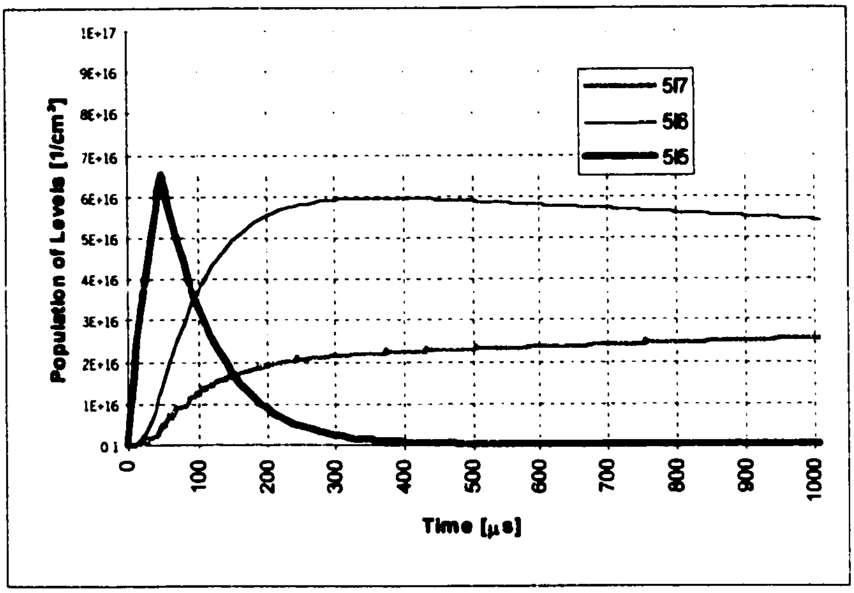

Figure 55. The results of model calculations for direct pulsed pumping of $^5I_5$ level in 1% Ho:BYF with 12 mJ pump pulses at 890 nm.

ms. Similar behavior of the $^5I_6$ level was observed in the experimental measurements of the temporal profiles of the build up and decay of fluorescence at 1200 nm, which corresponds to emission from $^5I_6$ to ground state $^5I_8$. Figure 56 demonstrates the comparison between the experimentally measured fluorescence transient from $^5I_6$ and the theoretically calculated build-up and decay of population on $^5I_6$ level.

The increase of population of $^5I_7$ clearly demonstrates contribution of two components: fast and slow. The fast build up of $^5I_7$ population is due to feeding from $^5I_5$ level with the branching ratio $1-\beta_{5I5\text{-}5I6}$, while the slow component is due to feeding from $^5I_6$ level with the branching ratio $\beta_{5I6\text{-}5I7}$. The branching ratios $\beta_{5I5\text{-}5I6}$ and $\beta_{5I6\text{-}5I7}$ were varied as input parameters in the model until the best fit of theory to experimentally

Reproduced with permission of the copyright owner. Further reproduction prohibited without permission.

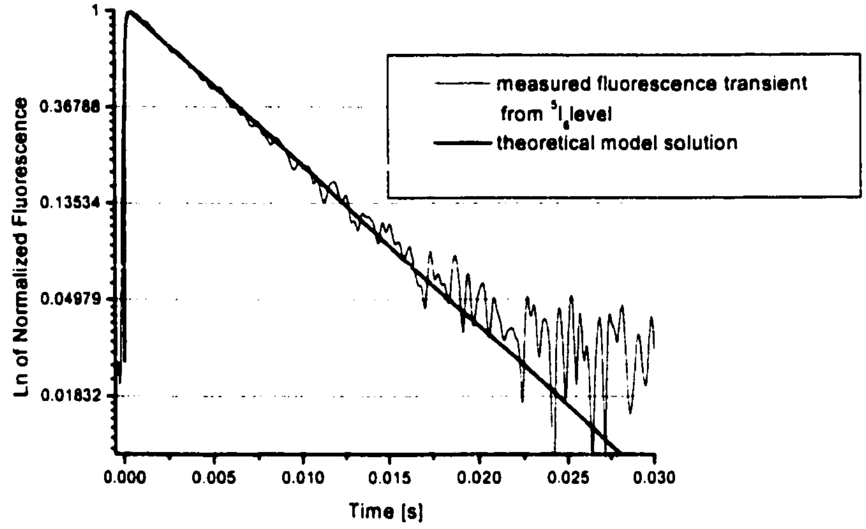

Figure 56. Experimentally measured fluorescent transient from $^5I_6$ level in 1% Ho:BYF and theoretically calculated temporal profile of population on $^5I_6$.

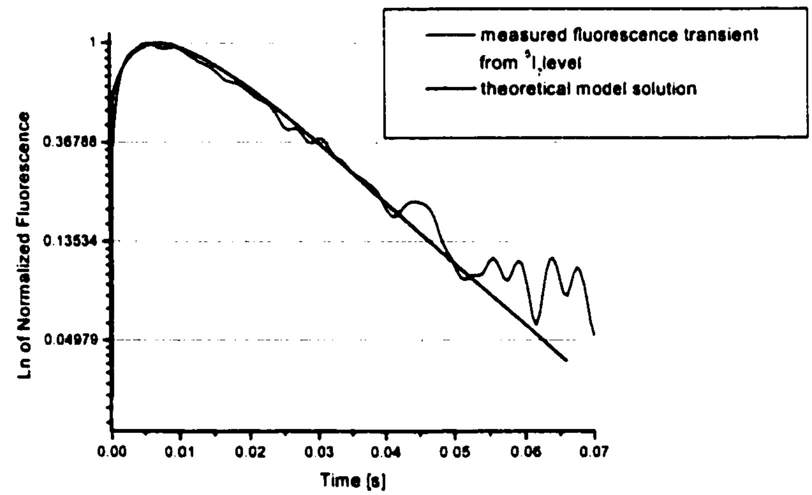

Figure 57. Experimentally measured fluorescent transient from $^5I_7$ level in 1% Ho:BYF and theoretically calculated temporal profile of population on $^5I_7$.

Reproduced with permission of the copyright owner. Further reproduction prohibited without permission.

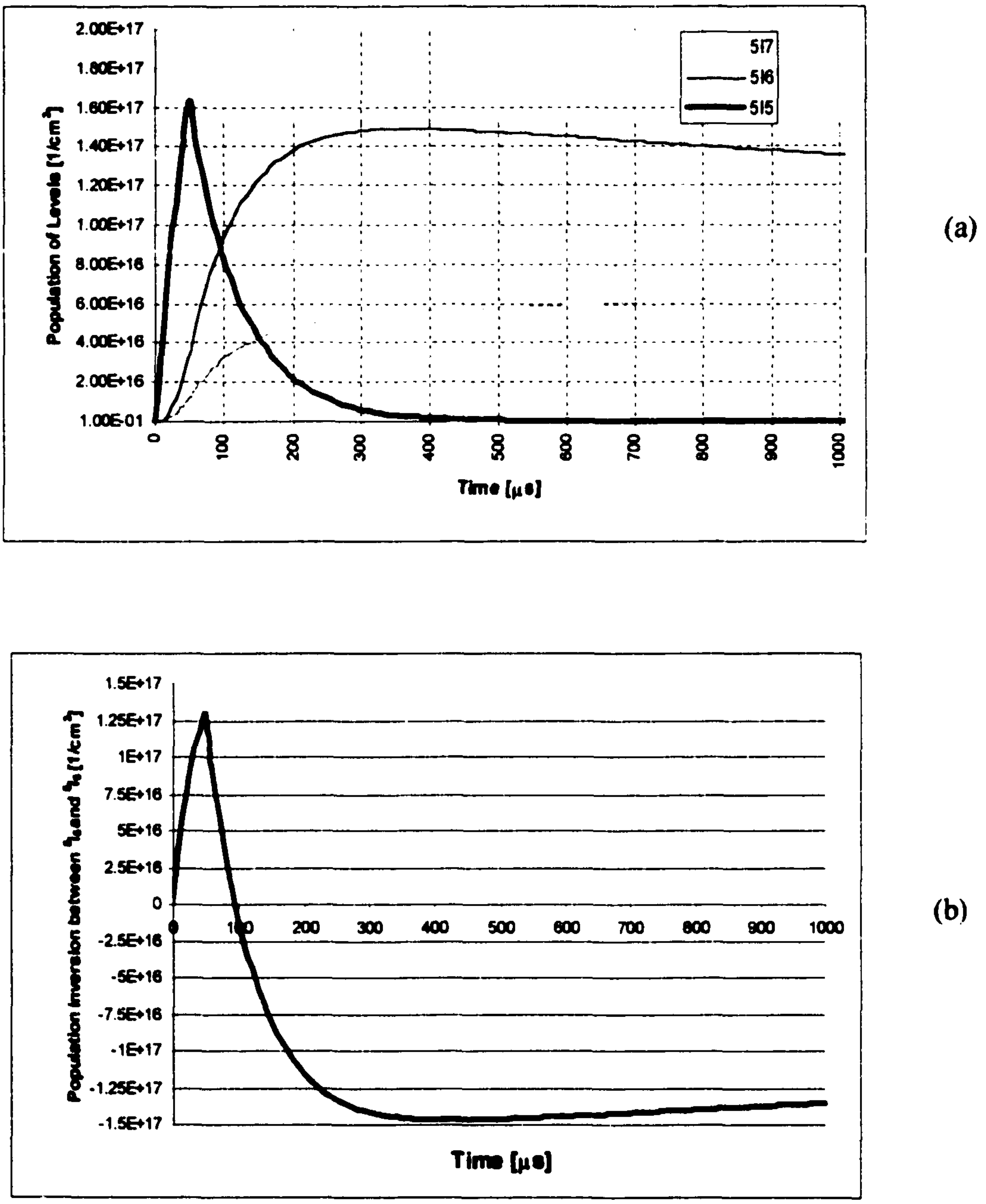

Figure 58. Results of model calculations for the direct pulsed pumping of upper level of the 3.9 μm laser transition in 10% Ho:BYF at pump energy of 3 mJ: (a) populations of levels $^5I_5$, $^5I_6$, $^5I_7$; (b) inversion of population between $^5I_5$ and $^5I_6$ levels.

Reproduced with permission of the copyright owner. Further reproduction prohibited without permission.

observed fluorescence transients was achieved. With 12 mJ pump pulse in 1% Ho:BYF, the model predicts that the $^5I_7$ level population reaches its maximum $3.7\cdot10^{16}$ $1/cm^3$ at about 7.2 ms and then decays with its lifetime of 17 ms. The results of model calcultion are in a good agreement with the experimental measurements of the temporal profiles of the build up and decay of fluorescence at 2060 nm, which corresponds to emission from $^5I_7$ to ground state $^5I_8$ (Figure 57).

Next, the calculations of the population dynamics in 10% Ho:BYF upon pumping with 50 μs long pulses at 890 nm, were performed. The populations of $^5I_5$, $^5I_6$, and $^5I_7$ levels were evaluated for different pump energies. The laser action at 3.9 μm in 10% Ho:BYF, described in the next section, was achieved with an absorbed pump energy threshold of 3 mJ. By using this energy as an input parameter for the theoretical model we obtained the following results: the maximum population achieved on the upper level $^5I_5$ of 3.9 μm laser by the end of the 50 μs long pump pulse was $1.63\cdot10^{17}$ $1/cm^3$ (Figure 58(a)), with the corresponding population inversion between $^5I_5$ and $^5I_6$ $\Delta N = 1.29\cdot10^{17}$ $1/cm^3$ (Figure 58(b)). This value of the inversion of population along with the threshold condition allows to estimate the order of the magnitude of the stimulated emission cross section of $^5I_5$ - $^5I_6$ transition $\sigma_{5I5\rightarrow5I6}$. The threshold for laser oscillation is determined by the requirement that the round-trip gain in the cavity exceed 1. If one considers only mirror losses, then the threshold condition is:

$$R_1 R_2 \exp(\sigma_{5I5\rightarrow5I6}\ \Delta N_{5I5\rightarrow5I6}\, 2L) \geq 1 \qquad (6.2)$$

or

Reproduced with permission of the copyright owner. Further reproduction prohibited without permission.

$$\gamma \geq 1/2L \ln(1/R_1R_2) \tag{6.3}$$

where γ is a small-signal gain coefficient and can be calculated as:

$$\gamma = \sigma_{5I5\rightarrow5I6}\, \Delta N_{5I5\rightarrow5I6} \tag{6.4}$$

Knowing the reflectivities of the actual mirrors used in the laser experiment (see Chapter 6.4), $R_1 = 0.998$ and $R_2 = 0.95$, and the length of the 10% Ho:BYF laser crystal, $L = 2$ cm, we can calculate that for achieving laser threshold the small-signal gain coefficient should satisfy the following condition: $\gamma \geq 0.01268\ cm^{-1}$. This, along with Eq. (6.4), allows to estimate the stimulated emission cross section of $^5I_5$ - $^5I_6$ 3.9 μm transition as $\sigma_{5I5\rightarrow5I6} \geq 9.8\cdot10^{-20}$ cm^2. Then, the small signal power gain per round trip given by

$$G = exp\,(\sigma_{5I5\rightarrow5I6}\ \Delta N_{5I5\rightarrow5I6}\, 2L) \tag{6.5}$$

at threshold is greater than unity.

The calculations of population inversion created between $^5I_5$ and $^5I_6$ levels at higher energies have shown that $\Delta N_{5I5\rightarrow5I6}$ increases linearly with absorbed pump energy. For example, at 250 mJ of absorbed pump energy $\Delta N_{5I5\rightarrow5I6} = 1.06\cdot10^{19}$ 1/cm^3, and at 750 mJ of absorbed pump energy $\Delta N_{5I5\rightarrow5I6} = 3.15\cdot10^{19}$ 1/cm^3 (Figure 59).

Reproduced with permission of the copyright owner. Further reproduction prohibited without permission.

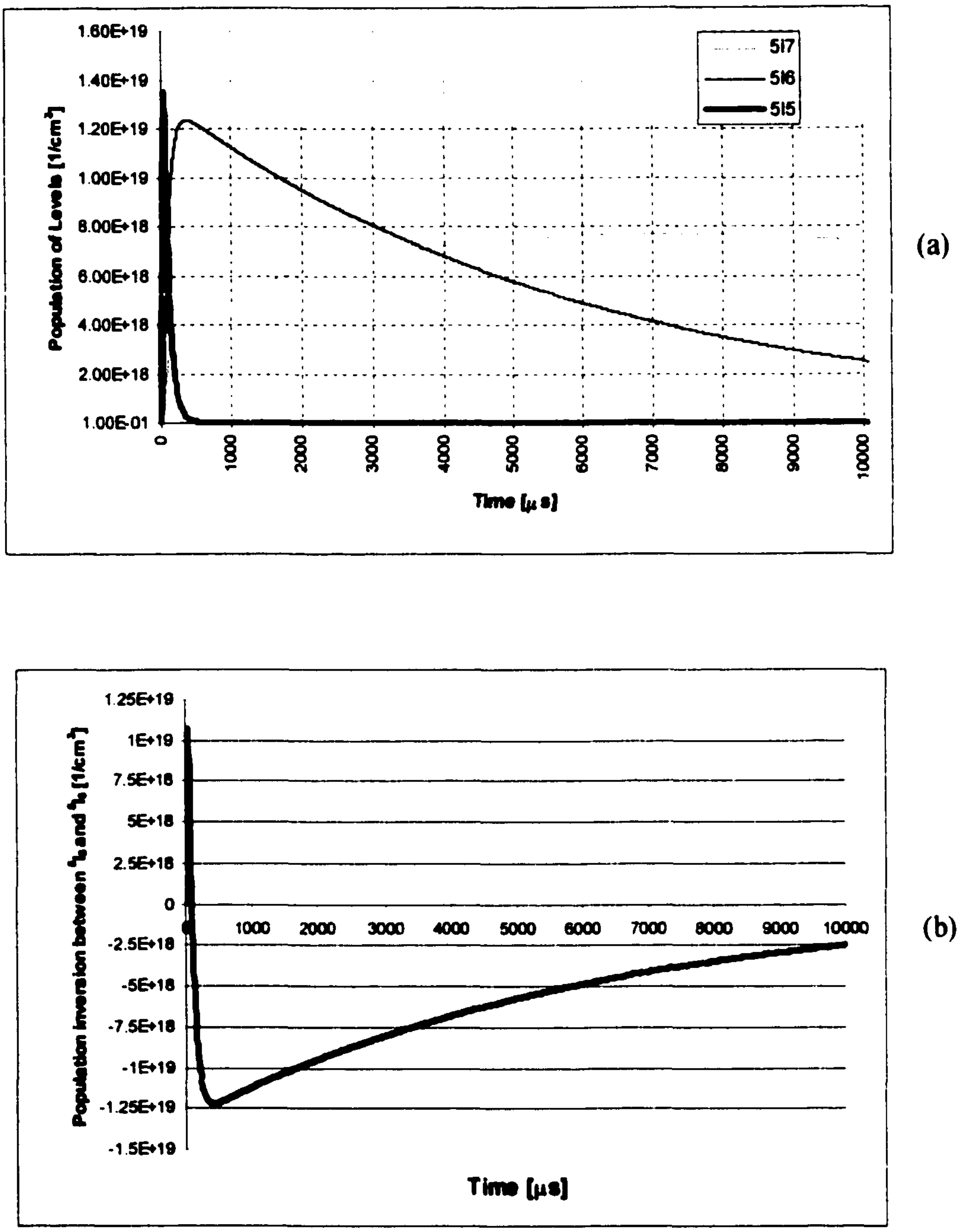

Figure 59. Results of model calculations for the direct pulsed pumping of upper level of 3.9 μm laser transition in 10% Ho:BYF at pump energy of 250 mJ: (a) populations of levels $^5I_5$, $^5I_6$, $^5I_7$; (b) inversion of population between $^5I_5$ and $^5I_6$ levels.

Reproduced with permission of the copyright owner. Further reproduction prohibited without permission.

Next, the model calculations were carried out for the 20% Ho:BYF 3.9 μm laser. The population deposited by the pump pulse on the upper $^5I_5$ level of the 3.9 μm transition in 20% Ho:BYF was factor of two higher than in the case with 10% Ho:BYF at given pump energies. This can be explained by the following formula:

$$dN_{5I5}/dt\ (\text{due to pumping}) = \sigma_{5I8\rightarrow 5I5}\, R_{\,5I8\rightarrow 5I5}\, N_{5I8} \qquad (6.6)$$

where N_{5I8} is the ground level population (or concentration of Ho^{3+} ions) which is two times higher in 20% than in 10% Ho:BYF.

6.3. Measurements of temporal build up and decay of populations of Ho:YLF and Ho:BYF energy levels with pulsed laser excitation at 890 nm

Prior to the actual development of the 3.9 μm laser with the direct resonant pumping of the upper level $^5I_5$ of laser transition, we performed series of experimental measurements of population dynamics on $^5I_6$ and $^5I_7$ energy levels in Ho:BYF and Ho:YLF upon pumping with 50 μs long pulses at 890 nm. Our experimental apparatus is shown in Figure 60. The pulse from the laser is incident on the sample mounted on an adjustable stage. In the experiments with high intensity excitation, the pump beam was focused on the sample with 10 cm focal length lens. The fluorescence from the crystal was collected by a lens and focused onto InAs detector cooled with liquid N_2. In order to selectively monitor the fluorescence from a particular manifold, a bandpass filter was mounted in front of the detector. The signal from the detector was amplified by a broad band trans-impedance preamplifier and acquired with Tektronix digital oscilloscope,

Reproduced with permission of the copyright owner. Further reproduction prohibited without permission.

which collected and averaged a number of waveforms to produce a transient. The detector was biased so that its response time was much faster than the lifetime being measured.

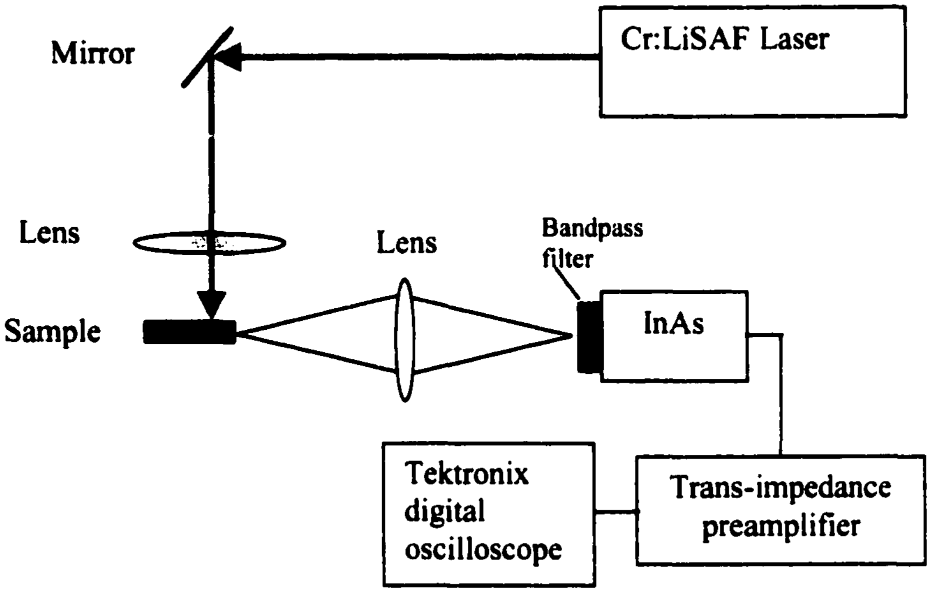

Figure 60. Experimental apparatus for measuremens of fluorescence transients from 5I6 and 5I7 levels in Ho^{3+} doped fluorides.

The 10 mJ 50 μs pulses from Cr:LiSAF laser at 890 nm were used for excitation of Ho^{3+} ions from ground state into $^5I_5$ level. The 1200 nm bandpass filter mounted in front of the detector was used for monitoring the fluorescence transient from $^5I_6$ level to ground state, while 2060 nm filter was used for the measurements of fluorescence transient from $^5I_7$ level to ground state. The fluorescence transients from $^5I_5$ level were not measured in our experiments, since the duration of the pump pulse (50 μs) is comparable to short lifetime of the $^5I_5$ level. For accurate measurements of the temporal development of fluorescence from $^5I_5$ level we would need short pulse excitation at 890 nm, which can be achieved by Q-switching of our Cr:LiSAF laser. Unfortunately, the equipment for Q-switching was not available at the time of our experiments. The lifetime

Reproduced with permission of the copyright owner. Further reproduction prohibited without permission.

of $^5I_5$ level can be estimated from the initial build up and decay of fluorescence from $^5I_6$ level. The time development of $^5I_6$ - $^5I_8$ fluorescence at 1200 nm after pulsed excitation of $^5I_5$ level is proportional to the difference of two exponential decays:

$$e^{-t/\tau_1} - e^{-t/\tau_2}$$

where τ_1 is lifetime of $^5I_5$ level and τ_2 is lifetime of $^5I_6$ level.

This curve has a maximum at:

$$t_{\max} = \frac{\ln \frac{1}{\tau_1} - \ln \frac{1}{\tau_2}}{\frac{1}{\tau_1} - \frac{1}{\tau_{21}}}$$

which can be experimentally measured. Thus, with τ_2 and t_{max} measured, τ_1 can be deduced. The broadness of the maximum around t_{max} makes a precise determination of the t_{max} difficult, but for the purpose of this study, it is more important to estimate the order-of-magnitude of decay changes with concentration and over a wide range of peak intensities. In our experiments, the unfocused pump beam at 890 nm delivered the peak intensity of 0.1 MW/cm^2 and, with focused pump, peak intensity of 40 MW/cm^2 was achieved.

The data generated in the experiment were analyzed in several manners. The temporal profiles were used for the determination of the build-up and decay rates of fluorescence from $^5I_6$ and $^5I_7$ levels for different samples pumped under certain

Reproduced with permission of the copyright owner. Further reproduction prohibited without permission.

conditions. Normalized fluorescence transients were fitted with the numerical solutions of rate equations describing the system.

The temporal build up and decay of fluorescence from $^5I_6$ level at 1200 nm in Ho:BYF with low intensity pumping is shown in Figure 61.

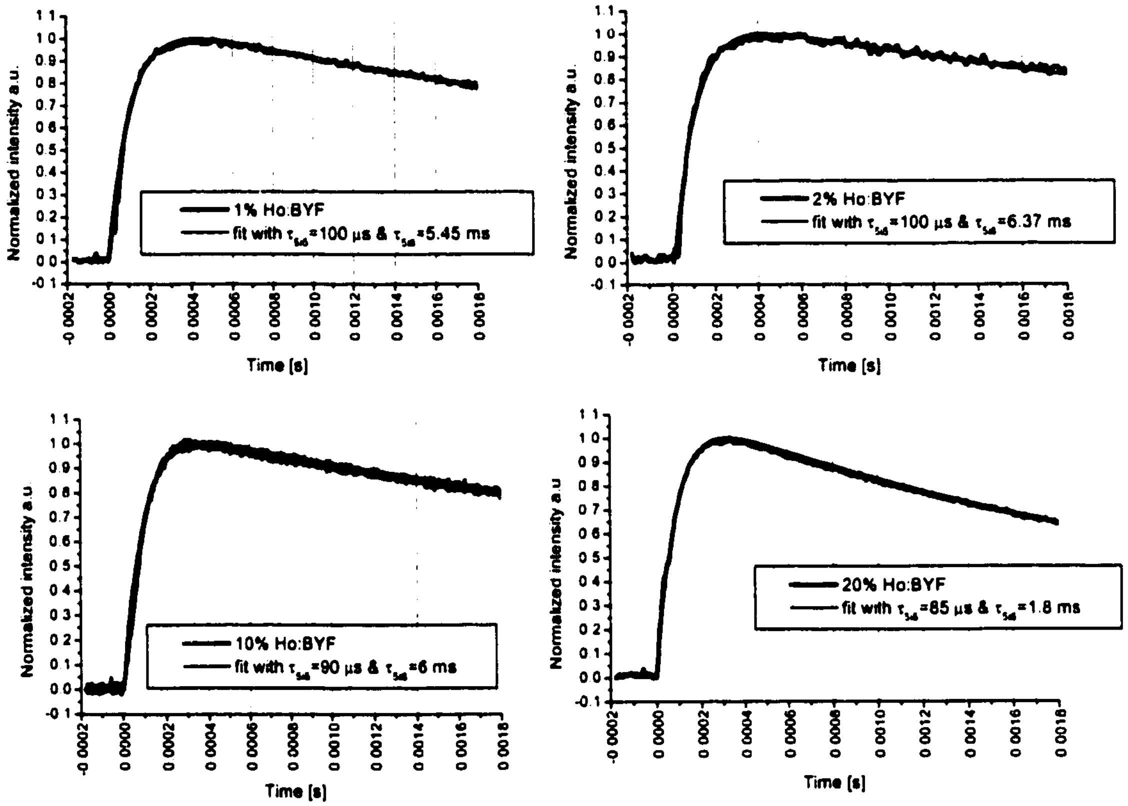

Figure 61. Temporal build up and decay of fluorescence from $^5I_6$ level at 1200 nm in Ho:BYF with Cr:LiSAF laser excitation at 890 nm at low pump peak intensities and theoretical fits with lifetimes of $^5I_5$ and $^5I_6$ used as parameters.

The shapes of the fluorescence transients for 1%, 2% and 10% samples are very similar, with the build up time of about 80 μs (characteristic of $^5I_5$ decay time) and with the decay time of 5.45 ms (which is in a good agreement with the data reported in the literature). The decay time is slightly lengthened for higher concentration samples: up to

Reproduced with permission of the copyright owner. Further reproduction prohibited without permission.

6.8 ms due to reabsorption (radiation trapping). The decay of fluorescence from 20% Ho:BYF sample, however, can be approximated by two exponentials: fast decay with the lifetime 1.8 ms in the beginning and slow decay with the characteristic lifetime of $^5I_6$ level.

In the high pump intensity conditions, the low concentration Ho:BYF samples (1% and 2%) did not exhibit any notable change in fluorescent transients from $^5I_6$ level compared to low pump intensity curves. However, in 10% sample we observed two-exponential decay with fast component lifetime ~ 620 μs and the slow component with the characteristic lifetime of $^5I_6$ level (Figure 62). In 20% sample pumped at high peak intensity, we observed also two-exponential decay with fast component lifetime of 1.5 ms and the slow component with somewhat lengthened characteristic lifetime of $^5I_6$ level. Another important observation was deduced from the relative magnitude of the 1200 nm fluorescence at high and low intensity pumping. In low concentration samples (1%, 2%) the emission signal from $^5I_6$ level was stronger at high pump intensities, while in 10% and 20% samples the emission signal from $^5I_6$ level decreased dramatically at high pump intensities compared to low pump intensity emission.

The energy transfer process, which is most probably responsible for this effect and for the fast decay component in high concentration samples pumped at high peak intensities, is upconversion from the $^5I_6$ level. In the Z-scan experiments with cw high intensity pumping at 750 nm, described in Chapter 5, the depletion of $^5I_6$ level in high concentration samples was attributed to two possible effects: excited state absorption at 750 nm or/and upconversion from $^5I_6$ level.

Reproduced with permission of the copyright owner. Further reproduction prohibited without permission.

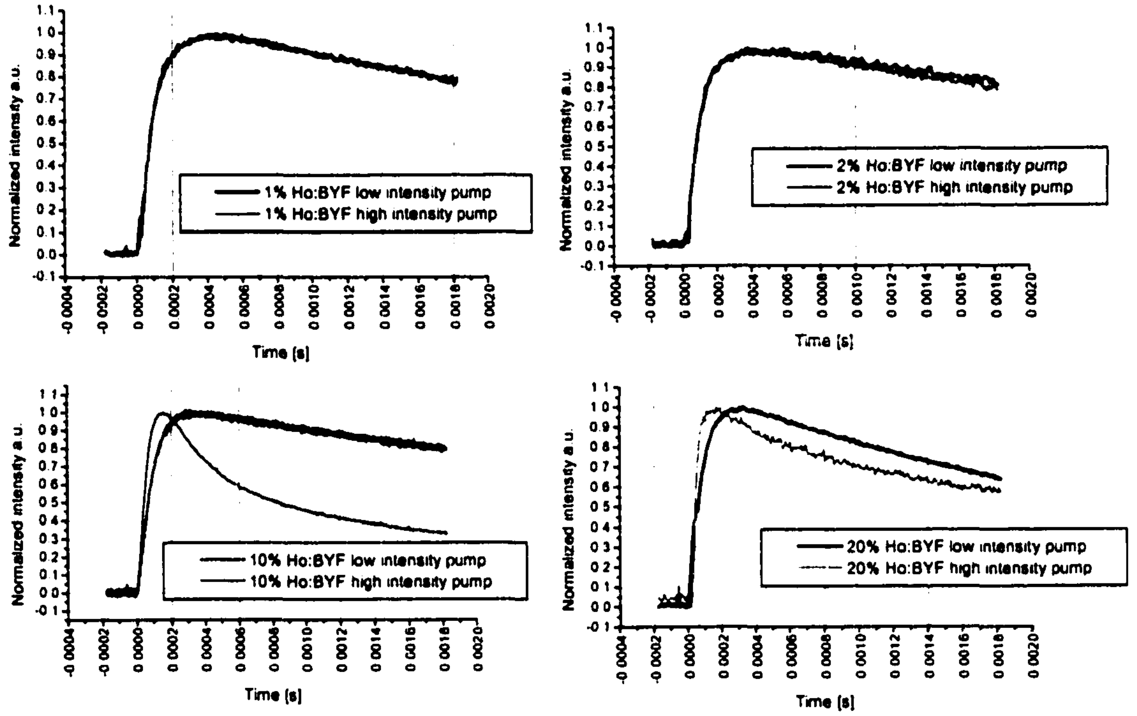

Figure 62. Temporal build up and decay of fluorescence from $^5I_6$ level at 1200 nm in Ho:BYF with Cr:LiSAF laser excitation at 890 nm at high and low pump peak intensities.

Here we can rule out the excited state absorption, since there isn't any matching transition at 890 nm from $^5I_6$ level, which leaves upconversion as the most likely mechanism of the depletion of $^5I_6$ level. To check this idea, we performed measurements of visible fluorescence transients with pulsed 890 excitation. In low concentration (1%) sample the blue fluorescence from $^5F_3$ level mostly followed the 890 nm pulse profile since there is an excited state absorption from $^5I_5$ at 890 nm. The Ho^{3+} ions are initially excited to $^5I_5$ level and from $^5I_5$ to $^5G_6$ with consequent multiphonon relaxation to $^5F_3$. The lifetime of $^5F_3$ level is estimated to be less than 10 µs. In 20% Ho:BYF, however, we observed the slow decay component in blue fluorescence which can be attributed to

Reproduced with permission of the copyright owner. Further reproduction prohibited without permission.

feeding from the $^5I_6$ level (Figure 63). These observations were very encouraging in terms of using high concentration Ho:BYF samples as gain materials for 3.9 µm laser, since the upconversion from terminal laser level $^5I_6$ reduces effective lifetime of this level within the time period when the population inversion between $^5I_5$ and $^5I_6$ is created.

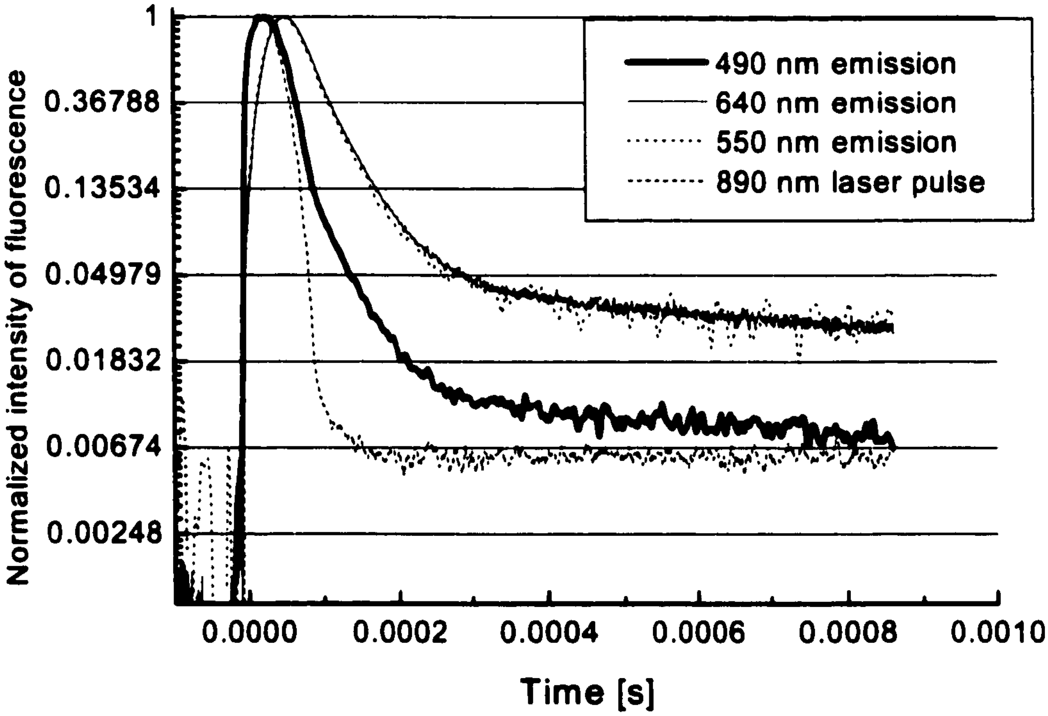

Figure 63. Visible emission build-up and decay of 20% Ho:BYF with Cr:LiSAF laser excitation at 890 nm.

6.4. Demonstration of laser action at 3.9 µm in Ho:BaY$_2$F$_8$

In the experiments for achieving laser action at 3.9 µm we used 10% and 20% Ho:BYF crystals as gain materials. The 10% Ho:BYF samples were available in a variety of orientations. Two samples were cut and polished in [100] direction, which means that b and c-axes lie in the plane of crystal's face. Two others were fabricated in [010] plane,

Reproduced with permission of the copyright owner. Further reproduction prohibited without permission.

with the b-axis along the propagation direction and the *x*- and *z*-axes in the plane perpendicular to propagation directions. The available two 20% Ho:BYF samples were cut and polished with the edges parallel to *x*, *y* (b) and *z*-axes. One of the 20% samples was 15 mm long with the *z*-axis along the propagation direction and the *x*- and b- axes in the plane perpendicular to propagation direction. Another 20% sample was 10 mm long with the *x*-axis along the propagation direction and the *z*- and b-axes in the plane perpendicular to propagation direction.

Figures 9, which illustrates the absorption spectrum of 10% Ho:BYF for light polarized parallel to b-axis of the crystal, shows that the absorption coefficient at 890 nm is the same for both orientations, $\alpha \sim 0.6\ \text{cm}^{-1}$. This implies that for the pump laser polarized along the b axis or [001] direction (perpendicular to b), the performance of the 3.9 μm laser should not be different, which we later observed in the actual laser experiments.

The absorption spectrum of the 20% Ho:BYF sample cut and polished in [010] plane is shown in Figure 10. The following absorption coefficients for two different orientations of the crystal were measured: $\alpha = 1.002\ \text{cm}^{-1}$ for polarization of light parallel to *x*-axis and $\alpha = 1.04\ \text{cm}^{-1}$ for polarization of light parallel to *z*-axis. The cross section of absorption along the *x*- and *z*-axes is by 16% smaller than along the b- or c-axes, which was also observed in the performance of the 3.9 μm laser.

The 10% Ho:BYF crystals were fabricated 20 mm long, which, in the case of [100] samples, ensured 70% of absorbed pump energy. The absorbed energy in 20 mm long [010] samples was 65% for polarization along the *z*-axis and 63% for polarization along the *x*-axis. For the 15 mm 20% Ho:BYF crystal, the absorbed pump energy was

Reproduced with permission of the copyright owner. Further reproduction prohibited without permission.

78% for polarization along the *x*-axis and 83% for polarization along the b-axis. For the 10 mm 20% Ho:BYF crystal the absorbed pump energy was 65% for polarization along the *z*-axis and 70% for polarization along the b-axis.

Laser action at 3.9 μm was initially achieved in [100] sample of 10% Ho:BYF. The cavity was end-pumped with 50 μs Cr:LiSAF laser pulses at 890 nm, at a repetition rate of 2 Hz (Figure 64).

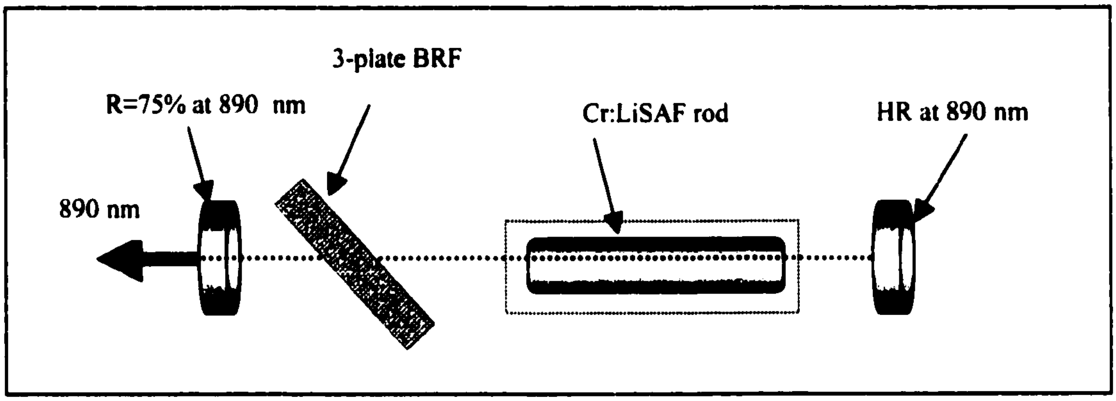

Figure 64. Pump source for the direct resonant excitation of upper level of 3.9 μm Ho:BaY_2F_8 laser: flashlamp pumped, pulsed Cr:LiSAF laser with wavelength tuning around 890 nm.

The pump beam was focused with the 25 cm focal length lens in the Ho:BYF sample. The Ho:BYF laser cavity (Figure 65) consisted of a laser crystal with entrance mirror coated on the front surface of the crystal and the 1 m radius of curvature output coupler. The entrance coating on the crystal was high reflective at 3.9 μm and 85% transmissive at 890 nm, the other face of the crystal was coated with antireflective coating at 3.9 μm. Initially we used 99% reflective output coupler. The output of the 3.9 μm Ho:BYF laser was filtered through the germanium filter in order to separate it from

Reproduced with permission of the copyright owner. Further reproduction prohibited without permission.

the pump radiation at 890 nm. The energy of the 3.9 μm laser pulse was measured with Laser Probe energy meter.

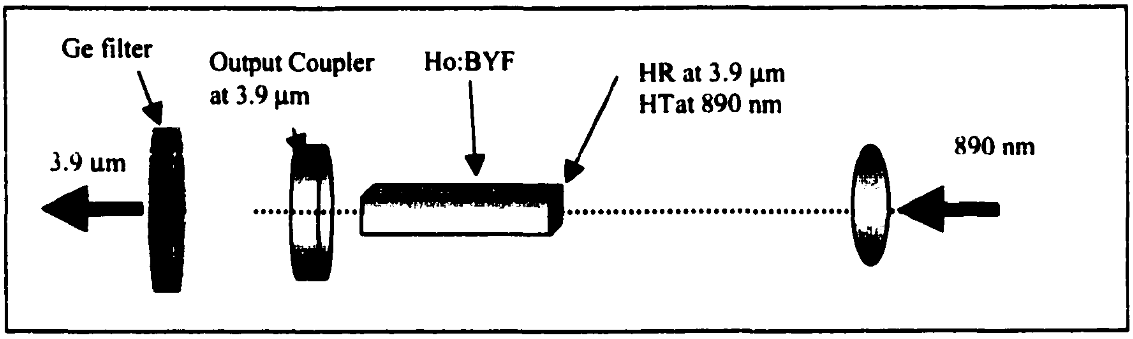

Figure 65. Cavity layout for 3.9 μm Ho:BaY_2F_8 laser with pulsed resonant pumping at 890 nm by Cr:LiSAF laser.

The polarization of pump laser was in a horizontal plane, and the laser performance was evaluated for different orientation of pump polarization with respect to the crystal axis. In the first experiment with 10% Ho:BYF sample, the laser action at 3.9 μm was achieved with a low threshold of 3 mJ absorbed pump energy and the slope efficiency of 1.35% (Figure 66). The low threshold was an indication that with the use of more transmissive output coupler we should be able to achieve higher slope efficiency. Next, we used the second available output coupler coated for 95% reflection at 3.9 μm and observed 2.55% slope efficiency. The slope efficiencies observed for two orientations of the b-axis of the Ho:BYF crystal relative to polarization of the pump were about the same, which was expected from absorption spectra around 890 nm.

Reproduced with permission of the copyright owner. Further reproduction prohibited without permission.

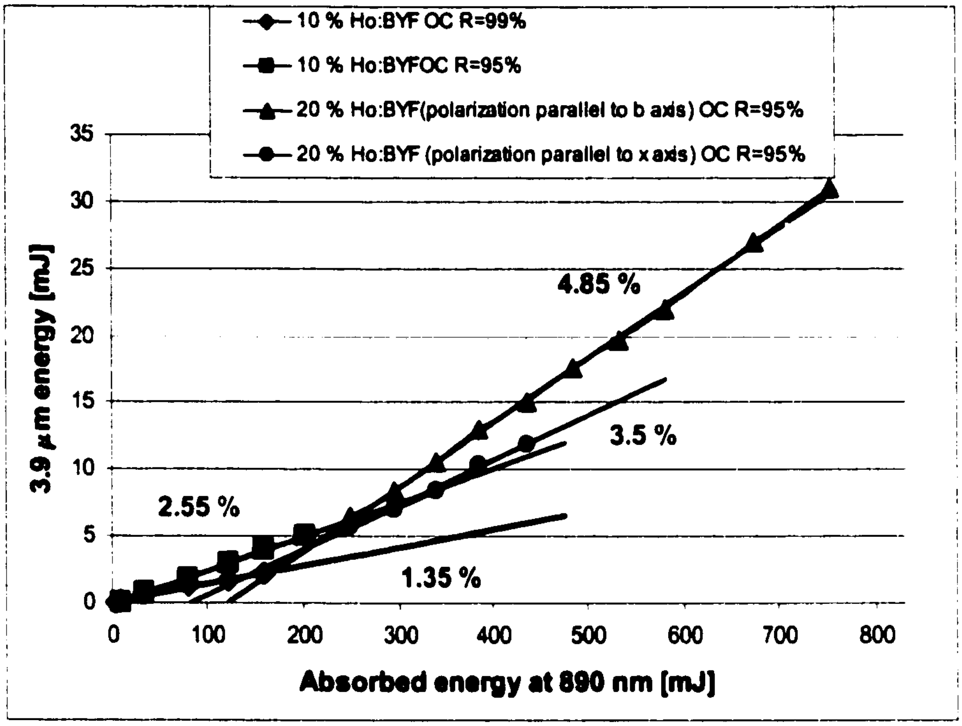

Figure 66. Performance of Ho:BYF 3.9 μm laser (initial experiments).

Next laser experiments were performed with 20% Ho:BYF 15 mm long sample. As in the case with 10% sample, the threshold of the 3.9 μm laser was quite low, 2-3 mJ. In fact, when the pump Cr:LiSAF laser was oscillating barely above its threshold, the Ho:BYF 3.9 μm laser was already lasing. In order to find the true value of 3.9 μm laser threshold, we attenuated the low energy (~ 15 mJ) output of Cr:LiSAF laser with neutral density filters to measure the performance of the Ho:BYF laser at low energies.

The performance of the 20% Ho:BYF laser is also shown in Figure 66. The slope efficiency was lower near the threshold than well above the threshold, which is caused by number of factors. The tightness of the focus of the pump beam is one of them. At higher output energies of the pump Cr:LiSAF laser, the transverse mode size of 890 nm beam is

Reproduced with permission of the copyright owner. Further reproduction prohibited without permission.

increasing, which leads to tighter focused beam in Ho:BYF laser crystal and results in higher slope efficiency. Nonuniform lasing could be another factor causing the lower slope efficiency near threshold, since at low pump energies not all of the cavity mode volume is lasing, while at higher energies the lasing fills entire cavity mode volume. Another reason for the lower slope efficiency near threshold is the quasi-three level nature of the 3.9 μm laser transition with a partially populated lower laser level, where the reabsorption of the laser wavelength by gain medium due to this population appears as a real loss near threshold [44]. At higher pump energies laser operates well above the threshold level and, in this regime, the loss decreases since the circulating energy saturates the transition and therefore the loss.

Following slope efficiencies have been demonstrated with the 20% Ho:BYF laser: for pump polarization parallel to b-axis the slope efficiency was 4.85% and extrapolated threshold of 100 mJ of absorbed pump energy. A maximum output of 31 mJ at 3.9 μm was achieved at absorbed pump energy of 750 mJ. For polarization parallel to the *x*-axis, the slope efficiency was 3.5% and extrapolated threshold of 80 mJ of absorbed pump energy.

The main technical problem we encountered in our experiments was the poor quality of the infrared coatings on the front faces of the laser samples. Even moderate pump energies occasionally produced damage spots on these coatings, which were not just localized under the focused spot of the pump pulse, but caused peeling of some areas of coatings. This in turn led to termination of laser action. Although all laser samples were coated in the same coating run, some of the coatings were more resistive to damage than the others. For example, in the initial experiments with the 10% samples, the coating damage was observed at lower input energies ~ 200 mJ compared to 1 J pump in the

Reproduced with permission of the copyright owner. Further reproduction prohibited without permission.

experiment with 20% samples, which did not allow us in the first experiments with 10% Ho:BYF laser to reach higher pump energy regime with higher slope efficiency as in the case with 20% Ho:BYF laser.

In the next experiments, we were able to demonstrate significantly higher slope efficiencies for both 10% as well as 20% Ho:BYF samples. First, the measurements of the pump beam profile were performed with traditional knife-edge technique. The measured value of the 890 nm beam waist radius focused with 25 cm focal length lens was about 650 μm. The plane-concave cavity parameters, such as 3.9 μm beam waist as a function of the resonator length, were calculated again in order to match cavity mode size with the pump spot size. The radius of curvature of the output couplers was intentionally selected as high as 100 cm in order to provide large cavity mode volume in a relatively short resonator. That also relaxed a condition on tight focusing of the pump beam in the gain medium, which allowed avoiding the damage of coatings and of the laser crystal.

With optimized cavity parameters we achieved significant improvements in the performance of the 3.9 μm laser. The 10% Ho:BYF laser was demonstrated with low threshold < 2.5 mJ and slope efficiencies of 8% and 6.6% for two different orientations of the crystal relative to polarization of the pump parallel to b- and *x*-axes, respectively (Figure 67). With 1 cm long 20% Ho:BYF laser sample we obtained laser oscillation with a threshold of less than 2.5 mJ. The slope efficiency measurements exhibit similar behavior, as it was observed before: lower slope efficiency near threshold and higher slope efficiency well above threshold (Figure 68). With the pump polarization parallel to b-axis, the measured slope efficiency near threshold was 7% and, for absorbed energies above 210 mJ, the slope efficiency was 14.5%. With the pump polarization parallel to *z*-axis, the slope efficiency near threshold was 6.1% and 14.3% for higher pump energies.

Reproduced with permission of the copyright owner. Further reproduction prohibited without permission.

The achieved slope efficiency of 14.5% corresponds to quantum efficiency of 63.4%. We expect that with improvement of the quality of the coatings and the further optimization of the key cavity parameters even higher slope efficiencies can be achieved. With the current set up and available pump energies of the order 1.5 J at 890 nm, the energy of the 3.9 μm laser can be scaled up to 60 mJ, provided the coatings will not be damaged.

Next, the measurements of the temporal profiles of the pump Cr:LiSAF laser pulse at 890 nm and Ho:BYF laser pulse at 3.9 μm were performed over a wide range of pump energies. The temporal pulse profiles of the pump laser at 890 nm were monitored with the fast silicon detector, while for the mid–infrared 3.9 μm laser pulses the fast room temperature HgCdZnTe detector was used. The pulse shapes were acquired and stored with Tektronix TDS 380 digital real time oscilloscope with 400 MHz analog bandwidth.

The pump Cr:LiSAF laser exhibits pronounced laser spiking or relaxation oscillations – most notable transient effect in solid state laser oscillators. The output of the laser consists of individual spikes with random amplitude, duration and separation. The 3.9 μm Ho:BYF laser exhibits strong relaxation oscillations as well. The spikes in the mid-infrared pulse follow the spikes in the 890 nm pump pulse. We performed the measurements of temporal profiles of both pulses at different pump energies.

Reproduced with permission of the copyright owner. Further reproduction prohibited without permission.

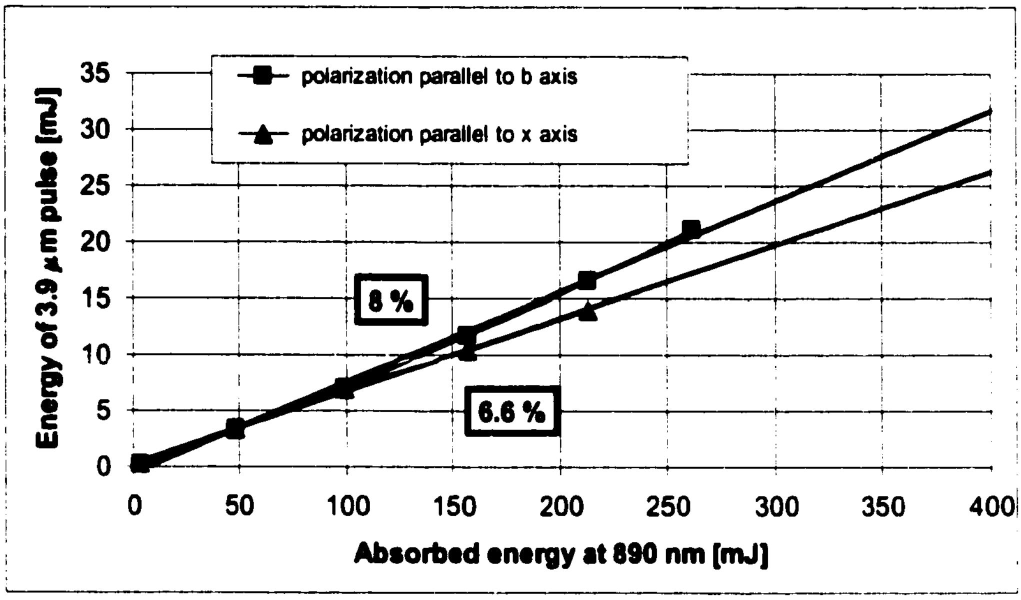

Figure 67. Performance of 10% Ho:BYF 3.9 μm laser.

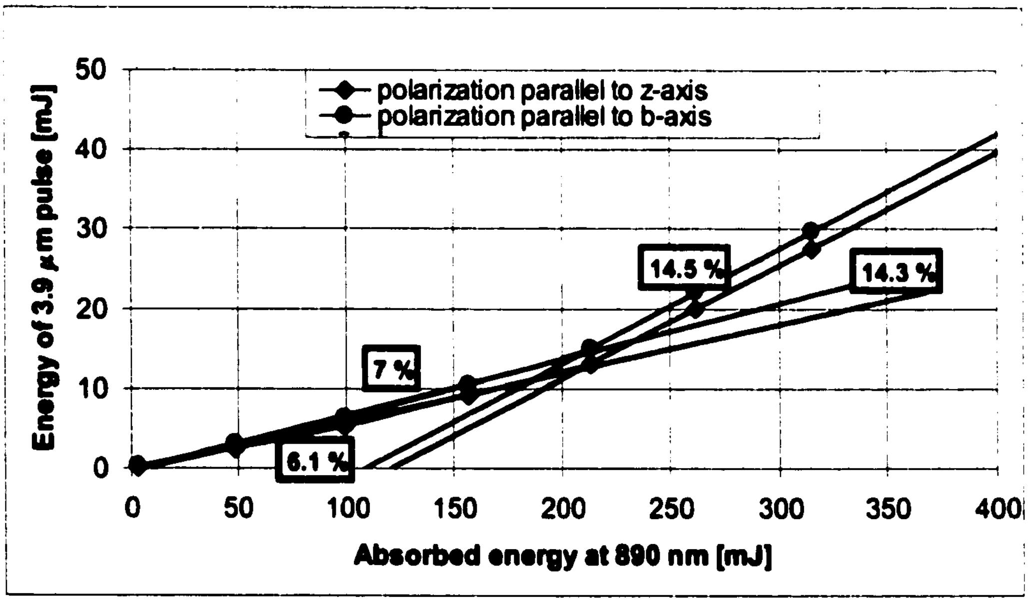

Figure 68. Performance of 20% Ho:BYF 3.9 μm laser.

Reproduced with permission of the copyright owner. Further reproduction prohibited without permission.

It can be seen in the Figure 69 that, at 15 J energy of the flashlamp, which corresponds to 150 mJ of 890 nm output, the 3.9 μm pulse envelope builds up with slower rate and decays faster than 890 nm pulse. At lower flashlamp energies, the duration of the pump pulse at 890 nm is about 35 μs, while at higher energies it increases up to 60 μs. The pulse duration of 3.9 μm Ho:BYF laser also increases with pump energies from about 30 μs at low pump energies to 80 μs at high pump energies, thereby exceeding the duration of the pump laser pulse. This effect of maintaining the inversion of the population beyond the duration of pump pulse could be attributed to a significant reduction of the effective lifetime of $^5I_6$ level due to upconversion at high pump intensity.

In Figure 70 we demonstrate the comparison of the temporal profiles of the relaxation oscillations of pump pulse and 3.9 μm pulse at different pump energies on a magnified time scale. As it can be seen, the first spike in 890 nm pump pulse at low pump energies does not allow the 3.9 μm laser to reach its threshold, and only the second spike leads to laser oscillation at 3.9 μm. At higher pump energies the mid-infrared laser starts lasing right after the first spike in a pump pulse with a time delay, which decreases with the increase in pump energy.

Reproduced with permission of the copyright owner. Further reproduction prohibited without permission.

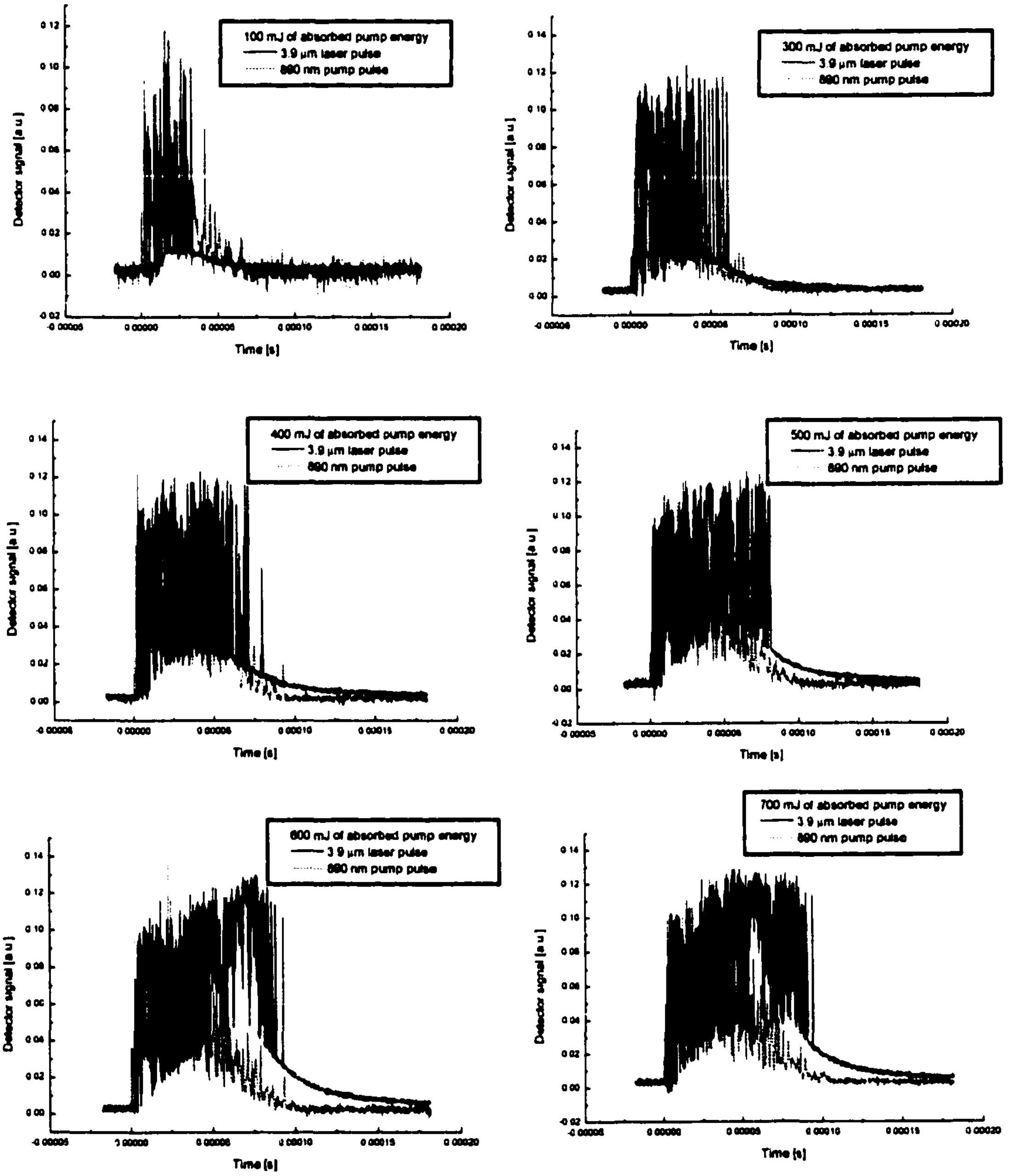

Figure 69. Temporal profile of Cr:LiSAF laser pump pulse at 890 nm at different flashlamp energies and corresponding Ho:BaY_2F_8 laser pulse at 3.9 µm.

Reproduced with permission of the copyright owner. Further reproduction prohibited without permission.

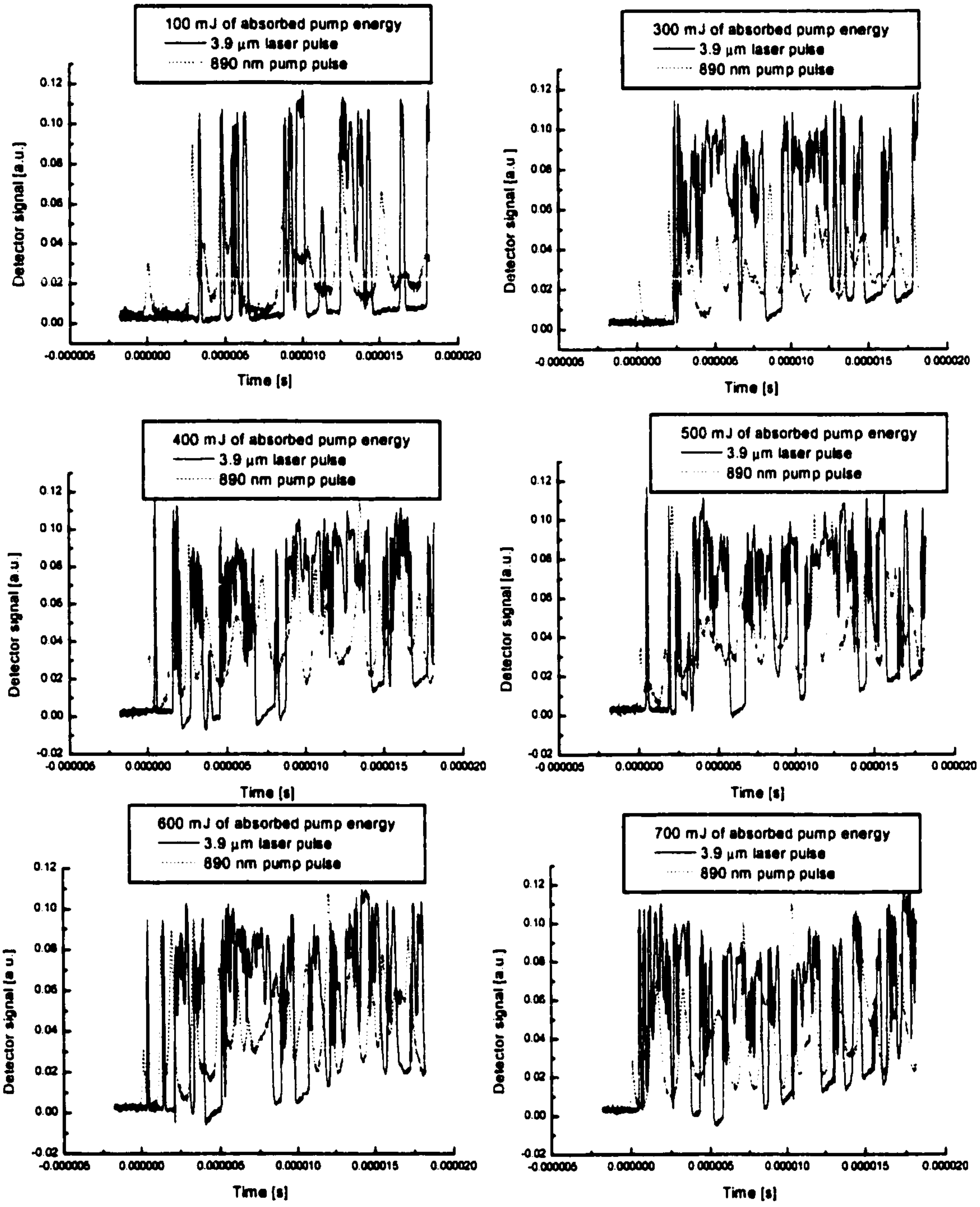

Figure 70. Temporal profile of relaxation oscillations in Cr:LiSAF laser pump pulse at 890 nm at different flashlamp energies and corresponding Ho:BaY$_2$F$_8$ laser pulse at 3.9μm.

Reproduced with permission of the copyright owner. Further reproduction prohibited without permission.

Next, we performed the measurements of the transverse mode profile of the Ho:BYF 3.9 μm laser. The Electrophysics PV-320L infrared viewing camera based on an uncooled pyroelectric BST focal plane array with infrared spectral response from 3 to 14 μm was used for our experiments. The laser beam was scattered off the diffusing surface and acquired with the IR camera. The mode patterns of the 3.9 μm laser, obtained after optimization of the Ho:BYF cavity are shown in Figure 71. With properly aligned laser, we achieved TEM_{00} mode operation with the divergence close to that of diffraction limited beam propagation.

The next experiment was designed in order to measure the spectral bandwidth and the peak wavelength of the mid-infrared Ho:BYF laser. The laser radiation was directed to the entrance slit of the 0.3 m McPherson monochromator with 300gr/mm diffraction grating blazed at 3 μm. The signal from the output slit of the monochromator was focused at InSb detector, cooled with liquid N_2, and sent to analog input of data acquisition card AT-MIO-16XE-50 in computer. The measurements of the spectral bandwidth and of the peak wavelength were performed at different pump energies (see Table 3):

The spectral range and the peak wavelength of the Ho:BYF laser, as we can see, did not change notably with the increase in pump energy.

Some issues associated with pulsed pumping of upper laser level of the 3.9 μm transition have to be taken into account. As in the short pulse pumping scheme at 532 nm the repetition rate of the laser is limited by the long lifetimes of $^5I_6$, the lower level of the 3.9 μm transition and by even longer lifetime of $^5I_7$ manifold.

Reproduced with permission of the copyright owner. Further reproduction prohibited without permission.

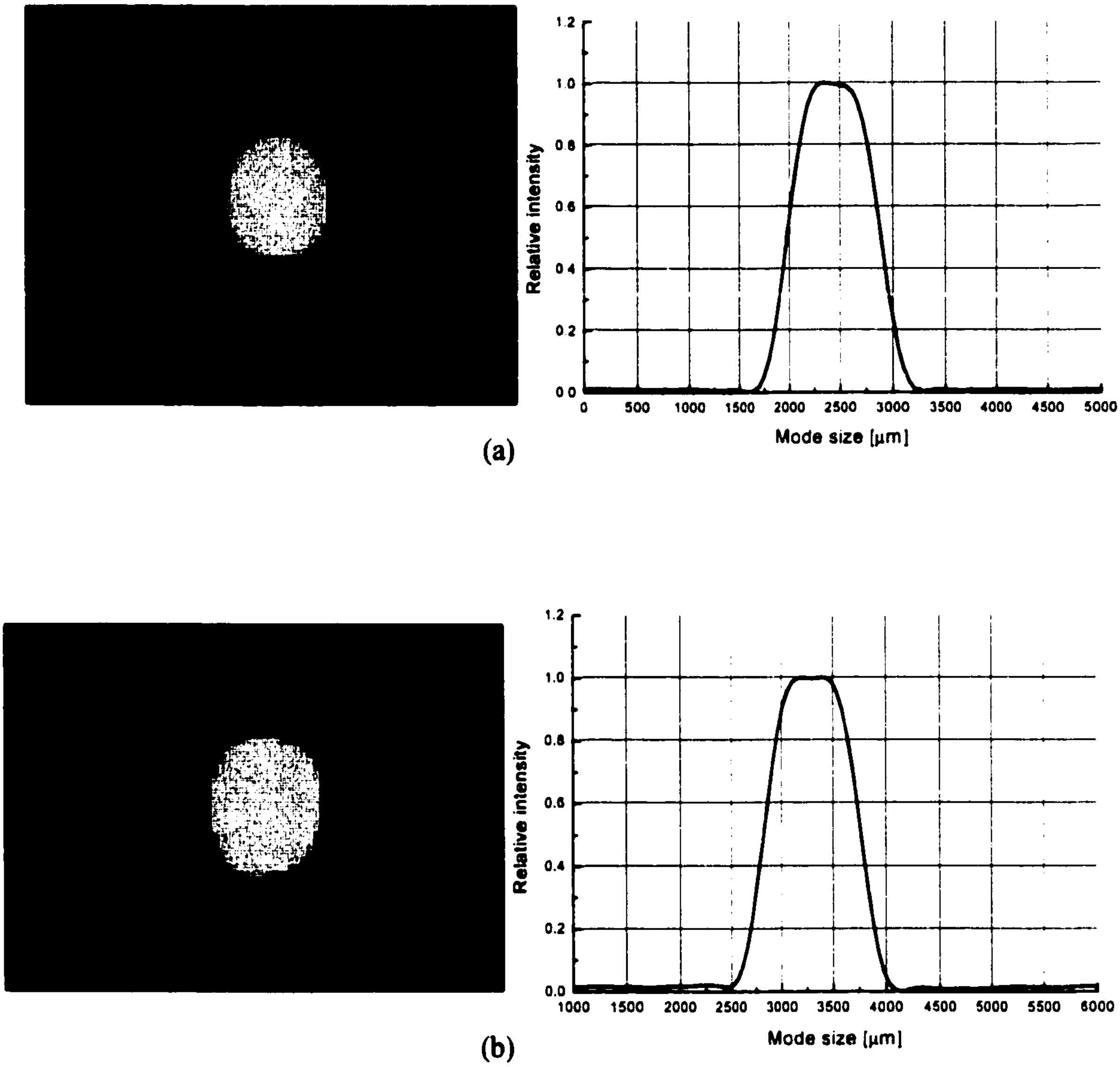

Figure 71. Transverse mode patterns of the 3.9 μm Ho:BYF laser measured by infrared camera and corresponding intensity profiles at two different distances from the laser: (a) d = 55 cm, (b) d = 107 cm.

Reproduced with permission of the copyright owner. Further reproduction prohibited without permission.

Table 3. Spectral range and peak wavelengths of Ho:BYF laser at different pump energies

Pump Energy at 890 nm [mJ]	Spectral range [nm]	Peak wavelength [μm]
85	3888.0 – 3891.6 (3.6 nm)	3.89
175	3889.4 – 3893.2 (3.8 nm)	3.8904
275	3888.0 – 3891.2 (3.2 nm)	3.8904
375	3888.8 – 3892.4 (3.6 nm)	3.89

The theoretical calculations of the dynamics of population on energy levels of holmium at different pump pulse repetition rates have indicated that up to about 50 Hz repetition rate the inversion of the population between the $^5I_5$ and $^5I_6$ levels can be maintained at a stable value. In the experiment, we tested the 3.9 μm laser performance within the range of 2 Hz to 15 Hz repetition rates (Figure 72). The 3.9 μm laser pulses were acquired at 300 mJ of pump energy at 890 nm. The temporal profile as well as energy of the 3.9 μm pulses at higher repetition rates of 15 Hz remained similar to earlier observed ones at 2 Hz.

Based on the results of our laser experiments, we expect that efficient laser operation at 3.9 μm can be also achieved in a short pulse regime by pumping it with a Q-switched Cr:LiSAF laser at 890 nm.

Reproduced with permission of the copyright owner. Further reproduction prohibited without permission.

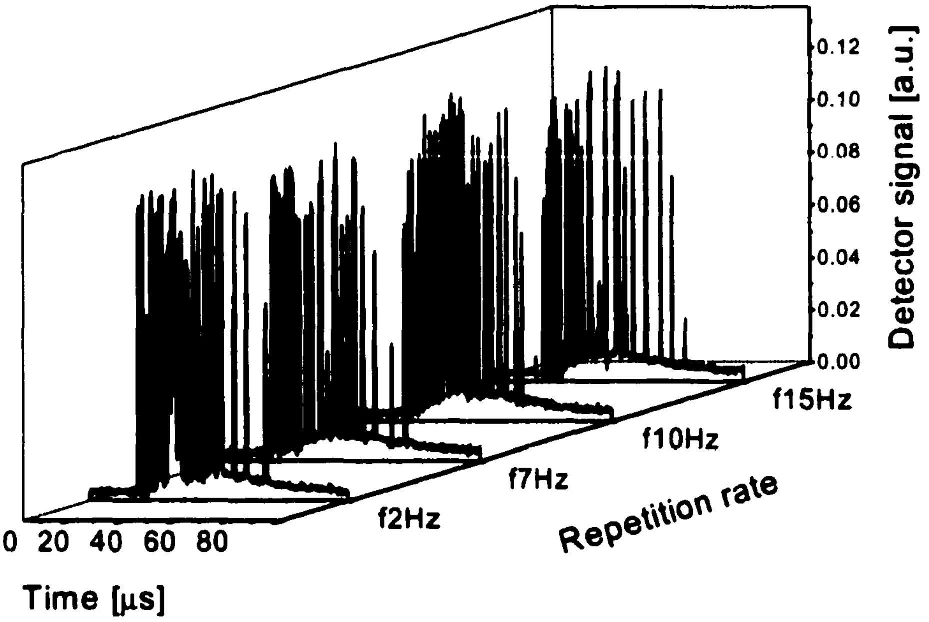

Figure 72. Temporal profile of the 3.9 μm Ho:BYF laser measured at different repetition rates.

Reproduced with permission of the copyright owner. Further reproduction prohibited without permission.

CHAPTER 7. DEVELOPMENT AND TECHNICAL DESIGN OF NEW LASER FOR HOLOGRAPHY

The goal of this part of the thesis was to develop an efficient long coherence length 640 nm pulsed laser for holography. We have designed and constructed a laser system that is a prototype for lower energy testing of actual holographic laser The active element of this laser is Pr:YLF crystal pumped by the frequency doubled Cr^{3+}:LiSAF laser at 444 nm.

Pr:YLF is a promising laser source because it offers visible red, green, blue emission from a solid state laser. Pr:YLF is a four level laser, a desirable property in a laser material. However, direct flashlamp pumping yields unacceptably low slope efficiencies due to the poor spectral overlap between the broadband pump light and the narrow Pr^{3+} absorption [45]. Therefore, a source of laser radiation at 444 nm was deemed more suitable for efficient pumping of the Pr:YLF laser. We have built and optimized such a laser: it is a flashlamp pumped frequency doubled Cr:LiSAF laser with wavelength tuning.

7.1. Flashlamp pumped Cr^{3+}:$LiSrAlF_6$ laser with wavelength tuning

Lamp pumped Cr^{3+}:$LiSrAlF_6$ (Cr:LiSAF) rod oscillators operating in the long pulse or Q-switched mode have been demonstrated by a number of groups. Zenzie et al.

Reproduced with permission of the copyright owner. Further reproduction prohibited without permission.

reported a near diffraction limited Q-switched Cr:LiSAF laser system (oscillator and amplifier) capable of producing 860 nm, 400 mJ pulses at a repetition rate of 2 Hz [46]. At a 31 J flashlamp energy delivered in 75 μs long pulse, the oscillator with 5x100mm Cr:LiSAF rod produced 75mJ of near diffraction limited (M^2=1.5) output in a 126 ns pulse. The output of the double pass amplifier with 7x100mm Cr:LiSAF rod pumped at 45J lamp energy was 400 mJ at 860 nm. In the same paper the harmonic generation results were reported: with 10mm long BBO crystal 200 mJ of energy at 430 nm was achieved and 40 mJ - at 215 nm. Stalder et al. reported a flash-lamp-pumped long-pulse Cr:LiSAF laser with a slope efficiency of 5% and an overall efficiency of 3.1% at 845 nm [47]. The same group obtained Q-switched pulse generation with a rotating mirror and observed 150 mJ pulses with duration of 40-50ns. Shimada et al. have demonstrated an electro-optically Q-switched multimode flashlamp pumped Cr:LiSAF oscillator that emitted 455 mJ of energy in a 32 nsec pulse [48]. Energies in excess of 70 J have been extracted in single, free-oscillation pulse from a flashlamp pumped 25 mm diameter, 200 mm long, 0.7% Cr doped Cr:LiSAF laser [49].

The Cr:LiSAF rod used in our laser has the dimensions of 6 mm diameter by 80 mm in length and is mounted in a single flashlamp pumped, close coupled diffuse reflecting pump chamber (IR Sources, Inc.). The Cr:LiSAF is a uniaxial crystal. The laser rod was oriented and positioned with the c-axis of the crystal in the horizontal plane, forcing the laser oscillation with polarization in the same plane. Electrical energy is supplied to the flashlamp using Analog Modules, Inc. Model 8800V fixed pulsewidth flashlamp power supply. This supply can produce electrical pulses to the flashlamp with energy up to 100 J and pulsewidths on the order of the 100 microseconds. This power

Reproduced with permission of the copyright owner. Further reproduction prohibited without permission.

supply is a special configuration 8800 master/slave system with double pulse capability, which can allow to use a second lamp for the experiment involving a second gain medium.

In order to use Cr:LiSAF laser for efficient pumping of Pr:YLF laser, it was necessary to match exactly the pump wavelength to the peak of absorption line of the Pr:YLF crystal at 444 nm. Therefore, the fundamental frequency of flashlamp pumped Cr:LiSAF laser had to be tuned to 888 nm. Two different methods of tuning of Cr:LiSAF laser were tested: wavelength tuning with Littrow prism and with birefringent filter.

7.1.1. Linear cavity configuration with Littrow prism

The initial step in all sets of experiments was the construction of Cr:LiSAF laser with linear cavity and wavelength tuning. In the first cavity configuration the resonator consisted of a pump chamber with a flashlamp pumped Cr:LiSAF rod, a Littrow prism for wavelength tuning, used at the same time as the rear mirror, and an output coupler (Figure 73). The front face of the Littrow prism was positioned at a Brewster angle in order to minimize the reflection losses for horizontally polarized light in the cavity.

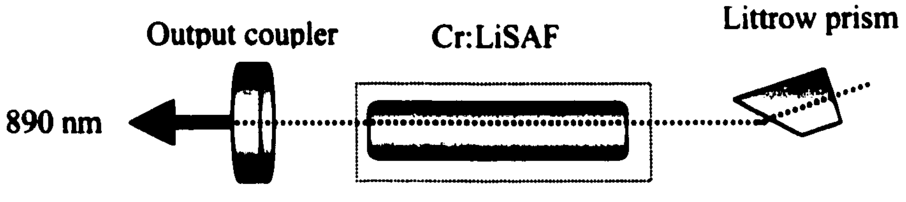

Figure 73. Linear cavity configuration with Littrow prism.

Reproduced with permission of the copyright owner. Further reproduction prohibited without permission.

Laser action was achieved with the threshold of 8 J of flashlamp energy. The laser repetition rate was 2 Hz. We performed measurements of the peak wavelength of the Cr:LiSAF laser with the linear cavity. The beam from the laser was focused on the entrance slit of the 0.3 m McPherson monochromator. At the exit slit of the monochromator signal was measured with the fast silicon detector and was sent to the Tektronix digital oscilloscope. The peak wavelength of the free running laser was at 857.6 nm, which corresponds to the peak of the gain curve of Cr:LiSAF crystal. The Littrow prism was adjusted in horizontal plane in order to tune the laser wavelength to 888 nm.

The performance of the laser at 888 nm was evaluated for three cavities with the Littrow prism and three different output couplers. The slope efficiency of the laser with R=95% output coupler was 0.74%, with R=90% output coupler – 1.32%, and with R=75% output coupler – 2.7% (Figure 74).

In the next experiment we performed measurements of wavelength tuning range of the Cr:LiSAF laser with Littrow prism. In the set-up the double-grating SPEX spectrometer with 1200 gr/mm gratings blazed at 500 nm was used.

The measurement of the wavelength tuning bandwidth was performed for the linear cavity with 75% output coupler at 30 J lamp energy. The selective reflectivity of the coating on the back surface of the Littrow prism allows suppressing the wavelengths below 830 nm (Figure 75).

The same set-up was used to measure the pulse profile at 888 nm. The duration of the single pulse was about 70 μs. As many other solid state pulsed laser systems, our Cr:LiSAF laser exhibits pronounced laser spiking or relaxation oscillations. Figure 76

Reproduced with permission of the copyright owner. Further reproduction prohibited without permission.

shows several consecutive pulses from the Cr:LiSAF laser with the linear cavity with Littrow prism for wavelength tuning. In addition to the initial oscillations, the laser spiking behavior is reexited during the pulse by various cavity perturbations such as instabilities in the flashlamp pulse.

A variety of techniques for suppression of laser spiking, by introducing of active and passive feedback into the cavity has been reported in the literature [50,51,52]. One such method is suppression of laser spiking by intracavity frequency doubling [53]. Although for this particular project the relaxation oscillations in our Cr:LiSAF laser were not our main concern, however, the intracavity frequency doubling was expected to not only provide much higher energy of second harmonic than extracavity frequency doubling, but also notably damp relaxation oscillations.

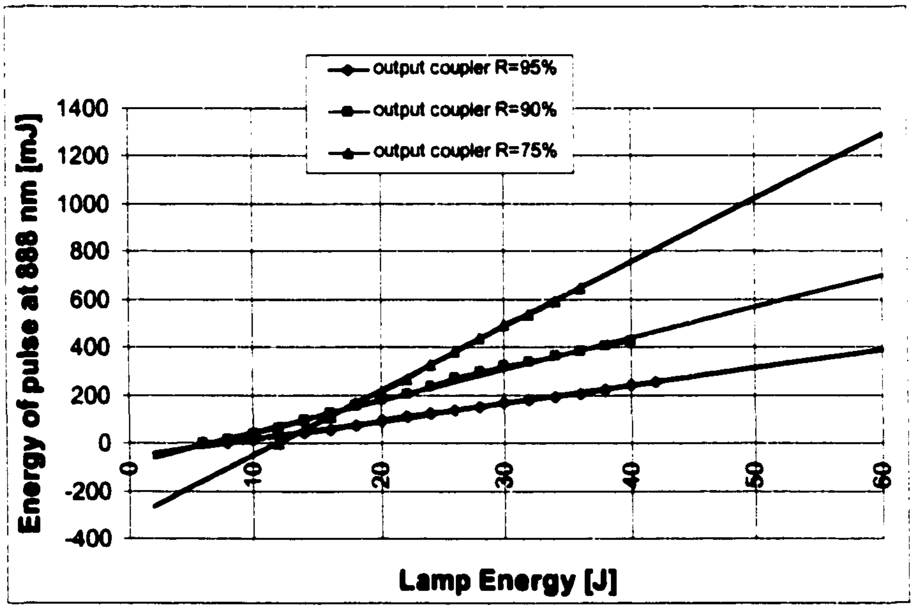

Figure 74. Performance of Cr:LiSAF laser at 888 nm for three linear cavities with Littrow prism and three different output couplers.

Reproduced with permission of the copyright owner. Further reproduction prohibited without permission.

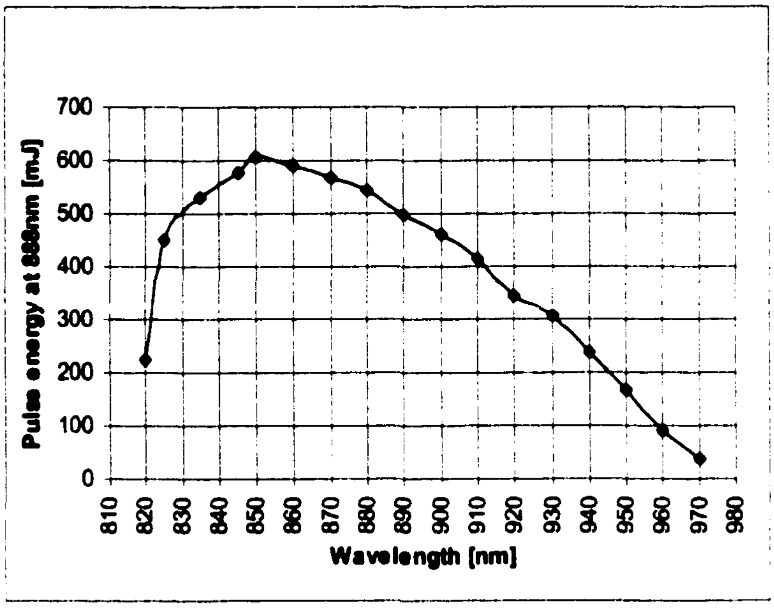

Figure 75. Wavelength bandwidth for Cr:LiSAF laser with linear cavity and Littrow prism used as a tuning element.

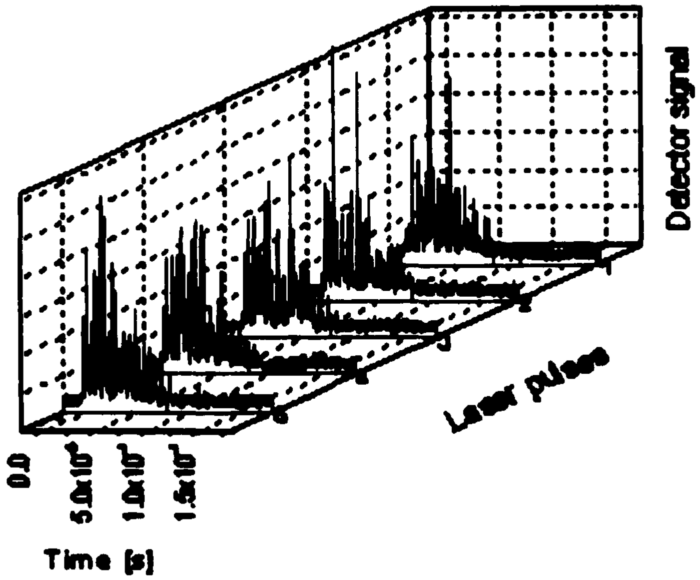

Figure 76. Temporal profile of laser pulses of Cr:LiSAF laser with linear cavity and Littrow prism.

Reproduced with permission of the copyright owner. Further reproduction prohibited without permission.

7.1.2. The 3-mirror V-shaped cavity with Littrow prism

In order to accomplish efficient intracavity frequency doubling, several different cavity configurations were considered. The laser cavity had to be designed in such a way that: 1) it provides tight beam waist (high power density of the fundamental beam) at the nonlinear crystal position for efficient second harmonic generation (SHG); 2) the frequency doubled beam has to be extracted from the cavity before it gets reabsorbed by the gain medium.

To satisfy these conditions we have designed and constructed a Cr:LiSAF laser with three mirror V-shaped cavity. The resonator consisted of pump chamber with flashlamp pumped Cr:LiSAF rod, a Littrow prism for wavelength tuning also used as a rear mirror, and two concave mirrors (Figure 77).

The nonlinear crystal had to be later placed in the beam waist located between two concave mirrors. The folding mirror M1 is positioned so, that it reflects the beam at a smallest possible angle to the axis of the long arm of the laser cavity, in order to minimize astigmatism in the laser mode. The folding mirror is high reflective at 888 nm and high transmissive at 444 nm. This does not allow the second harmonic beam to be reflected back into the long arm of the resonator, thus preventing its reabsorption by the Cr:LiSAF gain medium. The radius of curvature of that mirror is 10 cm; it is meniscus shaped in order to decrease the divergence of the output beam. The third mirror M2 is high reflective at both 888 and 444 nm and it also has 10 cm radius of curvature. Unfortunately, this was the only available set of mirrors provided for our experiments. As

Reproduced with permission of the copyright owner. Further reproduction prohibited without permission.

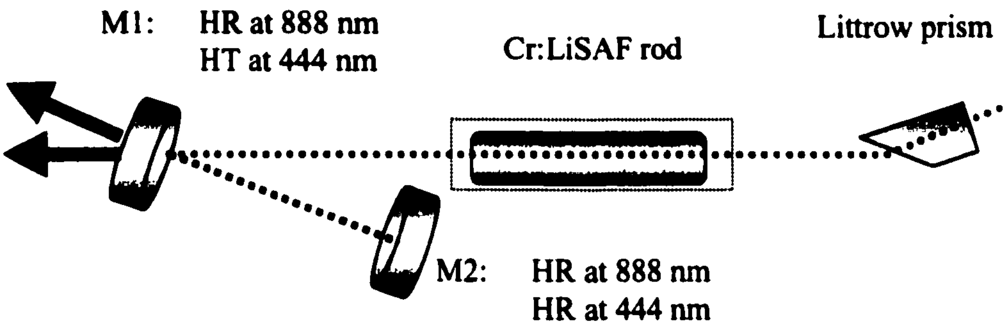

Figure 77. Cr:LiSAF laser with 3-mirror V-shaped cavity with Littrow prism.

we will show later in the analysis of the 3 – mirror cavity, the radii of curvature of 10 cm created strongly converging and diverging mode in the short arm of the resonator between two concave mirrors, thereby limiting efficiency of intracavity frequency doubling.

We achieved laser oscillation with three mirror cavity with even lower threshold - 4 J of lamp energy since all three cavity mirrors were high reflective at 888 nm. The wavelength tuning, however, turns out to be a challenging task for this cavity configuration. The optimized laser tends to operate at a peak wavelength of the gain curve with the width of the line in the order of ~10 nm. The horizontal adjustment of the Littrow prism was implemented for the wavelength tuning as before. The wavelength tuning range, however, was smaller than in the linear cavity configuration. The wavelength of the laser had the tendency of "jumping" back to the peak wavelength. This behavior could be explained by the beam "bending" in the cavity in the conditions of lasing through the wide aperture of the Littrow prism and insufficient suppressing of the

Reproduced with permission of the copyright owner. Further reproduction prohibited without permission.

unwanted wavelengths. The insertion of the aperture in the cavity has somewhat improved the tuning of the laser.

7.1.3. Linear cavity configuration of Cr:LiSAF laser with birefringent filter used for wavelength tuning

In the second set of experiments we tested an alternative method of the wavelength tuning by using the three plate birefringent filter (BRF) in Cr:LiSAF laser cavity. Initially we assembled the linear cavity consisting of pump chamber with flashlamp pumped Cr:LiSAF rod, the BRF for wavelength tuning, the rear mirror, and three different output couplers with 90%, 95% and 75% reflectivities at 888 nm (Figure 78).

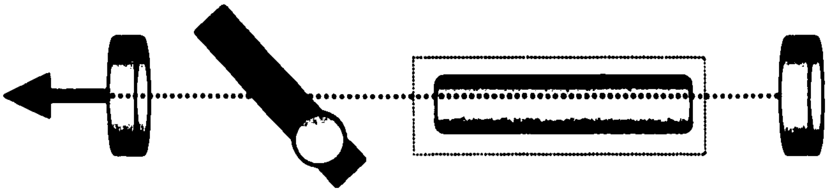

Figure 78. Linear cavity configuration of Cr:LiSAF laser with birefringent filter.

The comparison of slope efficiencies of linear cavities with BRF and Littrow prism shows clearly, that with thoroughly aligned laser, the cavity with BRF and 75% output coupler has higher slope efficiency 3.1% than the cavity with the Littrow prism and the same output coupler ~2.7% (Figure 79).

Reproduced with permission of the copyright owner. Further reproduction prohibited without permission.

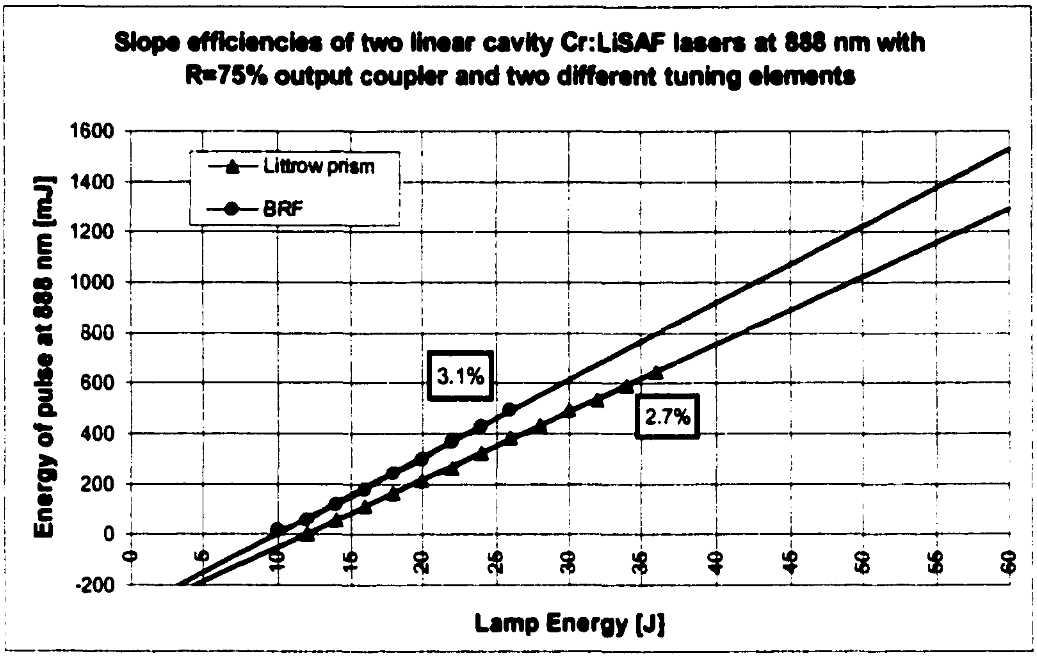

Figure 79. Slope efficiencies of Cr:LiSAF laser with two tuning elements.

For the tuning of the Cr:LiSAF laser we had the choice of using a single plate or a three plate BRF. Since the amplitude transmittance of the single stage filter is quite high at unwanted wavelengths, this could not provide adequate suppression of those wavelengths. As a result the wavelength of the laser would have a tendency of "jumping" to the peak wavelength of the gain. The alternative approach that we've chosen for the narrowing the width of the central passband of the filter was to use several crystals in series whose thicknesses vary by integer ratio. The thickness ratio of the plates of the BRF used in Cr:LiSAF laser was 1T, 2T, 15T (T=.61 mm).

The central passband of the 3-plate BRF was considerably narrower (<0.3 nm) than the resolution of the 0.3 m McPherson spectrometer with a 1200 gr/mm grating. The

Reproduced with permission of the copyright owner. Further reproduction prohibited without permission.

continuous wavelength tuning of the laser was easily implemented through rotation of the BRF. We performed the measurements of the wavelength tuning bandwidth for the linear cavity with 75% output coupler at 30 J lamp energy (Figure 80).

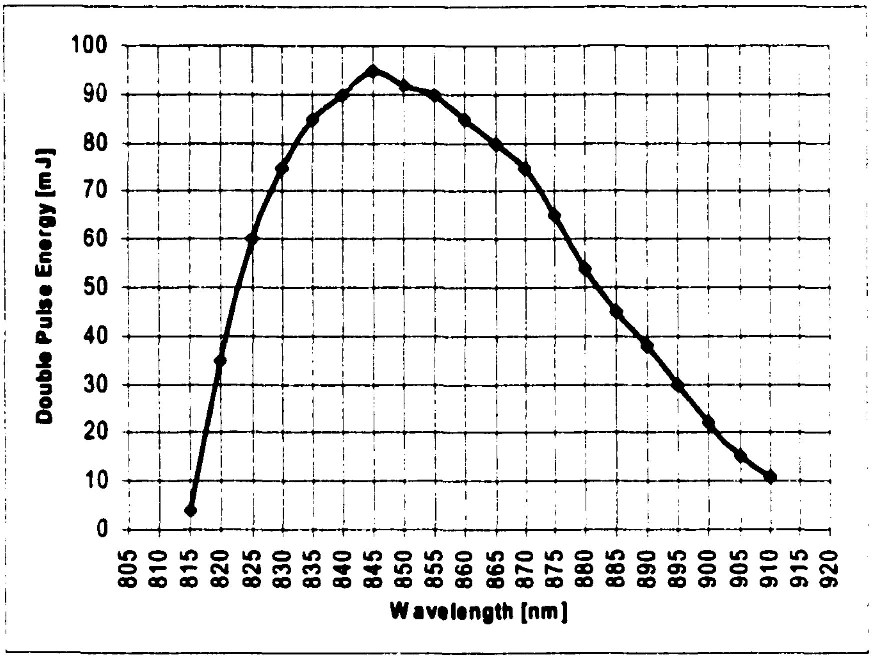

Figure 80. Wavelength bandwidth for Cr:LiSAF laser with linear cavity and BRF used as a tuning element.

The measurements of the temporal profile of the laser pulse at 888 nm with the linear cavity configuration using BRF for wavelength tuning, have demonstrated pronounced laser spiking or relaxation oscillations, similar to ones observed in the measurements with the cavity with Littrow prism (Figure 81). The measurements were performed for different pump energies.

Reproduced with permission of the copyright owner. Further reproduction prohibited without permission.

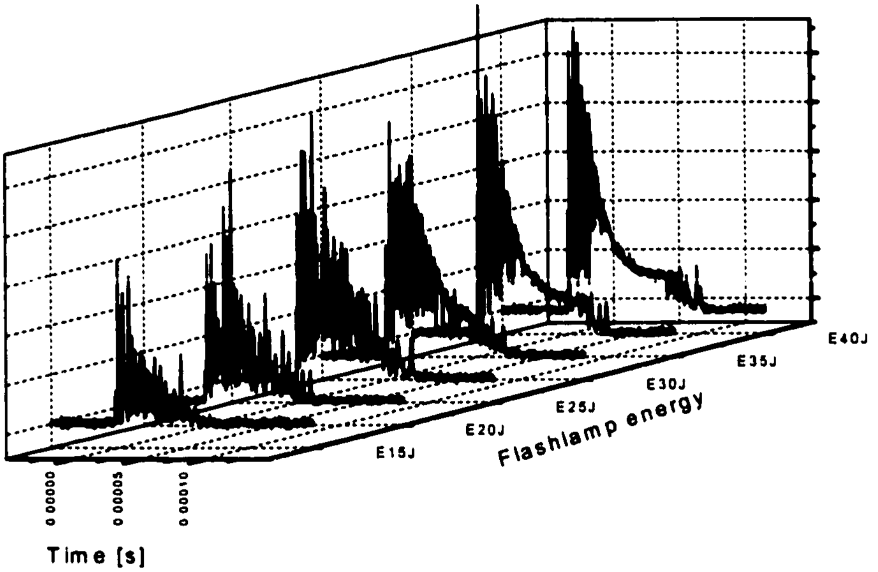

Figure 81. Temporal profile of laser pulses of Cr:LiSAF laser with linear cavity and BRF.

The laser pulse at low flashlamp energies consists of the sequence of ~1 microsecond spikes, while at high energies its temporal profile resembles an 70 μs long pulse envelope with amplitude fluctuations at the beginning of the pulse.

7.1.4. The 3-mirror V-shaped cavity configuration with BRF

We proceeded further, and assembled the V-shaped cavity with BRF. Since the BRF provides much narrower linewidth of the laser than Littrow prism, it was important to observe experimentally if that will affect the efficiency of intracavity frequency conversion in nonlinear crystal.

Reproduced with permission of the copyright owner. Further reproduction prohibited without permission.

The cavity layout was similar to the 3-mirror V-shaped cavity with the Littrow prism, except for the tuning element (BRF) and a separate flat back mirror high reflective at 888 nm (Figure 82).

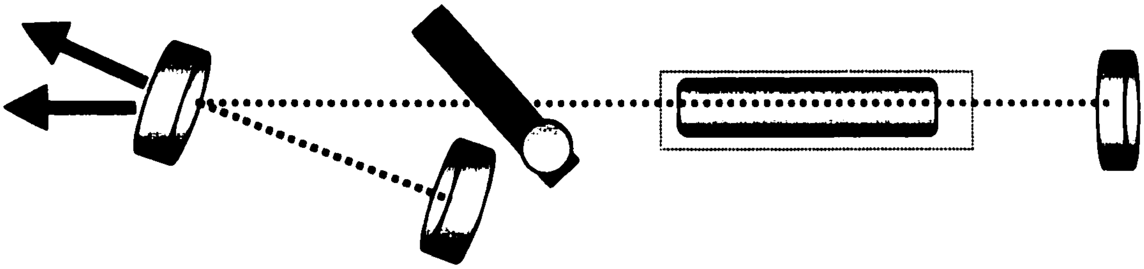

Figure 82. Cr:LiSAF with 3-mirror V-shaped cavity with BRF.

In order to preliminary estimate expected blue energy in the intracavity frequency doubling scheme, we decided to find the value of the fundamental energy oscillating between high reflective mirrors in the V-shaped cavity. First, the folding mirror was replaced by an output coupler, and the infrared pulse energy was measured in both output directions: collimated - from the long arm and the diverging – from the short arm of the resonator. The values of the pulse energy in both arms are the same and they are equal to half of the total energy out. The total energy out was measured by replacing the flat high reflective back mirror with three different output couplers, used in the experiments with linear cavities. For all three output couplers: R=95%, R=90%, R=75%, the slope efficiencies of the three linear cavities are consistently higher than the slope efficiencies of the three V-shaped cavities. This could be attributed to the restricted transverse mode

Reproduced with permission of the copyright owner. Further reproduction prohibited without permission.

oscillation in the V-shaped cavity compared to linear cavity and additional loss through third mirror. The slope efficiency of the laser with R=75% output coupler was 1.73%.

7.2. Frequency doubling of Cr:LiSAF laser

7.2.1. Choice of nonlinear crystal for inrtracavity frequency doubling

Initially three nonlinear crystals: LiB_3O_5 (LBO), $KNbO_3$ and β-BaB_2O_4 (BBO) were considered as the most suitable candidates for frequency doubling of Cr:LiSAF laser radiation. Although LBO has a lower effective nonlinear coefficient than $KNbO_3$, it has much higher angular, spectral, and temperature acceptance bandwidths [54]. In addition, LBO has much better thermal conductivity and a higher damage threshold. The main advantages of BBO over the LBO are higher effective nonlinear coefficient and temperature acceptance bandwidth. However, it suffers from much smaller angular and spectral bandwidths, thermal conductivity and damage threshold.

The comparison of key properties of the three nonlinear crystals of our interest is presented in the table 4 below.

In the reference, the $KNbO_3$ crystal was used for extracavity frequency doubling of Cr:LiSGaF laser [55]. In the extracavity second harmonic generation (SHG) scheme the infrared laser output was then focused into a 10 mm long crystal of a-cut $KNbO_3$. With the input field polarized along the crystals b axis and the crystal temperature maintained at 80° C there is non-critical phase matching for the of 880 nm radiation. With10 mJ of 442 nm input, 4mJ at 640 nm, 3.1 mJ at 528 nm and 0.7 mJ at 479 nm was achieved.

Reproduced with permission of the copyright owner. Further reproduction prohibited without permission.

Table 4. Comparison of key properties of 3 nonlinear crystals

	LBO	BBO	KNbO3
Deff [pm/V]	0.778	2.01	-10.8
Acceptance angle [mrad/cm]	2.05	0.43	0.62
Spectral acceptance bw [cm-1/cm]	18	11	1.5
Temperature range [K/cm]	7.91	26.10	0.39
Thermal conductivity [W/cm-K]	0.035	0.016(π) / 0.012(σ)	
Damage threshold (10 ns pulse) At 1064 nm [J/cm^2]	25	13	1.7

The fact that the energy of the blue pump pulse used for pumping the Pr:YLF laser was limited in the extracavity SHG scheme was also the main reason limiting the efficiency of Pr:YLF. To overcome this, the intracavity SHG scheme was tested [55]. Frequency conversion was accomplished with a 3 mm LBO critically phase matched for a Type I interaction in the XY plane. In this experiment, as much as 80 mJ of 442 nm was reported.

We used initially an 8 mm long LBO crystal for accomplishing intracavity SHG of Cr:LiSAF laser. Two fused silica windows with AR coatings at 880 nm and 440 nm were optically contacted to both faces of the LBO crystal in order to minimize the reflection losses in the cavity.

Reproduced with permission of the copyright owner. Further reproduction prohibited without permission.

7.2.2. Intracavity frequency doubling of Cr:LiSAF laser

After constructing and optimizing the 3-mirror V-shaped cavity with Littrow prism, described in the section 1.2, we have accomplished intracavity frequency doubling by inserting the nonlinear LBO crystal in the beam waist in the short arm of the cavity between two concave mirrors (Figure 83). The third mirror was mounted in a gimbal mount, which furthermore was mounted on a three-dimensional translation stage to allow precise tuning of the wavefront within the nonlinear medium.

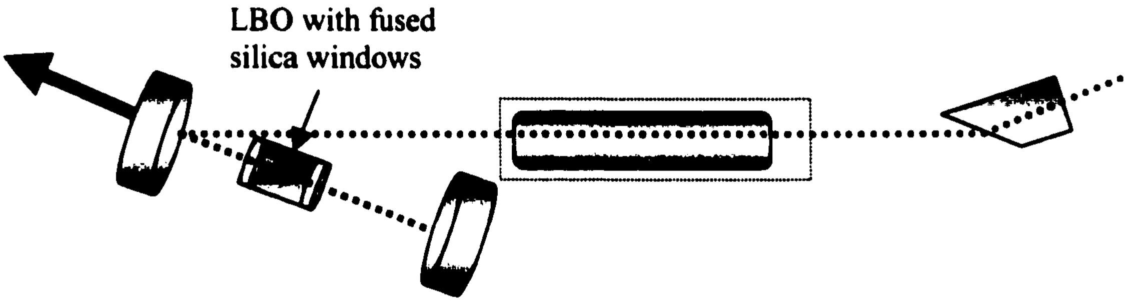

Figure 83. Intracavity frequency doubling of Cr:LiSAF laser cavity with Litrow prism.

The 8 mm LBO crystal was critically phasematched for a Type I interaction in XY principal plane. Long resonator of Cr:LiSAF laser leads to the decrease of the longitudinal cavity mode spacing and hence allows many modes to oscillate. This essentially averages out amplitude fluctuations due to mode coupling in the nonlinear crystal thus allowing a smooth second harmonic output pulse, as it was also reported in the literature [56,57,58].

Reproduced with permission of the copyright owner. Further reproduction prohibited without permission.

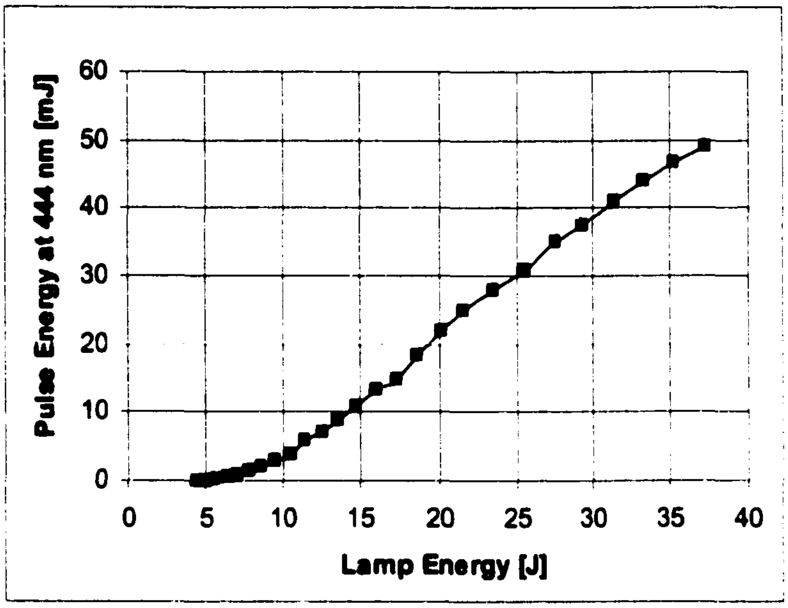

Figure 84. Pulse energy at 444 nm as a function of the lamp energy in intracavity frequency doubled Cr:LiSAF laser with Littrow prism.

The main concern here was the damage of the coatings on the fused silica windows or creation of air bubbles on the interfaces between the crystal and windows due to high power density in the tight beam waist in the short arm of the resonator. These factors led later to some degradation of the conversion efficiency.

We performed the measurements of the pulse energy at 444 nm as a function of the lamp energy. For optimized cavity we obtained as much as 50 mJ of energy in the blue pulse with 37.7 J lamp energy (Figure 84).

Intracavity frequency doubling was also accomplished in the laser tuned with BRF by inserting 8 mm LBO crystal in the beam waist in the short arm of the V-shaped cavity between two concave mirrors (Figure 85).

Reproduced with permission of the copyright owner. Further reproduction prohibited without permission.

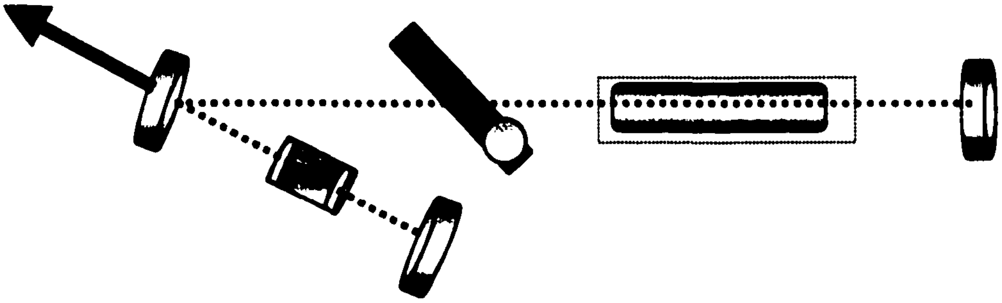

Figure 85. Intracavity frequency doubling of Cr:LiSAF laser cavity with BRF.

The energy measurements of the blue pulse are shown in Figure 86. For the optimized cavity we obtained as much as 30 mJ of energy in the blue pulse with 40 J lamp energy.

Due to degraded quality of windows bonded to LBO, efficiency of the intracavity frequency doubling was lower for cavity with BRF than for cavity with Littrow prism. It has slightly decreased even during the operation: at 25 J of lamp energy we initially obtained 18 mJ of energy in the blue pulse compared to 14 mJ after running the laser for a while.

In order to improve the efficiency of intracavity frequency doubling the LBO crystal was sent for repair: two fused silica windows with damaged AR coatings at 880 nm and 440 nm were removed, the LBO crystal faces were repolished and new windows were optically contacted to both faces of the crystal. This time special precautions were taken to avoid the damage of the LBO crystal. Prior to insertion of the doubling crystal in the beam waist between two concave mirrors, the plane parallel 8 mm slab of glass with the similar properties as LBO (refraction index, transparency and damage threshold) was

Reproduced with permission of the copyright owner. Further reproduction prohibited without permission.

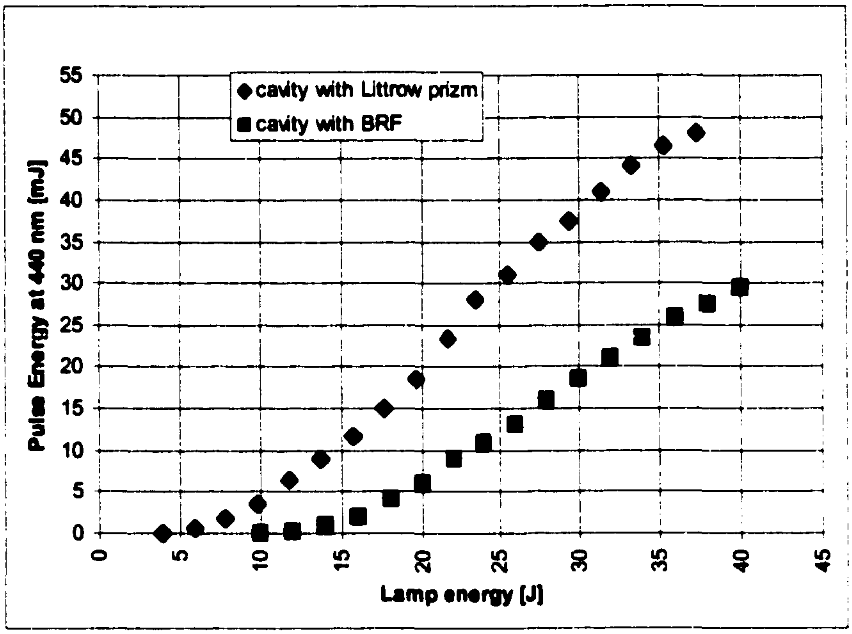

Figure 86. Pulse energy at 444 nm as a function of the lamp energy in intracavity frequency doubled Cr:LiSAF laser with two different tuning elements.

placed in the short arm of the cavity, in order to locate the beam waist and to measure the damage threshold. Then, the glass slab was removed and the nonlinear LBO crystal was inserted between two concave mirrors far from the beam waist. Although the laser operated well below the damage threshold of the crystal, the air bubble has developed again on the interface between the window and the crystal. This may have occurred due to number of reasons such as: imperfections of the polished surface of the LBO crystal and windows, high energy density of the beam within the resonator.

We have revised the design of our cavity and performed numerical analysis for determining the beam size and curvature of wavefront at any position in the resonator.

Reproduced with permission of the copyright owner. Further reproduction prohibited without permission.

7.3. Numerical analysis of V-shaped cavity

7.3.1. Ray tracing for the Gaussian beam in the resonator: theoretical modeling of the laser cavity using ABCD matrix method

Our goal in this part of the work was to study the propagation of Gaussian beams in the 3-mirror cavity of flashlamp pumped Cr:LiSAF laser. Deviations from the Gaussian beam profile, e.g. due to higher order laser modes, can be treated by means of the M^2-method [59]. For simplicity we confine our analysis to the fundamental Gaussian modes. The problem of using ray tracing methods for modeling laser cavities has been extensively studied not only in the literature [60] but also at CREOL (so called y-ybar-method) [61]. The latter we applied for our analysis.

In reference [60] it is shown in detail that Gaussian beams may be described by two rays at the waist position, these rays will be called y and ybar ray and have ray heights y and ybar and angles with the optical axis u and ubar. For a Gaussian beam of waist w_0 at the position z=0, the parameters are:

$$y = w_0, \qquad u = 0, \qquad \bar{y} = 0, \qquad \bar{u} = \frac{\lambda}{\pi w_0}. \tag{7.1}$$

These rays propagate according to the paraxial ray tracing equations, they obey e.g. the equation

$$\begin{pmatrix} y' \\ n'u' \end{pmatrix} = \begin{pmatrix} A & B \\ C & D \end{pmatrix} \begin{pmatrix} y \\ nu \end{pmatrix}. \tag{7.2}$$

Reproduced with permission of the copyright owner. Further reproduction prohibited without permission.

Equation (7.2) is valid for both y and ybar rays.

The Gaussian beam parameters are then deduced by the following formulae:

$$w = \sqrt{y^2 + \overline{y}^2}$$

$$R = \frac{y^2 + \overline{y}^2}{yu + \overline{yu}} \qquad (7.3)$$

The problem of finding the eigenmodes remains to be solved: from the y-ybar-method the radius of curvature R of the wavefront may be determined. If the curvature of the mirror equals exactly the curvature of the wavefront, the cavity is automatically resonant, as the beam is reflected back along its own path. Thus the radius of the curvature of the last mirror in a cavity has to be equal exactly the radius of curvature of the wavefront at that position. For a given mirror radius the position where the curvature of the wavefront equals that of the mirror has to be determined.

7.3.2. Modeling of 3-mirror V-shaped cavity of Cr:LiSAF laser

The goal of the simulation is to determine for different spot sizes of the fundamental beam on the flat mirror, which correspond to the first waist of the laser mode, and for different radii of curvature and positions of the folding mirror:

1) the size and position of the beam waist between two curved mirrors (second waist);

Reproduced with permission of the copyright owner. Further reproduction prohibited without permission.

2) the required radius of curvature or the position of the last mirror (in order to make the cavity resonant and stable).

For this task the y and ybar beams were defined according to the Eq. 7.1., i.e. the height of the y-ray corresponds to the waist w_0 and the angle of the ybar ray corresponds to $\lambda/\pi w_0$. These rays were then numerically "propagated" using a paraxial table, from these data the waist and radius of curvature of the beam were computed.

Figure 87 shows the results of the simulation, the Gaussian beam (red) and the y-ray (green) and ybar-ray (blue) are depicted.

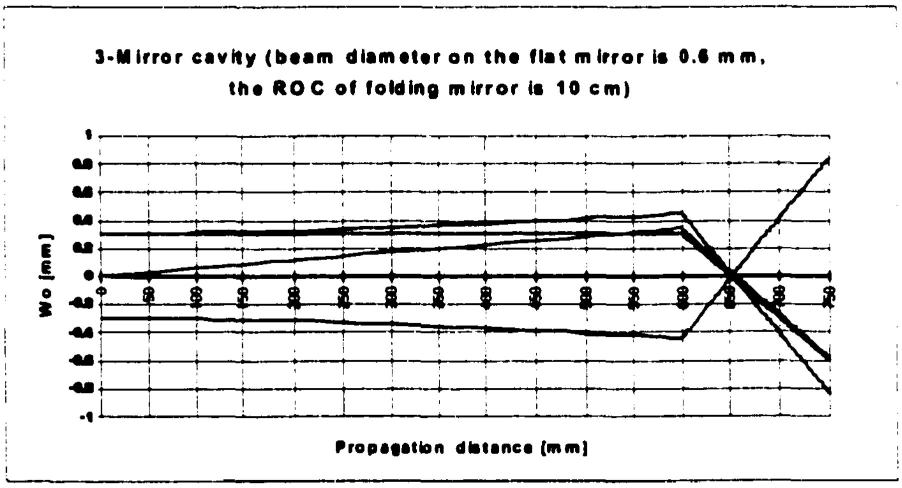

Figure 87. Gaussian beam propagation in a three-mirror V-shaped cavity.

The simulations were done for different waist sizes on the flat mirror and for three different folding mirror radii of curvature (100, 50 and 10 cm), one of which (10 cm) corresponded to actual ROC of folding mirror used in the experiment. A LiSAF rod length of 80 mm was assumed, the distance from the flat mirror to the first curved mirror was 600 mm, the wavelength 888 nm. Effects due to the tilt of the folding

Reproduced with permission of the copyright owner. Further reproduction prohibited without permission.

mirror are neglected. Our experiments and the modeling with PARAXIA software show that for small folding angles (up to 20° between the two optical axes) the effects to the Gaussian beam are negligible.

We obtained the following results:

1) For smaller radius of curvature of the folding mirror, i.e. a bigger power of this mirror, the spot size at the waist gets smaller;

2) The smaller the initial spot size on the flat mirror, the bigger the spot size at the second waist between two concave mirrors;

3) For big initial spot size on the flat mirror, the waist occurs nearly at the focus of the folding mirror. The smaller the spot size at the flat mirror gets, the farther the waist is away from the focus of the folding mirror;

4) The radius of curvature of the wavefront that determines the radius of the second mirror increases almost linearly with distance from the folding mirror.

In our 3-mirror V-shaped resonator the beam size on the flat mirror was determined by the aperture of the laser rod in most of cavity configurations. In some cases, an intracavity aperture was positioned close to the flat mirror of the resonator in order to eliminate higher order transverse modes. This aperture allowed the adjustment of the beam diameter on the flat mirror within the range from 0.5 mm to 6 mm. The aperture was not tightly closed, though, so that the output energy will not be reduced significantly.

In our 3-mirror V-shaped resonator, the folding mirror had a radius of curvature of 10 cm, which combined with relatively big beam diameter on the flat mirror (in the long arm of the resonator), led to very tight focusing of the beam in the short arm of the resonator. For Gaussian mode approximation the calculated spot size in the waist

Reproduced with permission of the copyright owner. Further reproduction prohibited without permission.

between two concave mirrors for central mode was couple of tens of microns. The value of two Rayleigh ranges $2z_0$ was ~2mm, which is much shorter than 8mm length of the nonlinear crystal. Both: the convergence and divergence angles between two concave mirrors were an order of magnitude higher than the acceptance angle of LBO. All of these factors have contributed to the limited efficiency of intracavity SHG and to the degradation of the optical contact of fused silica windows to LBO crystal.

In order to successfully implement the intracavity frequency doubling in our Cr:LiSAF laser we suggest to perform some modifications of the cavity. First of all, we need to replace currently available folding mirror with ROC of 10 cm with another one with longer ROC. Correspondingly, the length of the arm between concave mirrors will be longer. With new mirror the beam waist will be not as tight as with 10 cm ROC folding mirror, and the Rayleigh range will be longer than the length of nonlinear crystal, which will result in improvement of efficiency of intracavity frequency doubling. The last curved mirror with 10 cm ROC could still be used by positioning it at a distance where the radius of wavefront curvature is also 10 cm.

7.4. The Pr:YLF laser at 640 nm pumped by the intracavity frequency doubled flashlamp pumped Cr:LiSAF laser

Pr:YLF is a promising laser source because it offers visible emission from a solid state laser. In 1977, Esterowitz et al. [62] measured stimulated emission at 640 nm ($^3P_0$-$^3F_2$) in a 0.2% Pr:YLF sample pumped by a pulsed dye laser. Four-level operation results in a low threshold for stimulated emission. However, direct flashlamp pumping yields unacceptably low slope efficiencies (.014%) [45], due to the poor spectral overlap

Reproduced with permission of the copyright owner. Further reproduction prohibited without permission.

between the broadband pump light and narrow Pr^{3+} absorption. Therefore, radiation of the intracavity frequency doubled Cr:LiSAF laser at 444 nm was used for the efficient pumping of the Pr:YLF laser.

7.4.1. Polarized absorption and emission spectra of Pr:YLF

Esterowitz et al. reported detailed study of absorption and emission in Pr:YLF; exact energies and crystal field parameters can be found in [63].

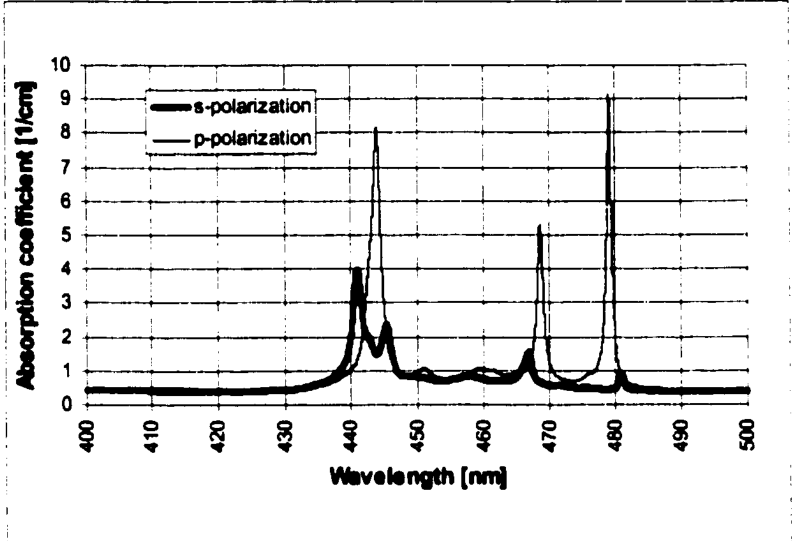

Figure 88. Polarized absorption spectrum of the 3% Pr:YLF.

We performed spectroscopic measurements of absorption and emission of 3% Pr:YLF crystal used for fabrication of laser material. The polarized absorption spectrum of Pr:YLF is shown on the Figure 88. The strongest absorption peak around 444 nm is for the polarization parallel to the c-axis of the Pr:YLF crystal. The absorption coefficient at 444 nm in 3% concentration sample is about 8 cm^{-1}.

The polarized emission spectra of Pr:YLF are shown in Figure 89. The 640 nm emission line is present only in the spectrum of σ - polarized light and corresponds to $^3P_0$-

Reproduced with permission of the copyright owner. Further reproduction prohibited without permission.

$^3F_2$ transition. The emission cross section at 640 nm was found to have the value of 10^{-18} cm^2. The room temperature lifetime of upper level $^3P_0$ of 640 nm transition is reported in [45]: it is 50 μs for 0.2% and 30 μs for 1.2% of Pr:YLF.

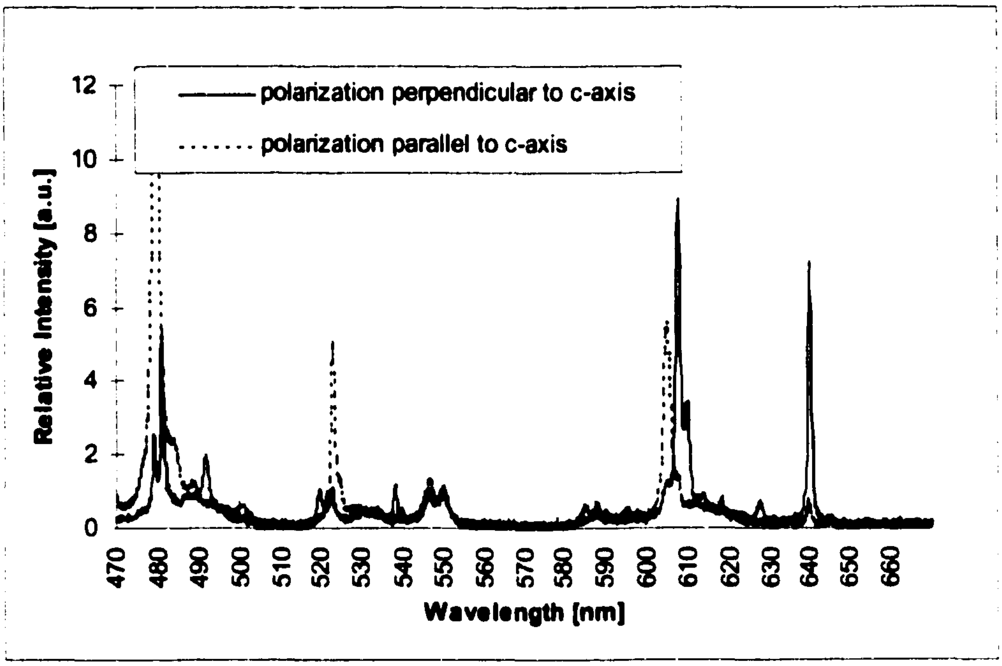

Figure 89. Polarized emission spectrum of Pr:YLF.

7.4.2. Cavity layout of Pr:YLF laser

In the following experiment we used blue radiation at 444 nm from intracavity frequency doubled Cr:LiSAF laser with BRF for pumping of Pr:YLF laser and obtained lasing at 640 nm. The 3 mm thick Pr:YLF laser crystal is coated on one surface for high reflection at 640nm and high transmission at 440 nm. The output coupler available for this experiment was a partial reflector R=98% at 640 nm with radius of curvature 10 cm. It had a meniscus shape in order to decrease the divergence of the emerging laser beam. The output coupler was mounted on a gimbal mount which was in turn mounted to a one dimensional translation stage in order to allow for proper adjustment of the length of the

Reproduced with permission of the copyright owner. Further reproduction prohibited without permission.

Pr:YLF cavity. This had ensured the control of the spatial overlap of the cavity mode within the crystal. The laser operation was achieved in the fundamental TEM_{00} mode with a low threshold (Figure 90). With the optimal output coupling, we expected to achieve the efficiency of laser similar to reported earlier in the reference [55] with 10 mJ of pump energy at 442 nm, 4mJ at 640 nm was achieved with corresponding slope efficiency of 44%. Therefore we were concerned only about the possibility of operating the Pr:YLF laser in single frequency mode.

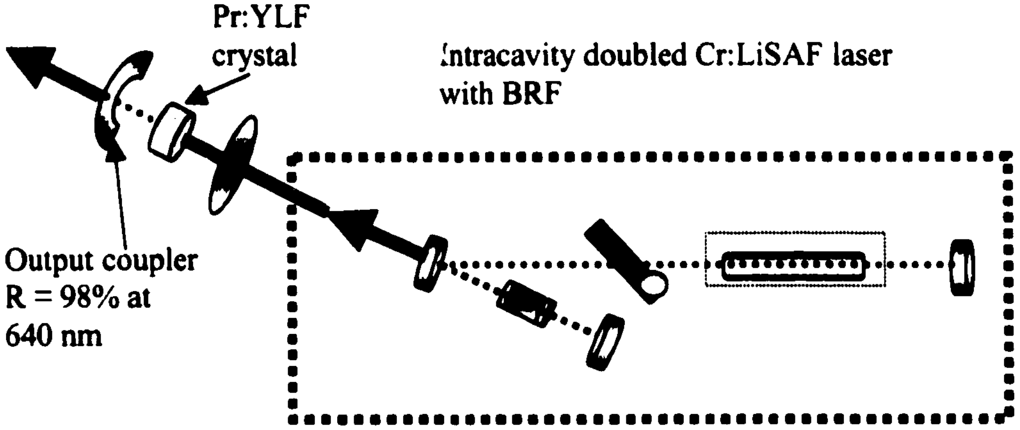

Figure 90. Cavity layout of Pr:YLF laser pumped by intracavity frequency doubled Cr:LiSAF laser.

7.4.3. Single frequency operation of the Pr:YLF laser: design suggestions and tests

Coherence length of lasers for holography is an important parameter, since it determines the allowable path length difference for a given hologram brightness. In order to achieve maximum coherence length of the Pr:YLF red laser, single frequency

Reproduced with permission of the copyright owner. Further reproduction prohibited without permission.

operation of the laser has to be established. Following methods of single frequency operation or their combinations could be used for our Pr:YLF laser:

a) Interferometric mode selection:
   - Fabry-Perot etalon "microchip" laser;
   - Intracavity tilted etalon;
   - Resonant reflector output coupler;

b) Injection seeded oscillator;

c) Traveling wave unidirectional ring laser.

From these methods of achieving laser oscillation in single frequency regime we've selected two ways, which were suitables for our system. Here we present the results of analysis for I) Fabry-Perot etalon "microchip" laser and II) intracavity tilted etalon.

The first method for achieving single frequency operation is following: by significantly reducing the length of the Pr:YLF laser cavity to make free spectral range (FSR) big enough, so that only few modes will oscillate within the emission line. To achieve this we were planning to use so called microchip Pr:YLF lasers (or Fabry-Perot etalon lasers).

The whole cavity consists of thin slab of gain medium coated on both sides (Figure 91). We've performed calculations for several different thicknesses of the microchip laser: 0.5mm, 1mm, 2mm.

According to calculations the 500 micron Pr:YLF crystal will absorb the 33% of pump light at 444 nm (the absorption coefficient is ~8 cm^{-1}). The width of the emission line at 640 nm in Pr^{3+} is about 1 nm or 24.4 cm^{-1}. The free spectral range of 500 micron

Reproduced with permission of the copyright owner. Further reproduction prohibited without permission.

Pr:YLF laser will be ~6.9 cm^{-1}, which means that there will be ~3 modes oscillating within the emission line (or less, considering that the gain curve will be narrower than emission line) (Figure 92). Up to a certain pump power we should be able to get single frequency output.

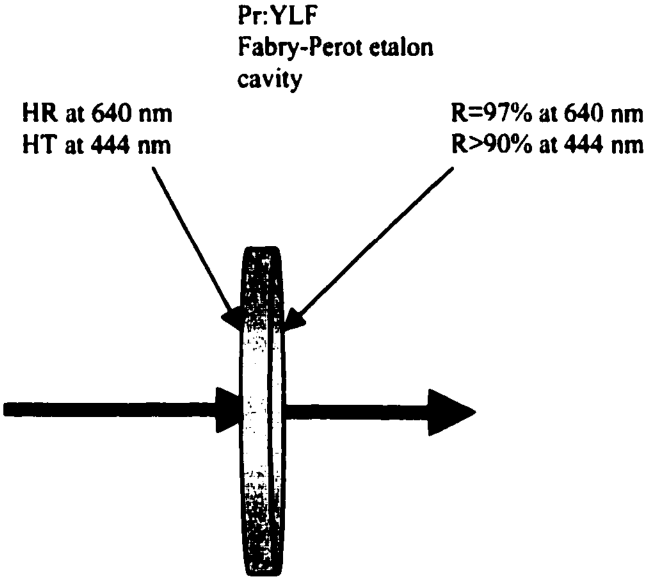

Figure 91. Pr:YLF Fabry-Perot etalon laser.

The linewidth will be determined by the choice of finesse of the etalon. For example, with the HR coating at 640 nm on one side and R=83% coating on the other side of the 0.5 mm thick crystal, the linewidth of selected mode will be ~0.2 cm^{-1} which corresponds to coherence length of 3.2 cm. In order to achieve even narrower line ~0.1 cm^{-1} (6.4 cm coherence length) the reflectivity of coating on the second side has to be

Reproduced with permission of the copyright owner. Further reproduction prohibited without permission.

R=91%. For coherence length of 10 cm the "output coupler" reflectivity has to be 97%, and for coherence length of 28 cm the "output coupler" reflectivity has to be 99%.

There are several problems to consider while working with microchip laser. The main drawback with this approach is that it is not scalable to higher energies. Another important issue is to find some way to eliminate higher order transverse modes, since every transverse mode has its own set of longitudinal modes. In this case the pump spot size can be used as a limiting aperture. By picking a pump spot size smaller than fundamental TEM_{00} mode size we can achieve the operation of the laser in the single spatial mode.

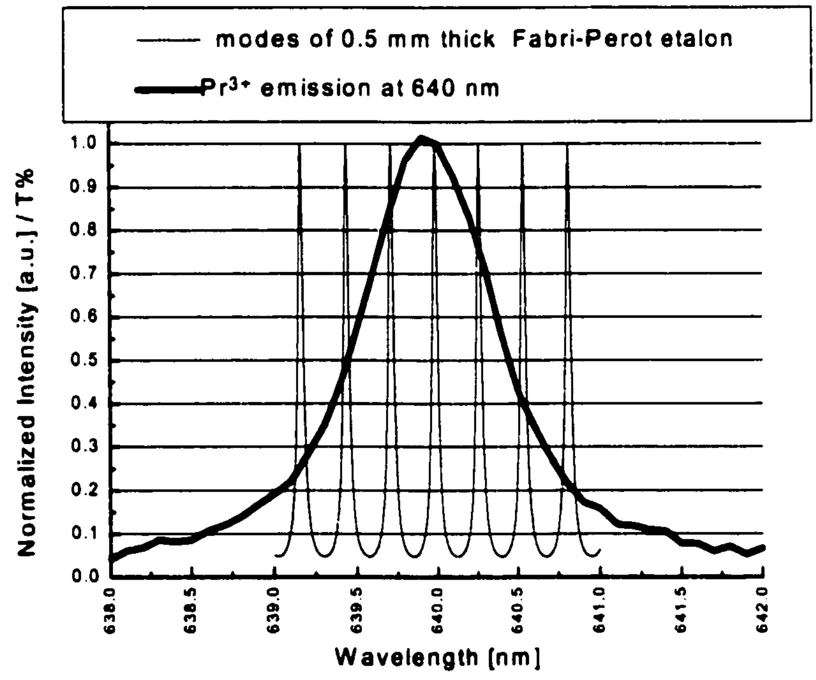

Figure 92. Emission line of Pr^{3+} at 640 nm and modes of 0.5 mm thick Fabry-Perot etalon.

Reproduced with permission of the copyright owner. Further reproduction prohibited without permission.

In order to keep the flat/flat 0.5 mm long Pr:YLF cavity configuration stable and the size of TEMoo mode reasonably small, thermal lensing in the material has to be induced. This might require the laser operation at higher repetition rate than 2 Hz. The YLF crystal has demonstrated the positive thermal lens ~150 m in σ-polarization (direction perpendicular to the optical axis of the crystal) and negative lens –60 m in the direction parallel to the optical axis of the crystal. The emission line at 640 nm is present only in σ polarization, so it will experience slight focusing by the positive lens. Our calculations of the resonator parameters with the account of the thermal lensing have given reasonable value of the TEM_{00} mode spot size of ~250 μm, which is very easy to match with the pump spot size.

The second approach for achieving single frequency operation is the insertion of the tilted Fabry-Perot etalon in the cavity of the Pr:YLF laser. The cavity should consist of the 3 mm Pr:YLF crystal that we already described and the output coupler (Figure 93). The 3 mm Pr:YLF crystal provides 97% absorption of the pump. The coating on the front surface of the crystal (HR at 640 nm and high transmission at 440 nm) serves as an entrance mirror of the laser. The AR coating at 640nm on the other side of the crystal will prevent it from acting as an etalon within another etalon in the laser cavity, since coupled etalons will create all kinds of transmission resonances and their beat modes, and it will make the task of achieving single frequency operation even more difficult. In order to insert the etalon in the collimated beam we were planning to use flat output coupler. If stability of the cavity was a problem, then the curved output coupler with long radius of curvature (~1m) had to be used in order to obtain quasi flat wavefront in the cavity.

Reproduced with permission of the copyright owner. Further reproduction prohibited without permission.

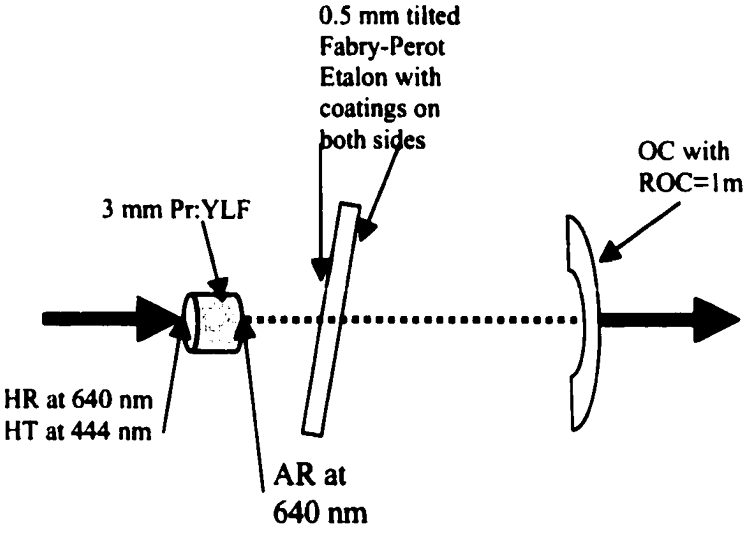

Figure 93. Pr:YLF laser cavity with intracavity tilted etalon.

As we mentioned above, the width of the emission line at 640nm in Pr^{3+} is about 1 nm or 24.4 cm^{-1}. The calculations of spectral characteristics of the laser cavity with the intracavity tilted etalon were performed for 5 cm long cavity. The free spectral range (FSR) for that cavity is ~0.1 cm^{-1} or 0.004 nm, which means that there are about 244 longitudinal modes oscillating in the cavity. Three different etalons were considered with thicknesses 0.5mm, 0.4mm, and 0.25mm. For the 0.5 mm thick etalon we obtained FSR of 6.9 cm^{-1} or 0.273 nm (~3-4 modes will oscillate within the emission line). For the 0.4 mm thick etalon we obtained FSR of 8.33 cm^{-1} or 0.341 nm (~2-3 modes will oscillate within the emission linewidth). For the 0.25 mm thick etalon we obtained FSR of 13.3 cm^{-1} or 0.546 nm (~1-2 modes will oscillate within the emission linewidth). By setting the condition on the width of the single line (it has to be equal to two FSR of the base laser cavity ~0.2 cm^{-1}) we can find the values of the reflectivities of the coatings on both

Reproduced with permission of the copyright owner. Further reproduction prohibited without permission.

sides of etalons. According to calculations, for the 0.5mm thick etalon the reflectivity should be R=91%, for 0.4mm etalon – R=92% and for 0.25 etalon R=95%. The decrease in the laser cavity length will significantly affect the values of the reflectivities. For example if 0.4 mm etalon is inserted in the 2.5 cm cavity (as opposed to 5 cm), then the required reflectivity of coatings on both sides will be lower ~85%.

The third approach to solving the problem of single frequency operation of Pr:YLF laser is combination of two previous approaches. We could use small portion of the blue beam for pumping the thinnest 0.5 mm Fabry-Perot Pr:YLF etalon laser. Due to low pump energy it will operate very close to the threshold, hence allowing single longitudinal mode oscillation within the gain curve at 640 nm. The weak single frequency radiation at 640 nm from Fabry-Perot Pr:YLF etalon laser can later be seeded into the main oscillator with 3 mm thick Pr:YLF active medium enabling its operation in single frequency regime.

For actual testing of discussed design suggestions we had only parts available for Fabry-Perot etalon lasers. Three Pr:YLF Fabry-Perot etalon laser slabs were fabricated: 0.5, 1, 1.5 mm thick. All of them were coated on both sides. The pump entrance side coating was high reflective >99.8% at 640 nm and high transmissive at 444 nm. The "output coupler" side coating was 97% reflective at 640 nm for the extraction of the laser radiation, and R>90% at 444 nm for the double pass of the pump beam in the gain medium (since the absorption of the pump in thin etalon might not be enough in single pass geometry).

Laser action was achieved for the thickest 1.5 mm etalon with rather big transverse mode. The measurements of coherence length of 1.5 mm Pr:YLF slab laser

Reproduced with permission of the copyright owner. Further reproduction prohibited without permission.

showed that the coherence length of the laser was about 4.2 cm at pump energies of about 10 mJ at 444 nm. With decreasing pump energy and allowing Pr:YLF slab laser operation slightly above threshold, we achieved coherence length of about 56 cm.

7.4.4. Interferometric measurements of coherence length of the Pr:YLF laser at 640 nm

The temporal coherence of a laser is defined as a path length difference over which the radiation can still interfere with itself. From the common techniques for measuring spectral bandwidth or coherence length of lasers, we selected the Michelson interferometer (Figure 94).

The output of the Pr:YLF laser at 640 nm is directed to a 50% reflective beam splitter under a 45° angle. The beam splitter is a 3° wedge, which allows to avoid the interference from plane-parallel surfaces. One part of the incident 640 nm radiation beam passes through the beam splitter and the second part is reflected at 90° relative to the incident beam. Both beams after reflection from the mirrors #1 and #2 are brought together through the beam splitter to form an interference pattern. One of the back reflecting mirrors is placed on the translation rail, which changes the optical path length difference.

The coherence length is defined as the path length difference for which fringe visibility in a Michelson interferometer is reduced to $1/2^{1/2}$ (laser manufacturers sometimes use the 1/2 or $1/e^2$ levels). The fringe visibility of an interferometer is defined as: $V = (I_{max} - I_{min})/(I_{max} + I_{min})$.

Reproduced with permission of the copyright owner. Further reproduction prohibited without permission.

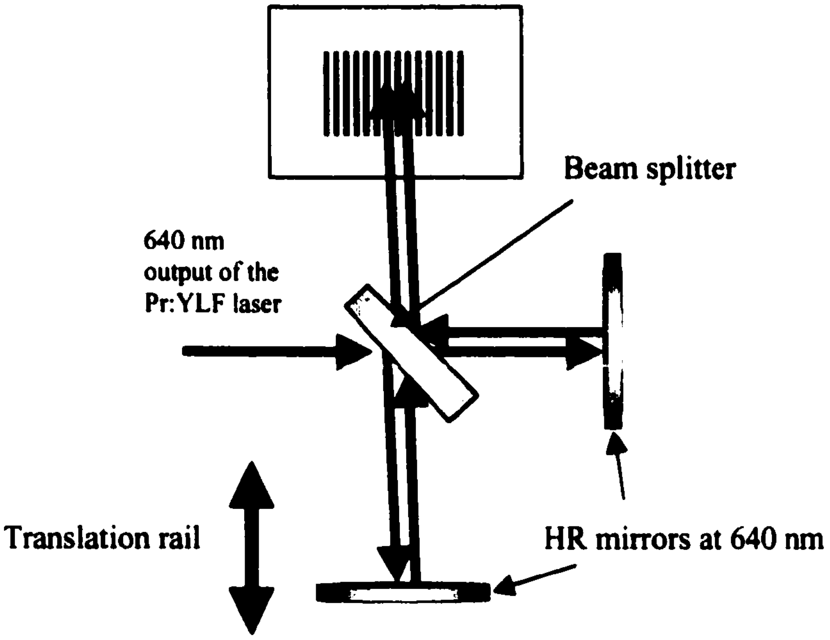

Figure 94. Michelson interferometer for coherence length measurement.

In Figure 95 and Figure 96, we demonstrate the interference patterns and corresponding intensity profiles of those patterns generated by the 640 nm radiation from Pr:YLF laser measured at different optical path length difference ΔL. For $\Delta L = 50$ cm, the measured fringe visibility is reduced to $1/e^2$ of its maximal value at $\Delta L = 0$.

Reproduced with permission of the copyright owner. Further reproduction prohibited without permission.

ΔL = -2 cm ΔL = 0 cm ΔL = 2 cm

ΔL = 10 cm ΔL = 15 cm ΔL = 20 cm

ΔL = 30 cm ΔL = 40 cm ΔL = 50 cm

Figure 95. The interference patterns with 640 nm Pr:YLF laser radiation obtained with Michelson interferometer.

Reproduced with permission of the copyright owner. Further reproduction prohibited without permission.

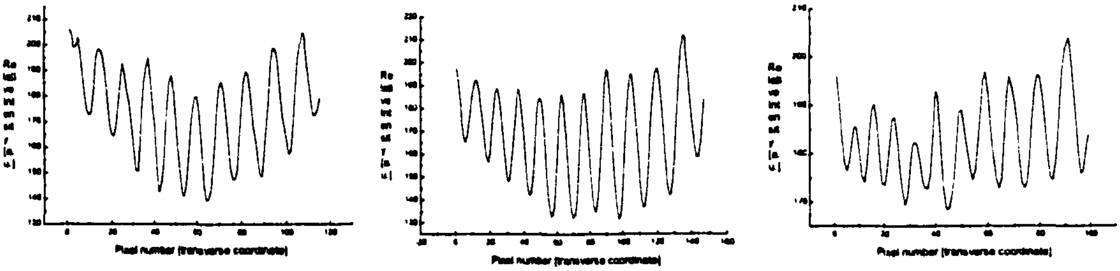

ΔL = -2 cm ΔL = 0 cm ΔL = 2 cm

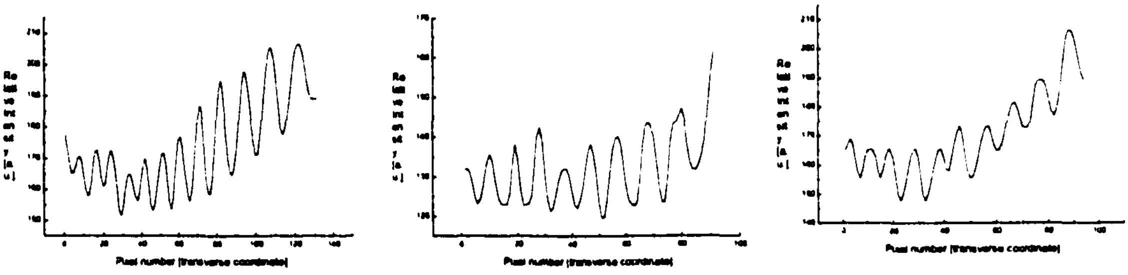

ΔL = 10 cm ΔL = 15 cm ΔL = 20 cm

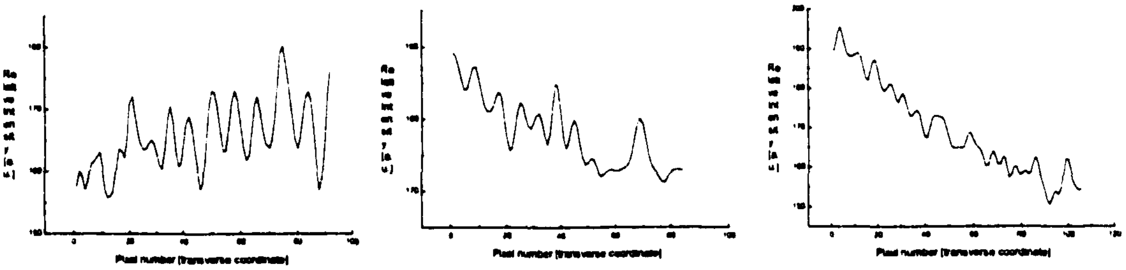

ΔL = 30 cm ΔL = 40 cm ΔL = 50 cm

Figure 96. Intensity profiles of interference patterns shown in Figure 95.

Reproduced with permission of the copyright owner. Further reproduction prohibited without permission.

CHAPTER 8. CONCLUSIONS

This dissertation has presented the results of series of experiments and theoretical studies, which led to the development of two new solid state laser systems: efficient, room temperature mid-infrared solid state laser at 3.9 μm in Ho^{3+} doped BaY_2F_8 and visible Pr:YLF laser at 640 nm for holography.

We presented the results of spectroscopic evaluations and numerical modeling of energy transfer processes between rare earth ions of Ho^{3+} doped in two host laser materials: BaY_2F_8 and $LiYF_4$. Three different pumping and lasing schemes of the 3.9 μm laser have been suggested and studied.

First, cascade laser action at 1.4 μm and 3.9 μm was achieved with low thresholds and near-theoretical quantum efficiency in Ho^{3+} doped BaY_2F_8 pumped at 532 nm by a Q-switched frequency doubled Nd:YAG laser.

Next, we studied the feasibility of achieving 3.9 μm laser with cw resonant cascade pumping at 750 nm by a Ti:Sapphire laser, by taking advantage of a fortuitous coincidence of ground state absorption and excited state absorption, combined with the strong cross-relaxation processes in high concentration samples. Along with theoretical model calculations we performed Z-scan measurements of nonlinear transmission and fluorescence for monitoring the population redistribution on Ho^{3+} energy levels upon pumping with cw radiation at 750 nm. New energy transfer processes, such as

Reproduced with permission of the copyright owner. Further reproduction prohibited without permission.

upconversion and excited state absorption from terminal level of 3.9 μm laser were observed in high concentration Ho^{3+} doped BaY_2F_8. These processes can reduce effective lifetime of the lower laser level $^5I_6$ of 3.9 μm transition thereby breaking the bottleneck at that level and possibly allowing mid infrared laser oscillation with cw pumping at 750 nm. Therefore, the strong upconversion process from $^5I_6$ level in high concentration Ho:BYF, experimentally discovered in this work, needs further characterization. First of all, the suggested path of upconversion: simultaneous transitions $^5I_6$ - $^5G_6$ and $^5S_2$ - $^5I_7$, has to be verified. Second, the measurements of upconversion rates have to be performed. Numerical model for Ho:BYF has to be upgraded by adding new terms (due to upconversion) into system of rate equations, and the results of theoretical calculations have to be compared to the results of Z-scan experiments.

We have developed a theory of reverse saturable absorption that allows determining the nonlinear absorption coefficients, which can be used for evaluation of populations of Ho^{3+} energy levels involved in the cascade resonant absorption process, and in particular – for evaluation of population of the first excited state $^5I_7$, under strong pumping at 750 nm.

Based on the results of experimental measurements of fluorescence transients from Ho^{3+} energy levels and theoretical calculations of population dynamics, we proposed to use flashlamp pumped tunable Cr:LISAF laser with up to 1 J energy in 50 μs long pulse for the direct pumping of the upper level of the 3.9 μm laser. Pulsed laser oscillation at 3.9 μm is demonstrated for Ho^{3+} in BaY_2F_8 pumped at 890 nm with low

Reproduced with permission of the copyright owner. Further reproduction prohibited without permission.

threshold of 3 mJ. A slope efficiency of 14.5% was achieved with maximal energy of 30 mJ of the 3.9 μm laser pulse.

Two linear down conversion schemes of 3.9 μm Ho:BYF laser with pulsed resonant pumping at 532 nm and 890 nm have demonstrated very low thresholds and high slope efficiencies. We expect significant improvement of the efficiency of 3.9 μm laser by further optimization of key cavity parameters. The value of threshold with the knowledge of pump energy and cavity parameters, allowed to estimate the order of the magnitude of stimulated emission cross section at 3.9 μm, which according to our calculations is quite high – it is greater than $9.8 \cdot 10^{-20}$ cm^2. More accurate value of $\sigma_{5I5 \rightarrow 5I6}$ emission cross section can be measured with spectroscopic methods.

As we mentioned before, the 890 nm pumping results in sequential ground state absorption $^5I_8$ - $^5I_5$, and excited state absorption $^5I_5$ – $^5G_6$. The excited state absorption (ESA) from $^5I_5$ level is not characterized yet. However, the knowledge of the cross section of ESA is very important for the design and optimization of the 3.9 μm laser, since it will allow to estimate the degree of depletion of the upper level of 3.9 μm laser due to ESA.

In the last part of the thesis, we described the design suggestions and the development of the visible Pr:LiYF$_4$ laser for holography at 640 nm resonantly pumped by the frequency doubled flashlamp pumped tunable Cr:LiSAF laser at 444 nm.

Reproduced with permission of the copyright owner. Further reproduction prohibited without permission.

APPENDIX 1. INSTRUMENT DRIVER FOR AUTOMATED CONTROL OF 0.3 M MCPHERSON SPECTROMETER WITH REAL TIME DATA ACQUISITION

Reproduced with permission of the copyright owner. Further reproduction prohibited without permission.

We used graphical programming language LabVIEW to program the instrument driver for automated control of 0.3 m McPherson spectrometer with simultaneous real time data acquisition. The control board "pcStep –4A" from nu-Logic Inc. was used for driving stepper motor (Superior Electric), installed in McPherson spectrometer. The pc-Step is a 2-axis stepper motor control board providing high performance motion control for ISA bus based IBM compatible computer systems. It offers output step rates of up to 750,000 steps per second to easily handle full step half step and microstep applications. All setup and motion control functions are implemented using device driver commands, callable from LabVIEW virtual instruments (VI-s).

The front panel of the instrument driver for automated control of 0.3 m McPherson spectrometer with simultaneous real time data acquisition is depicted in Figure 97. Here is the brief description of features of this virtual instrument. It has several terminals for input parameters: such as "Start wavelength", "Stop wavelength", "Wavelength increment", and "Average scan speed". The output terminals are: 1) waveform chart, that allows to view the data in real time as they are acquired, 2) waveform graph, which displays complete spectrum as a function of wavelength after the scan is finished, 3) "current wavelength" indicator, and 4) two-dimensional array of data, acquired in the experiment. At the beginning of each scan the monochromator first drives to "start wavelength" at a high speed of 5 nm/s. To avoid the backlash problem monochromator is programmed first to stop at the wavelength, which is 5 nm below of "start wavelength" and then to move slowly (0.1 nm/s) to the beginning of scan range. The motor pauses for a second at the "start wavelength" to indicate the beginning of scan.

Reproduced with permission of the copyright owner. Further reproduction prohibited without permission.

Then actual recording of spectrum starts. The McPherson instrument driver provides the ability to control motion in absolute or relative position modes, update maximum velocity and acceleration as required and read axis position and status from the return data buffer. This instrument driver works in stepwise manner. It first moves the monochromator to wavelength increment and reads the position of stepper motor to make sure that the monochromator has reached the specified wavelength. Then it initializes the National Instruments AT-MIO-16XE-50 data acquisition board, and acquires certain number of data points (100 points in our case) with precise timing, controlled by hardware clock. The program averages all 100 points and displays the resulting point on the waveform chart, and at the same time it records that point in two-dimensional array next to corresponding wavelength. The program drives then the monochromator to the next wavelength, and performs data acquisition as in previous step. In this manner, the McPherson instrument driver covers specified wavelength range and records the spectrum. When the scan is finished, the program saves the data into text files, readable by most spreadsheet applications (MicroCal Origin, Microsoft Excel, etc).

Reproduced with permission of the copyright owner. Further reproduction prohibited without permission.

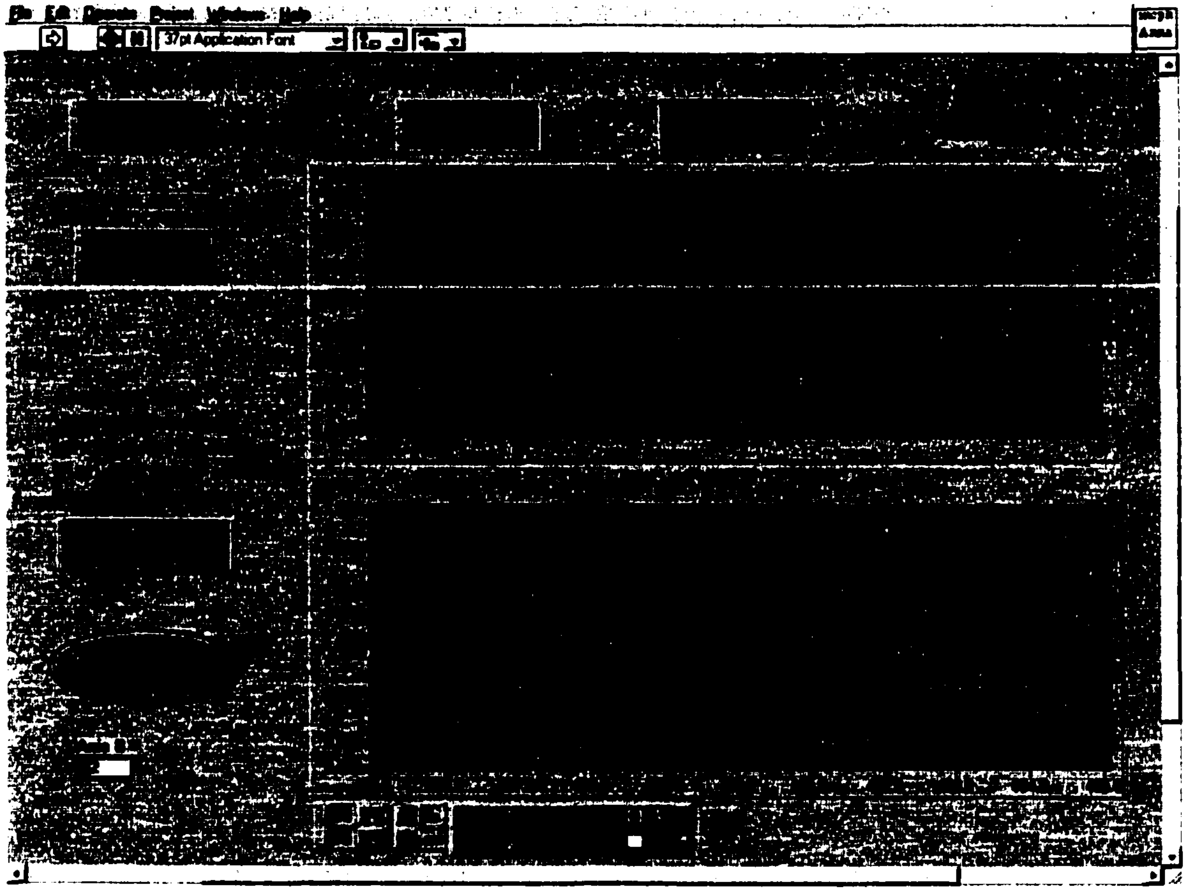

Figure 97. Front panel of Labview instrument driver for automated control of 0.3 m McPherson spectrometer with real time data acquisition.

Reproduced with permission of the copyright owner. Further reproduction prohibited without permission.

APPENDIX 2. LABVIEW INSTRUMENT DRIVER FOR SPEX SPECTROMETER WITH BUFFERED DATA ACQUISITION

Reproduced with permission of the copyright owner. Further reproduction prohibited without permission.

Labview instrument driver for SPEX spectrometer was programmed to acquire the specified amount of data from analog input channel of National Instruments AT-MIO-16XE-50 data acquisition board upon receiving the digital trigger signal. The front panel of the instrument driver for SPEX spectrometer is depicted in Figure 98. This instrument driver performs timed acquisition, meaning that a hardware clock is used to control the acquisition rate for fast and accurate timing. The data acquisition is buffered: the data is stored in an intermediate memory buffer after it is acquired from the analog input channel. The instrument driver retrieves all the data from the memory buffer and displays it after the acquisition is finished.

Special interface SPEX minidrive performs precise wavelength control of SPEX monochromators. The values of input parameters: start wavelength, stop wavelength, and scan speed have to be entered with keypad on minidrive. The same parameters have to be set through controls of instrument driver for SPEX spectrometer. In the beginning of each run, this VI waits for the trigger to occur. The trigger signal comes from minidrive, thus synchronizing the beginning of data acquisition and wavelength scan. When acquisition is finished, the program displays all the data from the buffer on the waveform graph, and fills two-dimensional voltage array. The data can be saved in form of spreadsheets. If necessary, the additional information about each particular scan can be saved in the same file with the data.

Reproduced with permission of the copyright owner. Further reproduction prohibited without permission.

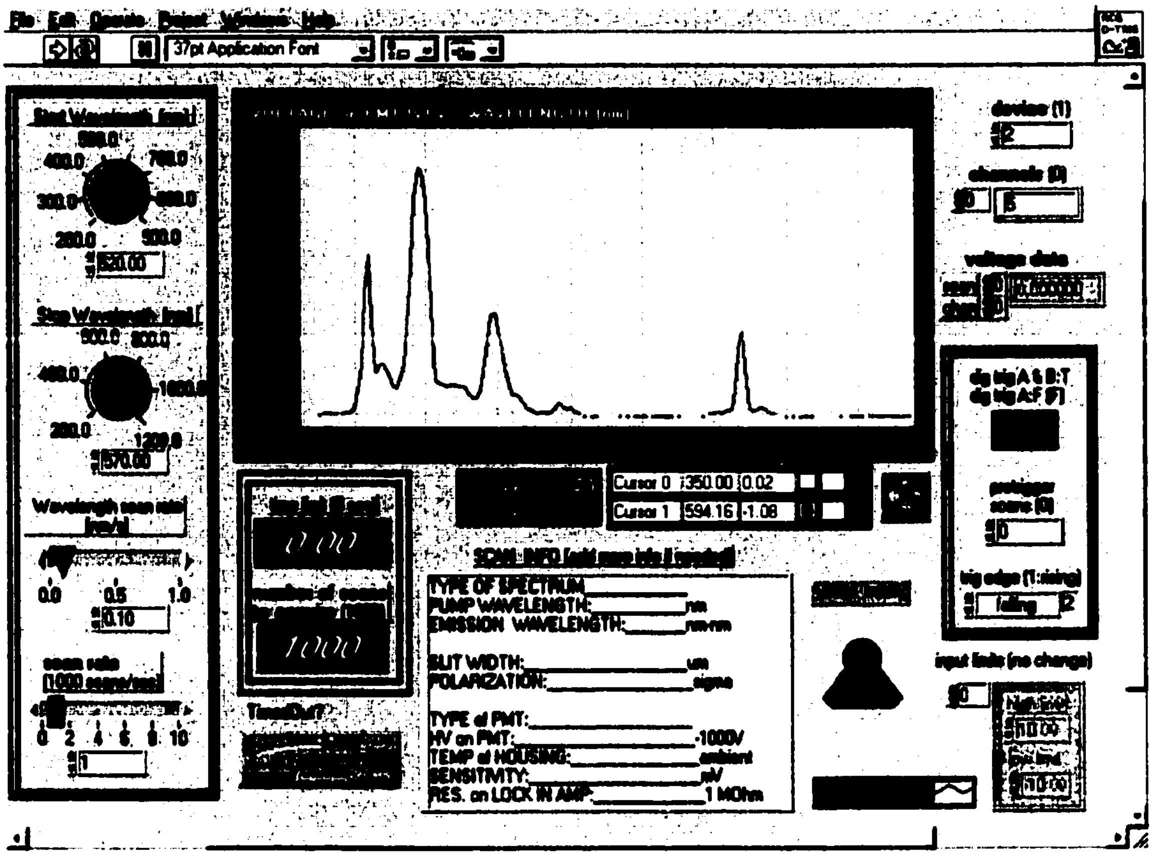

Cursor 0 350.00 0.02
Cursor 1 594.16 -1.08

TYPE OF SPECTRUM
PUMP WAVELENGTH:________nm
EMISSION WAVELENGTH:________nm-nm

SLIT WIDTH:________um
POLARIZATION:________sigma

TYPE of PMT:________
HV on PMT:________-1000V
TEMP of HOUSING:________ambient
SENSITIVITY:________uV
RES. on LOCK IN AMP:________1 MOhm

Figure 98. Front panel of Labview instrument driver for SPEX spectrometer with buffered data acquisition.

Reproduced with permission of the copyright owner. Further reproduction prohibited without permission.

LIST OF REFERENCES

---

1. S. Hufner, "Optical spectra of transparent rare earth components," Academic Press, New York, 1978.
2. G.H. Dieke, "Spectra and energy levels of rare-earth ions in crystals," Wiley Science, New York, 1968.
3. W.D. Partlow and H.W. Moos, "Multiphonon relaxation in $LaCl_3$:Nd^{3+}" *Phys. Rev.*, vol. 157, pp. 252-256, 19674.
4. J.H. Van Vleck, "The puzzle of rare-earth spectra in solids," *J. Phys. Chem.*, vol. 41, pp. 67-80, 1937.
5. L.A. Riseberg and M.J. Weber, "Relaxation phenomena in rare-earth luminoscence", in *Progress in Optics*, vol. 14, p. 91, E. Wolf, ed., North Holland, New York, 1976.
6. T. Forster, "Inytermolecular energy transfers and fluorescence," *Ann Physik*, vol. 2 (1,2), pp. 55-75, 1948.
7. D.L. Dexter, "A theory of sensitied luminoscence in solids," *J. Chem. Phys.*, vol. 21, pp. 863-870, 1953.
8. M. Inokuti, H. Hirayama, "Influence of energy transfer by the exchange mechanism on donor luminoscence," *J. Chem Phys.*, vol. 43, pp. 1978-1989, 1965.

Reproduced with permission of the copyright owner. Further reproduction prohibited without permission.

9. R.K. Watts, in Optical Properties of Ions in Solids, p.307, B. DiBartolo, ed., Plenum Press, New York, 1975.

10. J.E. Bernard, D.E. Berry, and F. Williams, in Energy Transfer Processes in Condensed Matter, p. 1, B. Dibartolo, ed., Plenum Press, New York, 1984.

11 B. DiBartolo, ibid, p. 103.

12. N. P. Barnes, D. J. Gettemy, N. J. Levinso, J. E. Griggs, "TEM_{00} mode Ho:YLF laser," *Proc. Soc. Photo Opt. Instrum. Eng. SPIE*, vol. 190, pp. 297-304, 1979.

13. L.F. Johnson and H.J. Guggengeim, "Laser emission at 3 μm deom Dy^{3+} in BaY_2F_8," *Appl. Phys. Lett.*, vol. 23 (2), pp. 96-98, 1973.

14. A.M. Morozov, I.G. Podkolzina, A.M. Tkachuk, V.A. Fedorov and P.P. Feofilov, "Lumincescence and induced emission of lithium-erbium and lithium-holmium binary fluorides," *Opt. Spectrosc.*, vol. 39 (3), pp. 338-339, 1975.

15. I.G. Podkolzina, A.M. Tkachuk, V.A. Fedorov and P.P. Feofilov "Multifrequency generation of stimulated emission of Ho^{3+} ion in $LiYF_4$ crystals," *Opt. Spectrosc.*, vol. 40, pp. 111-112, 1976.

16. E.P. Chicklis, C.S. Naiman, L. Esterowitz, and R. Allen, "Deep red laser emission in Ho:YLF," *IEEE Journal of Quantum Electronics*, vol. QE-13, pp. 893-895, 1977.

17 M.G. Knights, W.F. Wing, J.W. Baer, E.P. Chicklis and H.P. Jenssen, „High efficiency deep-red laser pumped by doubled Nd:YAG," *IEEE J. Quantum Electron.*, QE-18, 163, 1982.

Reproduced with permission of the copyright owner. Further reproduction prohibited without permission.

18. L. Esterowitz, R.C. Eckard, and R.E.Allen, "Long wavelength stimulated emission via cascade laser action in Ho:YLF," *Appl. Phys. Lett.*, vol. 35, pp. 236-239, 1979.

19. R. C. Eckart, L. Esterowitz and Y. P. Lee, "Three wavelength laser emission in Ho:YLF via sequential cascade," in *Procs. Int'l Conf. Lasers*, p. 380, 1981.

20. L. Wetenkamp, "Efficient cw operation of a 2.9 μm Ho^{3+}-doped fluorozirconate fibre laser pumped at 640 nm," *Electron. Letters*, vol. 26, pp. 883-884, 1990.

21. T. Sumiyoshi and H. Sekita, "Dual-wavelength continuous-wave cascade oscillation at 3 and 2 mm with a holmium-doped fluoride-glass fiber laser," *Optics Letters*, vol. 23, pp. 1837-1839, 1998.

22. J. Schneider, "Superfluorescent fiber source at 3.9μm in the attenuation minimum of the atmosheric window 3-5μm," *Int. J. Infrared Millim. Waves*, vol. 16, pp. 75-82, 1995.

23. J. Schneider, "Fluoride fibre laser operating at 3.9 μm," *Electron. Lett.*, vol. 31, pp. 1250-1251, 1995.

24. J. Schneider, C. Carbonnier and U. Unrau, "Characterization of a Ho^{3+}-doped fluoride fibre laser with a 3.9-μm emission wavelength," *Applied Optics*, vol. 36, pp. 8595-8600, 1997.

25 A.L. Harmer, A. Linz and D.R. Gabbe, "Fluorescence of Nd3+ in Lithium Yttrium Fluoride," *J. Phys. Chem. Solids*, vol. 30, pp. 1483, 1989.

26 P. Liu,P. , R. Yen, N. Bloembergen, "Two-photon absorption coefficient in uv window and coating materials," Appl. Opt., vol. 18(7), pp. 1015-1018, 1979.

Reproduced with permission of the copyright owner. Further reproduction prohibited without permission.

27. H.P. Christensen, H.P. Jenssen and D.R. Gabbe, "BaY_2F_8 as a host for Ln Ions, I: Optical properties of the crystal and spectroscopic results for Pr, Dy, Ho, and Er doping," Unpublished.

28. A.A. Kaminskii, S.E. Sarkisov, F. Below and H.J. Eichler, "Spectroscpic and laser properties of Er3+-doped monoclinic BaY2F8 single crystals, " *Optical and Quantum Electron.*, vol. 22, pp. 95-?, 1990.

29. O.E. Izotova and V.B. Aleksandrov, "The crystal structure of $BaTm_2F_8$," *Sov. Phys. Doklady.*, vol. 15 (6), 525-526, 1970.

30. M.Born and E. Wolf, *Principles of Optics*, 6th edition, Pergamon, 1980, pp. 667-679, 708 or J.J. Nye, "Physical properties of crystals," Oxford, London, 1960, pp. 3-49, 305-309.

31. W.L. Bond, "Measurememnt of the refractive indices of several crystals," *J. Appl. Phys.*, vol. 36 (5), 1674-1677, 1965.

32. K.M. Dinndorf, D.S. Knowles, M. Gojer, C.J. Taylor, and H.P. Jennsen, "Principal axes transitions in monoclinic crystals, " OSA Proceedings on Advanced Solid State Lasers, vol. 13, pp. 270-274, 1992.

33. M.D. Shinn, W.A. Sibley, M.G. Drexhage and R.N. Brown, "Optical transitions of Er^{3+}-ions in fluorozirconate glasses," *Phys. Rev.* B 27, pp. 6635-6648, 1983.

34 D.E. McCumber, „Einstein relations connecting broadband emission and absorption spectra," Phys. Rev. A, vol. 136, pp. 954-957, 1964.

35. B.F. Aul and H.P. Jenssen, "Vibronic interactions in Nd:YAG resulting in nonreciprocity of absorption and stimulated emission cross sections," *IEEE J. Quantum Electron.*, vol. QE-18, pp. 925-930, 1982.

Reproduced with permission of the copyright owner. Further reproduction prohibited without permission.

36. N. Karayianis, D.E. Wortman and H.P. Jenssen, "Analysis of the optical spectrum of Ho:$^{3+}$ in LiYF$_4$," *J. Phys. Chem. Solids*, vol. 37, pp. 675-682, 1976.

37 S.P. Payne, L.L. Chase, L.K. Smith, W.L. Kway and W.F. Krupke, Infrared cross-section measuremets for crystals doped with Er^{3+}, Tm^{3+}, and Ho^{3+}, IEEE J. Quantum Electron., vol. 28(11), 2619-2630, 1992.

38. K.M. Dinndorf, "Energy transfer between thulium and holmium in laser hosts," Ph.D. Dissertation, MIT 1993.

39. H. Chou, "Energy transfer in codoped Ho, Er:YLF and its potential for improving the efficiency of 3 micron lasers," S.M. Dissertation, MIT, 1983.

40. L.F. Johnson and H.J. Guggenheim, "Electronic- and phonon- terminated laser emission from Ho^{3+} in BaY$_2$F$_8$," *IEEE J. Quantum Electron.*, vol. QE-10, pp. 442-449, 1974.

41. L.O. Chua and P.-M. Lin, in *Computer-Aided Analysis of Electronic Circuits: Algorithms and Computational Techniques*, Prentice Hall, Englewood Cliffs, 1975, p. 30.

42. M. Sheik-Bahae, A.A. Said, T.-H. Wei, D.J. Hagan and E.W. Van Stryland, "Sensitive measurement of optical nonlinearity using a single beam," *IEEE J. Quant. Electron.*, vol. 26 (4), pp. 760-769, 1990.

43. D.S. Knowles and H.P. Jenssen, "Upconversion versus Pr-deactivation for efficient 3 μm lasre operation in Er," *IEEE J. Quant. Electron.*, vol. 28 (4), pp. 1197-1208, 1992.

Reproduced with permission of the copyright owner. Further reproduction prohibited without permission.

44. T.Y. Fan and R.L. Byer, "Modeling and cw operation of a quasi-three-level 946 nm Nd:YAG laser," *IEEE J. Quantum Electron.*, vol. QE-23 (5), pp. 605-612, 1987.

45. D. S. Knowles, Z. Zhang, D. Gabble, H.P. Jenssen, "Laser action of Pr^{3+} in $LiYF_4$ and spectroscopy of Eu^{2+}-sensitized Pr in BaY_2F_8, " *IEEE J. of Quantum Electron.*, vol. 24 (6), pp. 1118-1123, 1988.

46. H. H. Zenzie, and Y. Isyanova, "High-energy, high-efficiency harmonic generation from a $Cr:LiSrAlF_6$ laser system, " *Optics Letters*, Vol. 20 (2), pp. 169-171, 1995.

47 M. Stalder, B. H. T. Chai, and M. Bass, *Appl. Phys. Lett.* 58, 216 (1991).

48. T. Shimada, J. W. Early, C. S. Lester, and N. J. Cockroft, "Repetitively pulsed Cr:LiSAF laser for lidar applications, " in *Advanced Solid State Lasers*, Vol. 20 of OSA Proceedings Series (OSA, Washington. D. C., 1994), pp.188-191.

49. V. Yanovski, B. H. T. Chai, Y.-F. Chen, and M. C. Richardson, "High energy 1-in aperture Cr:LiSAF laser", OSA'92 *Annual Meeting of the Optical Society of America*. Albuquerque, NM, Sept. 20-25, 1992.

50 D.V. Keller, B.I. Devis, *IEEE J. Quantum Electron.*, vol. QE-2, pp. 178, 1966.

51. C.H. Thomas, E.V. Price, *IEEE J. Quantum Electron.*, vol. QE-2, pp. 617, 1966.

52. R.V. Lovberg, E.R. Wooding, M.L. Yeoman, *IEEE J. Quantum Electron.*, vol. QE-11, pp. 17, 1975.

53. T. H. Jeys, "Suppression of laser spiking by intracavity second harmonic generation," *Aplied Optics*, Vol. 30, No.9, pp.1011-1013, 1991.

Reproduced with permission of the copyright owner. Further reproduction prohibited without permission.

54. V.G. Dmitriev, G.G. Gurzadyan, D.N. Nikogosian, "Handbook of Nonlinear Optical Crystals," *Springer-Verlag*, Third Revized Edition, 1999.

55. S. C. Buchter, H. P. Jenssen, A. Cassanho, P. Nicholson, "All solid state red, green,and blue Pr:YLF laser," OSA TOPS Vol.19 *Advanced Solid State Lasers*, 1998 OSA, pp. 34-35.

56. R. G. Smith, "Theory of intracavity optical second-harmonic generation, " *IEEE J. of Quantum Electronics*, vol. 6, , pp. 215-223, 1970.

57. J.E. Geusic, H.J. Levinstein, S. Singh, R.G. Smith, L.G. Van Uitert, "Continuous 0.532 μm solid-state source using $Ba_2NaNb_5O_{15}$, " *Appl. Phys. Lett.*, vol. 12 (9), pp. 306-308, 1968.

58. T. Baer, "Large amplitude fluctuations due to longitudinal mode coupling in diode-pumped intracavity-doubled Nd:YAG lasers," *J. Opt. Soc. Am.* B vol. 3, pp. 1175-1180, 1986.

59. W.T. Silfvast, "Laser Fundamentals, " Cambridge University Press, 1996, pp. 341.

60. R. Herloski, et. al., "Gaussian beam ray-equivalent modeling and optical design," *Appl. Opt.*, vol. 22 (8), pp. 1168-1174, 1983.

61. K.A. Menard, "Gussian Resonator Formalism using the y-ybar-method," M.S. thesis, CREOL /UCF 1995.

62. R. Allen, L. Esterowitz, M. Kruer, and F. Bartoli, "Stimulated emission at 0.64 μm in trivalent Pr doped $LiYF_4$," in Abs. 13th Rare Earth Res. Conf., Oglebay Park, Oct. 16-19, 1977, p. 27.

63 L. Esterowitz, F.J. Bartoli, R.E. Allen, D.E. Wortman, C.A. Morrison, and R.P.

Reproduced with permission of the copyright owner. Further reproduction prohibited without permission.

Leavitt, "Energy levels and line intensities of Pr^{3+} in $LiYF_4$," Phys. Rev. B, vol. 19, pp. 6442-6455, 1979.

Reproduced with permission of the copyright owner. Further reproduction prohibited without permission.